University of Padova

Department of Electrical Engineering

A Modern Analysis Approach of Induction Motor for Variable Speed Applications

Supervisor: prof. Nicola Bianchi

PhD student: Luigi Alberti

31 Gennaio 2009

to Ester

Acknowledgment

I wish to express my gratitude to my supervisor Prof. Nicola Bianchi for his valuable comments and guidance throughout the work as well as for giving me the opportunity to participate in several other interesting projects. I also thank Prof. Silverio Bolognani for his suggestions and encouragement.

I wish to thank all my friends at *Electric Drives Laboratory*, including Italian and foreign students. Their presence was a positive contribution to the scientific, technical and social environment of the laboratory.

For the practical works I am obliged to the technicians of the Electrical Engineering Department, they help me in setting the prototypes and during measurement.

I am also grateful to Mr. Leone Donazzan *EME spa* for the measurements data provided. A special thank is for Peter Baldassari for the language proof of this Thesis.

Finally, I wish to thank Serena and Ester for sharing with me this period so enriching for me.

Padova, January 2009 Luigi Alberti

This Thesis is written in LaTeXusing Kile. Pictures are drawn with Gnuplot
An electronic version is available at:
http://paduaresearch.cab.unipd.it

Contents

Sommario

L'analisi della macchina asincrona é oggetto di studio di molti autori da più di cento anni. I diversi approcci presenti in letteratura includono sia modelli analitici che modelli basati sul metodo degli elementi finiti. Sono diverse le motivazioni per cui é importante eseguire un calcolo preciso delle prestazioni della macchina. Negli ultimi anni, ad esempio, le normative internazionali indirizzano sempre più le case costruttrici a produrre motori elettrici ad alta efficienza, nell'intento di diminuire il consumo energetico globale. Per migliorare il progetto di un motore aumentandone il rendimento, é necessario un modello accurato della macchina. C'é poi un interesse economico nell'aumentare la densità di potenza di un motore: ciò significa infatti ridurre le dimensioni di un motore per una prefissata potenza o, similmente, aumentare le prestazioni della macchina a parità di dimensioni.

In alcune particolari applicazioni poi, non è sufficiente un progetto "standard" del motore. É necessario infatti un modello più accurato, che consideri anche la dinamica termica della macchina. É questo il caso di macchine elettriche che operano in condizioni particolari, ad esempio in ambienti ad alta temperatura, alta pressione, ecc.

Oltre a ciò, nei processi di produzione industriale, si deve anche considerare il tempo necessario per effettuare il progetto della macchina. Infatti, un modello "idealmente esatto" la cui soluzione richiede tempi eccessivamente lunghi, non é di particolare interesse pratico, specialmente nel caso in cui il progetto si compia mediante più iterazioni e parametrizzazioni. Se per esempio si usano simulazioni agli elementi finiti tridimensionali, il tempo di simulazione cresce molto velocemente e nonostante i prestanti processori disponibili al giorno d'oggi, si possono avere tempi di simulazione molto lunghi. Se poi la simulazione agli elementi finiti della macchina elettrica é usata in un modello di sistema più complesso, é chiaro come il tempo di simulazione totale possa raggiungere una durata non compatibile con i ritmi di sviluppo industriale.

Da tutto ciò nasce l'esigenza di impiegare modelli accurati e veloci per il calcolo delle prestazioni della macchina. Il modello deve essere infatti sufficientemente rapido per poter essere utilizzato nelle attività di progetto e analisi giornaliere, tipiche di un'azienda. Esso deve garantire inoltre una adeguata accuratezza delle prestazioni calcolate. [1]

La costruzione di modelli secondo questi criteri, é stata al centro della pro-

[1] L'accuratezza del modello può essere affinata con il suo utilizzo tarandolo sulla base di misure sperimentali.

duzione scientifica internazionale degli ultimi anni. In letteratura si possono trovare infatti molte pubblicazioni riguardanti questo tema. Inoltre, anche i software commerciali per l'analisi ed il progetto di macchine elettriche implementano sempre più strategie di questo tipo, proprio per rispondere alle esigenze delle case costruttrici che li utilizzano.

In questo lavoro, si presenta un contributo all'analisi della macchina asincrona ad induzione. L'approccio scelto consiste nell'elaborare modelli della macchina asincrona combinando tecniche analitiche e agli elementi finiti e facendo sinergia della loro unione. In tal modo, la velocità dei modelli analitici e l'accuratezza degli elementi finiti si completano a vicenda permettendo di ottenere un calcolo rapido delle prestazioni, con una buona precisione.

Di seguito di presenta sinteticamente il contenuto di questa tesi capitolo per capitolo.

Contenuti

Questo lavoro é suddiviso in sei capitoli. Il primo capitolo introduce una procedura agli elementi finiti per calcolare un circuito equivalente "normalizzato" della macchina asincrona. Il circuito equivalente ottenuto é normalizzato nel senso che esso può essere usato per ogni motore costruito con il lamierino simulato. Le simulazioni agli elementi finiti sono eseguite una sola volta e successivamente i parametri del circuito equivalente sono riadattati solo analiticamente. In questo modo il tempo di calcolo risulta sensibilmente ridotto.

Il Capitolo 2 presenta alcuni esempi applicativi del modello descritto nel primo capitolo. Sono state considerate due diverse serie di motori: la prima su lamierino standard, la seconda per argano.

Nel Capitolo 3 si é considerato il progetto di motori per applicazioni non standard. In particolare é proposta un'analisi combinata termica–magnetica del motore asincrono con l'obiettivo di ottenere una stima precisa e rapida delle sue prestazioni. Il circuito equivalente del motore é accoppiato con una rete termica a parametri concentrati per il calcolo della sovra temperatura in ogni punto della macchina. Poiché sia il circuito equivalete che la rete termica sono modelli analitici, bastano pochi secondi per eseguire l'analisi. Allo stesso tempo, le simulazioni agli elementi finiti danno un preciso calcolo dei parametri usati nei modelli analitici, garantendo una buona accuratezza nella stima delle prestazioni del motore.

Il Capitolo 4 introduce una procedura di analisi agli elementi finiti per motori a velocità variabile. Una novità della procedura esposta riguarda l'uso esclusivo di simulazioni magnetostatiche per l'analisi del motore sia per il funzionamento a vuoto che per il funzionamento a carico. Entrambe le correnti di statore e rotore sono imposte come sorgenti del campo magnetico; in tal modo, la simulazione della macchina ad induzione è del tutto assimilabile alla simulazione della macchina sincrona, ed il tempo di calcolo risulta notevolmente ridotto.

Tale procedura può essere usata per ottenere un circuito equivalente del motore, oppure come un *solver* per il calcolo della traiettoria "maximum torque per Ampere" e della caratteristica coppia velocità dell'azionamento.

Nel Capitolo 5, la procedura esposta nel capitolo precedente é usata per l'analisi di un motore asincrono per lavatrice. Diversi punti di lavoro sono considerati, sia a bassa che ad alta frequenza. Le prestazioni ricavate sono confrontate con i risultati ottenuti mediante la procedura descritta nel primo capitolo e con le misure effettuate su di un prototipo.

Nel Capitolo 6, é presentato lo studio di fattibilità di un motore asincrono *doubly fed* ad avvolgimento concentrato frazionario per applicazioni *direct–drive*. Nel capitolo si mostra che per questa tipologia di macchine una specifica scelta del numero di cave di statore e rotore minimizza l'interazione fra armoniche di forza magnetomotrice statoriche e rotoriche, limitando le perdite e le oscillazioni di coppia.

Introduction

ANALYSIS of the induction machine (IM) has been conducted around the world, by many different authors, for more than one hundred years. Throughout the years various approaches from analytical models to the newer finite element computations have been extensively presented in the literature. There are various reasons for a precise computation of the machine performance. In recent years international standards have dictated that industries produce more efficient electrical machines. The goal is to reduce the global energy consumption and this improvement is achievable only with ever increasing machine model accuracy. There is also an economic interest to increasing the power density of a machine: this means to reduce the machine dimensions for a given power, and to increase the performance of a machine of given size.

In particular applications, standard design methods are not suitable and a more accurate model is necessary. Typically today's best methods include the thermal as well as the electromagnetic analysis of the machine. This is certainly the case for machines operating in severe external conditions, such as high temperature, frequent overloads, corrosive or polluted atmosphere, and so on.

Besides these considerations, competition in the global marketplace has shortened the time fame in which new designs must be completed. In today's environment a very precise analysis which requires a long time (even days or weeks) is no longer acceptable, especially in an iterative design process with some parametrization. If the finite element simulation of the machine is linked to a more complicated model of the system (including for instance control algorithms, mechanical and thermal transients, etc.), the computational time becomes not compatible with the development process of the industries.

These facts then give rise to the necessity for the existence of a rapid and accurate model for machine performance prediction. The model must be rapid enough for daily use in office calculation but yet has to exhibit good accuracy. This trend is evident in recent international publications. Further evidence is provided by the fact that commercial software for electrical machines analysis and simulations is following such an approach.

In this Thesis, a contribution to the analysis of induction machine is presented. The approach is to elaborate and detail models which combine analytical and finite element methods in novel and ingenious ways. Therefore, the speed of the analytical approach is refined with the accuracy of the finite element method and the synergy between the two methods is maximized.

Outline

This work is divided into six Chapters. The first Chapter introduces a finite element procedure to compute a normalized equivalent circuit of the induction machine. The equivalent circuit is normalized, in the sense that it can be used for any induction machines composed by the simulated lamination geometry and winding distribution. The finite element simulations are carried out only once and subsequently the equivalent circuit parameters are adjusted analytically therefore the computational time is very short.

Chapter 2 presents some application examples of the model described in Chapter 1. At first, a series of induction motors for standard applications are considered. Then, an induction machine for an elevator system is considered.

In Chapter 3 the design of electrical machines for extreme operating conditions is considered. This Chapter proposes a coupled thermal–magnetic analysis of an induction machine with the primary goal of achieving a rapid and accurate prediction of its performance. The equivalent circuit of the machine is coupled with a lumped parameter thermal network to predict the temperature in each part of the IM. Since both the equivalent circuit and thermal network solutions are analytic, the analysis converges very rapidly. At the same time, the finite element analysis yields a precise estimation of the IM parameters used in the analytical models.

Chapter 4 deals with an analysis procedure of a field oriented controlled induction motor by means of finite element simulations. A novelty of the proposed procedure is that only magnetostatic field solutions are used for both no–load and under load analysis. Both the stator and rotor currents are imposed as field source. In this way, the IM simulation is similar to that of a synchronous machine, and the computational time again is very low.

This strategy can be used to achieve an equivalent circuit of the IM or as a solver for the computation of the maximum torque per Ampere trajectory and the torque versus speed characteristic of the drive.

In Chapter 5, the analysis procedure presented in Chapter 4 is adopted for the computation of an IM for a washing machine application. Various operating conditions, at low and high frequency, are considered. The computation is compared with results obtained from the analysis described in Chapter 1 and from measurements.

Chapter 6 investigates the possibility of designing a fractional–slot doubly fed IM for a direct–drive application. This Chapter shows that proper choice of the number of stator and rotor slots minimizes the interaction between stator and rotor MMF harmonics, thereby limiting losses and minimizing torque ripple. The design strategy of the doubly fed induction machine is explained and the results are discussed, highlighting the advantages and drawbacks of each proposed solution.

Original contribution

The material presented in this work represents an evolution of the classical analysis of ac induction motors, however without an exclusive use of the finite ele-

ment method. While such a method is a powerful analysis technique, the classical analytical approaches of simplified models, equivalent circuits, etc. can not be abandoned. Since *in medio stat virtus*, the basic principles of electrical machine theory are strictly bound to the powerful modern numerical approaches. The truth being that neither approach dominants over the other and indeed they can work in conjunction to produce an accurate, speedy analysis environment.

As a consequence, although the author has been deeply influenced by the writing of Alger, Liwschitz–Garik, Veinott, Williamson and many others, various new materials presented in this work can be considered as an original contribution to the analysis. Among the others, I'd like to remember:

1. *A normalized equivalent circuit for achieving the IM performance.*
   FE analysis is carried out only once and then the model is rearranged analytically for any motors formed by the simulated lamination geometry. This is described in Chapter 1 and 2 and also in publications [1–3];

2. *Computation of the thermal network parameters with FE method.*
   The FE analysis is adopted to compute proper thermal parameters of the machine. These parameters are used in a thermal network combined with the electro–magnetic model of the motor. Then, the machine performance is computed solving jointly together the two analytical model. This is described in Chapter 3, and in publications [4, 5];

3. *Simulation of IM for variable speed drive*
   An analysis strategy is proposed for the analysis of IM adopting the rotor flux reference frame. Therefore the currents in the simulation are adjusted so as to orient the rotor flux along the d–axis. Only magnetostatic field solutions are used for both no–load and under load analysis. In this way, the IM simulation is similar to that of a synchronous machine and the computational time results reduced taking into account saturation in each operating point of the machine. See Chapter 4 and 5. This is connected with publications [6, 7];

4. *An investigation of feasibility of a direct drive fractional slot IM.*
   Chapter 6 the possibility to adopt a fractional–slot doubly fed IM in a direct–drive application is investigated. An index I_{shi} is introduced to quantify the interaction of the MMF harmonics with respect to the main harmonic. This is connected with publication [8].

Chapter 1

Rapid IM Performance Computation Combining Analytical And Finite Element Analysis

Abstract– A rapid and accurate analysis of the induction motor is the basis of any design process. This Chapter deals with an analysis procedure of the induction motor combining a set of finite element simulations with an analytical model. The finite element simulations are used to achieve the non linear parameters of the equivalent circuit. The choice of specific quantities during the FE simulations releases the results from the actual motor length and number of conductors. In this way, the obtained results are normalized, in the sense that they can be adopted for any IM formed by the same lamination geometry and by the same winding distribution. Both three–phase and single–phase machines are considered.

1.1 Introduction

THE analysis of the induction motor (IM) is presented in literature extensively, including analytical models [9–11] and finite element (FE) computations [12, 13]. The first approach is appreciated for its speed, in spite of the inevitable approximations. The second approach is favorable for its accuracy: finite elements consider properly the iron saturation at various magnetizing currents and the current density distribution within the rotor slot at different rotor frequency [14]. However, a common requirement to any analysis or design procedure is to reduce the computation time without any loss of accuracy in predicting the IM performance.

This Chapter presents an analysis procedure that combines a set of FE simulations with an analytical model of the motor. The main aim is to achieve a prediction of the IM performance that is rapid and accurate at the same time. In other words, the IM model has to be accurate enough to allow good prediction of the motor performance, and the computation time (mainly due to the FE simulations) has to be as short as possible.

Only a few FE simulations are carried out so as to achieve the more significative motor parameters. The flux lines are mainly two–dimensional lines, so that a two–dimensional analysis is generally satisfactory, with a substantial reduction of the computational time [15]. Then, a three–dimensional correction is needed, to include such effects as end–winding and ring resistances and inductances, skewing and so on. Finally, once the motor parameters are derived, the analytical model is adopted for all subsequent computations.

This approach overcomes the limits of the completely analytical or completely numerical procedures. In addition, the FE simulations required in the proposed procedure can be carried out using any commercial or free software. Even if further advantages could be achieved by means of a fine–fitting IM analysis procedure [16] (among them: a minimum domain required in FE simulations, a shorter computation time, or a complete consideration of the rotor current harmonics), the proposed procedure allows for an easy implementation.

Another novelty of the analysis proposed in this Chapter is the choice of the main quantities, which are closely bound to the lamination geometry. Therefore the IM features result to be independent of the actual power rating and voltage. The obtained results can be adopted for any size of the IM formed by the same lamination geometry and winding distribution.

There are two main reasons that inspire this approach. At first, there is an increasing request by industry for rapid prediction of the IM capability, comparing rapidly various configurations with reasonable accuracy. Secondly, in a practical IM design, commercial laminations are adopted: the geometry of the lamination is fixed, while the design variables remain the motor stack length L_{stk} and the number of turn per phase N_t.

The proposed procedure can be applied to different IM types. At first the analysis of the three–phase IM is introduced, and then the single–phase IM is considered. In the latter case, some expedients are adopted for a more precise prediction of the motor parameters. These will be accurately described here.

For both configurations, the experimental measurements on some IM prototypes confirm the accuracy of the prediction achieved by means of the proposed analysis. For the sake of completeness, the limits and the possible improvement to the proposed procedure are also underlined where necessary. Finally, the effect of temperature on the parameter computation is investigated.

1.2 Choice of the analysis quantities

The main quantities of the analysis are chosen accurately, so as to bind the IM features to the lamination geometry rather than the actual motor power rating and voltage. Therefore, actual quantities such as number of turns, current, and voltage are not considered, while other more general quantities are taken into account. They are:

- the current density within the whole slot (peak value), given by

$$\hat{J}_{slot} = \sqrt{2} k_{fill} J_c \tag{1.1}$$

  where k_{fill} is the fill factor and J_c is the rms current density in the conductor,
- the flux linkage of each phase, referred to one conductor per slot ($n_{cs} = 1$) and to a unity stack length ($L_{stk} = 1m$),
- other integral quantities, such as magnetic energy, power losses, and so forth are referred to a unity stack length.

In this way, the obtained results are normalized, in the sense that they can be adopted for any IM formed by the same lamination geometry and by the same winding distribution.

1.2.1 Description of the winding distribution

The winding distribution is described by the slot matrix [17]. This is a $m \times Q_s$ matrix, where m is the number of phases and Q_s is the number of slots. Each term k_{qj} of the matrix is equal to the per unit filling of the q–th slot by the j–th phase conductors. Then, k_{qj} assumes a value between –1 and +1. In a three–phase motor typical values are:

- $k_{qj} = 0$ if there are no conductors of the j–th phase within the q–th slot;
- $k_{qj} = \pm 1$ if the q–th slot is filled completely by conductors of the j–th phase, and the sign is assigned according to the reference direction;
- $k_{qj} = \pm 0.5$ if only half a q–th slot is filled by conductors of the j–th phase, and the sign is assigned according to the reference direction.

An example is reported in Fig. 1.1, referring to a three–phase two–pole single–layer winding with two slots per pole and per phase.

1.3 Combined FE–analytical procedure

The flow–chart of the proposed IM analysis is sketched in Fig. 1.2. The steps of the analysis are the following:

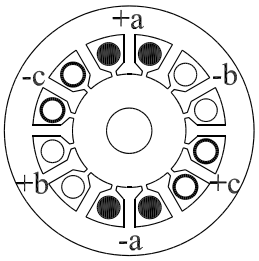

Figure 1.1: Example of a three–phase 12–slot two–pole single–layer winding. The slot matrix results in

	slot number											
phase	1	2	3	4	5	6	7	8	9	10	11	12
a	0	0	1	1	0	0	0	0	-1	-1	0	0
b	-1	-1	0	0	0	0	1	1	0	0	0	0
c	0	0	0	0	-1	-1	0	0	0	0	1	1

1. The no–load performance of the IM is analyzed by using FE simulations that allow an accurate prediction of the iron saturation phenomenon. Assuming a rotor slip equal to zero so that the rotor frequency is zero (the motor is analyzed in the rotor reference frame), magnetostatic simulations are carried out.
   The aim of the no–load test is to investigate the saturation of the iron lamination and to compute the corresponding parameters of the equivalent circuit. Since the flux lines in an IM are mainly within the laminations, a two–dimensional analysis is generally satisfactory to determine the saturation effects.
   The magnetizing characteristic is an intrinsic characteristic of the lamination and the winding distribution and it is applied to any motor adopting the same lamination and winding distribution [1].
2. From the no–load simulations, the maximum flux density in the stator teeth B_t and in the stator back iron B_{bi} are computed and the iron losses derived.
3. Then FE analysis is carried out at locked rotor, to account accurately for the rotor current distribution. The rotor parameters are computed from the rotor Joule losses P_{jr} and the magnetic energy W_m [17]. The simulations are carried out at various frequencies so as to determine their dependency on the frequency.
4. Since the previous analysis is two–dimensional, three–dimensional parameters are computed analytically and are added to the equivalent circuit (see Fig. 1.3) [14]. They are (i) the stator resistance r_s, (ii) the stator coil end winding leakage inductance $l_{\sigma ew}$, (iii) the rotor cage ring resistance r_{ring} and (iv) the rotor cage ring leakage inductance $l_{\sigma ring}$. Effects of skewed

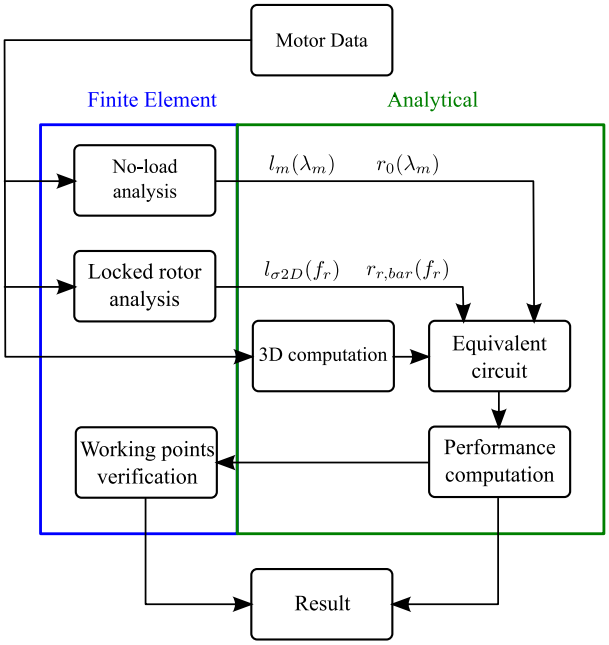

Figure 1.2: Scheme of the combined FEM–analytical procedure

rotor bars are also introduced in the circuit as an additional leakage inductance.

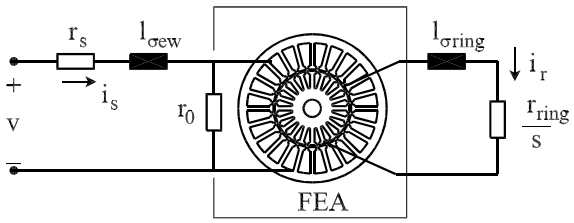

Figure 1.3: Schematic model of the three–phase induction motor.

5. When all parameters of the equivalent circuit are derived, the motor performance can be predicted.
6. A further check of the operating points is carried out using a direct FE analysis, where the sources are derived from the analytical model. For a given rotor speed, the stator current is computed from the equivalent circuit and it is imposed into the FE simulation so as to compute the rotor

current and torque. These quantities can be compared with those derived from the equivalent circuit of the motor.

Each of these steps is described in detail in the following sections.

1.3.1 No–load analysis

The aim of the no–load analysis is to investigate the saturation of the iron lamination and to compute the corresponding parameters that will be used in the equivalent circuit.

The motor is analyzed in the rotor reference frame. Assuming a rotor slip equal to zero, the frequency also equals zero. Thus FE magnetostatic simulations are carried out, where the field source is the slot current density $\hat{J}_{slot}$.

The maximum flux density in the teeth B_t and in the back iron B_{bi} are derived from the FE field solutions. Fig. 1.4 shows the paths in the stator teeth (curve

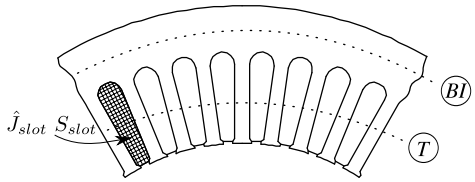

Figure 1.4: Paths for flux density computation

T) and in the back iron (curve **BI**), along which the maximum flux density is calculated. It is reasonable to assume that the flux density varies sinusoidally in time in each part of the stator [12]. Then, the stator iron losses are estimated from B_t and B_{bi} according to the iron loss characteristics, published by the manufacturer and normally specified in terms of Watt per unit weight. These losses are synthesized by means of the resistance r_0 [18], assuming that the dependence of the flux density on the main flux linkage, computed at no–load, remains the same during operation under load.

In recent years, other authors have proposed improved models for the computation of iron losses [19,20]. A more precise analysis, for example based on several FEA simulations or a time stepping analysis, is not reported here. In any event it is quite simple to include, in the proposed strategy, a more precise iron losses parameter on the basis of available data (for example starting from a previous time stepping analysis or measurements).

Some considerations can be drawn concerning the two paths of Fig. 1.4. In the search of the flux density B_t, the path is chosen in the middle of the teeth, and the result does not change if the path is moved up or down. There are two reasons for this. First, there is a minimum influence of the slot leakage flux with respect to the magnetizing flux, since the maximum of the air gap flux density occurs where the stator currents are lower, that is, the slot leakage flux is lower. Second, the highest leakage flux comes from the tooth shoe, and its variation along the tooth height is slight.

The path to determine the flux density B_{bi} is chosen at 2/5 of the back iron height towards its inner diameter. The variation of flux density in the back iron is described in [21,22]. It is shown that the variation of the flux density can be up to 30% of the average value referring to a constant permeability (linear iron). The average value of B_t^2 is found to be close to 2/5 of the back iron height. When the iron saturation is taken into account, the variation decreases to 5%. Therefore, the choice of a path at 2/5 of the back iron height yields a satisfactory approximation.

The normalized magnetizing flux linkage $\hat{\lambda}_m$ is computed varying $\hat{J}_{slot}$. The resulting curve $\hat{\lambda}_m - \hat{J}_{slot}$ is an intrinsic characteristic of the lamination and the winding distribution. This curve can be applied to all motors using the same lamination and winding distribution, without the need for simulating each motor separately. This is useful when a series of IMs is being investigated. The no–load characteristic of any actual motor can be achieved by rearranging the normalized flux–linkage and slot current density according to the actual stack length and number of conductors per slot.

1.3.2 Locked rotor analysis

In the locked rotor analysis, linear iron is assumed for the lamination, so that the superposition of the effects can be applied. This is suitable for the estimation of the rotor parameters that are assumed to be independent of the magnetizing flux.

To achieve reasonable results, when rotor slots are closed with a narrow bridge, such a bridge is considered completely saturated [23–26]. Thus, it is substituted by an equivalent air bridge. It has been experimented that this approximation does not yield any appreciable discrepancy in the rotor parameter prediction.

Once again the analysis is carried out in the rotor reference frame, so that the frequency of the simulation corresponds to the rotor frequency f_r. A magnetodynamic analysis is carried out in order to consider the various non–uniform distributions of the current density within the rotor bars.

The same analysis is repeated at various frequencies, so as to get the dependence of the rotor parameters on the operating frequency.

1.4 Analysis of the three–phase IM

First, let us refer to a three–phase motor. The equivalent circuit is shown in Fig. 1.5. All the elements in the circuit refer to a motor with one conductor per slot $n_{cs} = 1$ and $L_{stk} = 1$ m. Small letters are used for these normalized parameters. Actual values of resistance and inductance are achieved by multiplying the normalized values by $n_{cs}^2 L_{stk}$.

Fig. 1.5 refers to the fundamental MMF harmonic [27]. MMF harmonics can be considered rearranging the equivalent circuit as indicated in [28] additional parameters are added in series to the fundamental parameters. These additional parameters can be derived from the fundamental ones as indicated in [11,29].

In the following, only the fundamental MMF component is considered. However, when a motor is characterized by high MMF harmonic contents, taking into

account the MMF harmonics is necessary. This is the case of an IM with fractional–slot windings and Dahlander windings, in the configuration with lower number of poles.

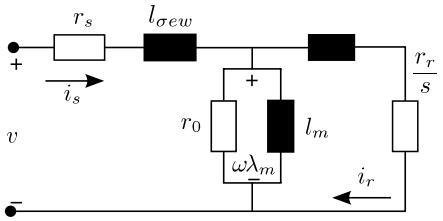

Figure 1.5: Equivalent circuit of the three–phase induction motor. Lower case is used for normalized parameters ($n_{cs} = 1$, $L_{stk} = 1$ m).

1.4.1 No–load parameters

From the no–load FE analysis, the normalized magnetizing inductance is computed as:

$$l_m = \frac{\hat{\lambda}_m}{\hat{J}_{slot} S_{slot}} \tag{1.2}$$

The no–load analysis is carried out imposing the current density $\hat{J}_{slot,a} = \hat{J}_{slot}$ and $\hat{J}_{slot,b} = \hat{J}_{slot,c} = -\hat{J}_{slot,a}/2$. Only in case of linearity of the iron path, the flux linkages results in $\lambda_b = \lambda_c = -\lambda_a/2$. In other words, it is $\lambda_a/\hat{J}_{slot,a} \neq \lambda_b/\hat{J}_{slot,b}$. Then, when iron saturation is considered, the magnetizing flux linkage is averaged out as

$$\hat{\lambda}_m = \frac{2}{3}\left(\lambda_a - \frac{\lambda_b}{2} - \frac{\lambda_c}{2}\right) \tag{1.3}$$

Fig. 1.6 shows the normalized flux linkage and the magnetizing inductance vs. the slot current density.

The second parameter that is computed from the no–load simulation is the iron loss resistance r_0. The flux density in the stator teeth B_t and in the stator back iron B_{bi} are extracted from the field solution (see Fig. 1.4) and expressed as a function of the slot current density. Thanks to the link between flux linkage and current density described above, the flux densities B_t and B_{bi} can be expressed as a function of the flux linkage $\hat{\lambda}_m$ itself. Hence, the iron losses and the resistance r_0 used in the equivalent circuit of Fig. 1.5 are functions of $\hat{\lambda}_m$.

The adopted equivalent circuit considers all the two–dimensional leakage inductances on the right–hand side of the magnetizing inductance l_m. In other words, the Γ–type equivalent circuit is adopted [30]. A simple transformation exists to derive the Γ–type from the more used T–equivalent circuit [17]. Thus, it is not necessary to separate the leakage inductances from the magnetizing inductance.

However, it could be interesting to estimate the weight of the leakage inductances with respect to the magnetizing inductance [31]. Among the others, the

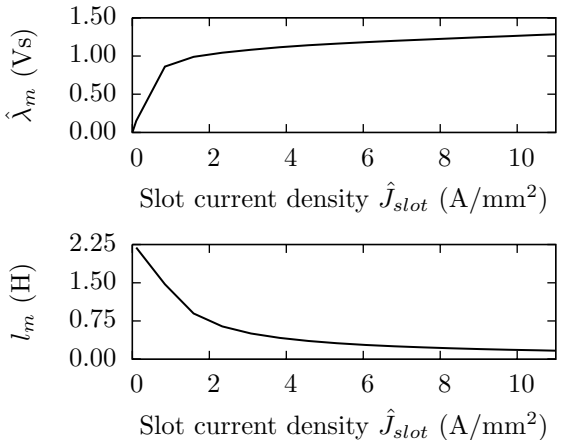

Figure 1.6: Normalized flux linkage and magnetizing inductance vs. slot current density (n_{cs}=1 L_{stk}=1 m).

stator slot leakage inductance can be easily derived from the magnetic energy in the stator slots [25], which is

$$W_{slot} = \int_{slot} \frac{1}{2} BH dvol \tag{1.4}$$

This is not possible for the other leakage inductances, such as the zig–zag and the belt inductances.

1.4.2 Locked rotor parameters

From the rotor Joule losses P_{jr} and the total magnetic energy W_m the equivalent series parameters are computed as:

$$r_{eq} = \frac{2P_{jr}}{3\left(\hat{J}_{slot} S_{slot}\right)^2} \tag{1.5}$$

$$l_{eq} = \frac{4W_m}{3\left(\hat{J}_{slot} S_{slot}\right)^2} \tag{1.6}$$

Then, imposing the equivalence between the two circuits of Fig. 1.7 (this FE analysis is carried out using a constant iron permeability), the rotor parameters result in

$$r_{r,bar}(f_r) = \frac{l_m^2 r_{eq}}{(r_{eq}/\omega)^2 + (l_m - l_{eq})^2} \tag{1.7}$$

$$l_{\sigma 2D}(f_r) = l_m \frac{l_{eq}(l_m - l_{eq}) - (r_{eq}/\omega)^2}{(r_{eq}/\omega)^2 + (l_m - l_{eq})^2} \tag{1.8}$$

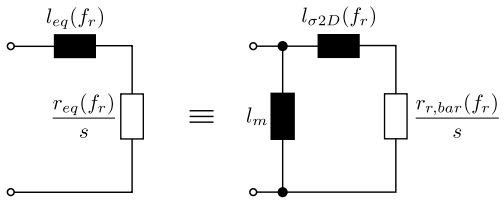

Figure 1.7: Equivalent circuits under locked rotor operations.

Repeating this calculation for various frequencies, the motor parameters are computed at various rotor frequencies f_r. An example of the behavior of $r_{r,bar}$ and $l_{\sigma 2D}$ versus rotor frequency is shown in Fig. 1.8.

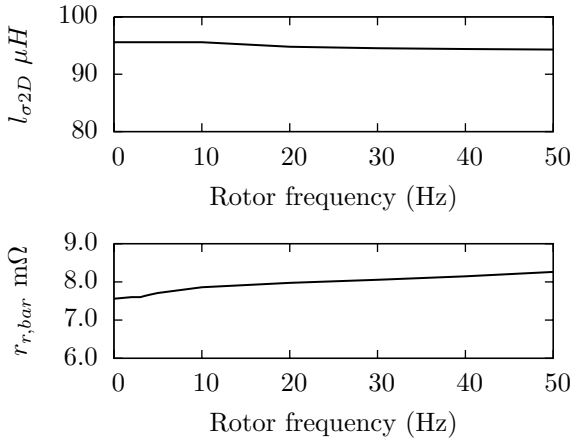

Figure 1.8: Normalized two dimensional parameters vs. rotor frequency (n_{cs} =1, $L_{stk} = 1$ m).

1.4.3 Three–dimensional computation

This subsection summarizes the three–dimensional parameter corrections (3D computation of Fig. 1.2). In the following, simple and practical expressions are reported for any parameters. In addition, for the same computations, further references are cited where alternative or particular computations are reported.

Stator resistance

The stator normalized resistance is calculated as

$$r_s = \rho_{Cu} \frac{1}{k_{fill} S_{slot}} \frac{Q_s}{3} \frac{L_{tot}}{L_{stk}} \tag{1.9}$$

where Q_s is the number of stator slots, and L_{tot} is the total length of one conductor (half a turn), given by $L_{tot} = (L_{stk} + L_{ew})$. The end–winding length L_{ew} can be approximated as $L_{ew} = y_q \pi D_e / Q_s$, where y_q is the coil throw (in number of slots). Then it is

$$\frac{L_{tot}}{L_{stk}} = \left(1 + \frac{y_q}{Q_s} \frac{\pi D_e}{L_{stk}}\right) \tag{1.10}$$

A different approximation of L_{ew} is suggested in [9] according to concentric coil windings.

For large or high–speed machines, the stator resistance has to be increased, considering the skin and proximity effect in the stator conductors [10, 32, 33].

Stator coil end–winding leakage inductance

A semi–empiric relationship is used to predict this leakage inductance:

$$l_{\sigma ew} = \mu_0 q^2 \frac{\pi D}{L_{stk}} \lambda'_{ew} \tag{1.11}$$

where $q = Q_s/(2pm)$ is the number of stator slots per pole per phase, and λ'_{ew} is the specific permeance that can be approximated as λ'_{ew}=0.5 [21]. Alternative relationships can be found in [10, 34–36].

Rotor cage skewing

Rotor skewing is taken into account by including a skew leakage inductance to the stator leakage inductance and reducing the magnetizing inductance. Thus, l_m is reduced to $l_m(1 - k^2_{skew})$ and $l_{\sigma 3Ds} = l_{\sigma ew} + l_m k^2_{skew}$, where k_{skew} is the rotor skewing factor [16, 30].

Rotor cage ring resistance

The ring resistance is considered as an increment to the resistance of the rotor bar. This is accomplished by introducing the corrective factor k_{ring}, as:

$$r_r = r_{r,bar}(1 + k_{ring}) \tag{1.12}$$

where a simple expression for k_{ring} is:

$$k_{ring} = \frac{2}{\pi} \frac{Q_r}{(2p)^2} \frac{D_r}{L_{stk}} \frac{S_{bar}}{S_{ring}} \tag{1.13}$$

where Q_r is the number of rotor slots, D_r is the average diameter of the ring, and S_{ring} is the ring cross area. An alternative expression can be derived from [18].

Sometimes, the resistance of the ring can be considered as an additional resistance of the slot. In the FE simulation the conductor resistivity could be increased by the factor $(1 + k_{ring})$. However, as shown in (1.13), this correction depends on the actual length of the motor. Therefore, it is preferable to add the ring resistance to the rotor bar resistance in the equivalent circuit of the motor.

Table 1.1: Dependence of parameters

R	$\propto$	$n_{cs}^2 L_{stk}$	Resistance
L	$\propto$	$n_{cs}^2 L_{stk}$	Inductance
V	$\propto$	$n_{cs} L_{stk}$	Voltage
Λ	$\propto$	$n_{cs} L_{stk}$	Flux linkage
I	$\propto$	$1/n_{cs}$	Current
T	$\propto$	L_{stk}	Torque
W_m	$\propto$	L_{stk}	Magnetic energy
P	$\propto$	L_{stk}	Power, Losses

Rotor cage ring leakage inductance

The leakage inductance due to the end ring could be estimated as

$$l_{\sigma,ring} = \mu_0 k_r \left(\frac{k_{ws}}{k_{skew}} \right)^2 q^2 \frac{\pi D_r}{L_{stk}} \tag{1.14}$$

where $k_r = 0.36$ if $2p = 2$, while $k_r = 0.18$ if $2p > 2$ [37], and k_{ws} is the stator winding factor. Then, $l_{\sigma,ring}$ is added to the two dimensional leakage inductance computed above, yielding $l_\sigma = l_{\sigma 2D} + l_{\sigma,ring}$. Other authors, e.g. [9,21,38], propose alternative approximations on the basis of their experiences.

1.4.4 Equivalent circuit and computation

Once all parameters of the equivalent circuit of Fig. 1.5 are defined, the IM model is ready for computing the performance of any IM that is formed by the simulated lamination geometry and winding distribution. According to the actual number of series conductors per slot n_{cs} and the given stack length L_{stk}, the IM actual parameters are computed from the normalized parameters. Table 1.1 reports the conversion factors.

1.4.5 Experimental verification

A two–pole 3–kW three–phase motor is considered to verify the proposed procedure. Outer and inner diameters are 135 mm and 70 mm respectively. Stator and rotor slots are 24 and 18 respectively, and the stator slot area is 88 mm^2. A single–layer full-pitch winding is adopted. As far as the quantities linked to the power and voltage of the machine, the stack length is $L_{stk} = 130$ mm, while the number of conductors per slot is $n_{cs} = 33$.

Fig. 1.9 shows the flux plots of a magnetostatic (f_r=0 Hz) and a magnetodynamic simulation at f_r=5 Hz. The motor symmetry allows only half a motor section to be simulated, with a further reduction of the computation time. The normalized flux linkage and magnetizing inductance vs. slot current density are reported in Fig. 1.6, and the normalized rotor parameters vs. frequency are shown in Fig. 1.8.

Fig. 1.10 shows the torque and current behavior versus slip. The rotor temperature is fixed to be 120 Celsius degrees. The starting torque has been measured at reduced voltage. Then the measured value has been reported according to the test voltage and the temperature. Fig. 1.11 shows the power factor prediction versus slip. Fig. 1.12 reports the mechanical power prediction vs. slip. The results predicted by means of the proposed method are compared with the measurements (circle are used in the figures). A good match can be observed.

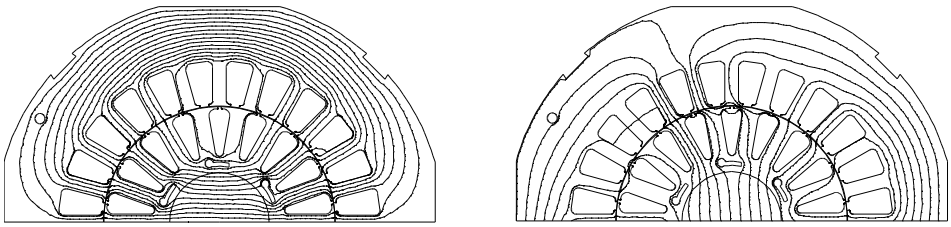

Figure 1.9: Flux plots of a 3 kW three–phase two–pole motor, simulations at f_r=0 Hz and f_r=5 Hz respectively.

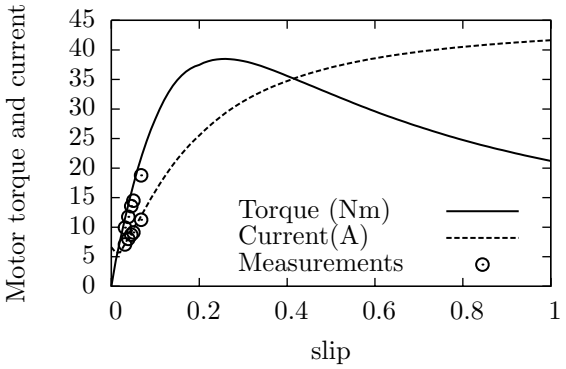

Figure 1.10: Three–kW three–phase IM. Torque and current prediction vs measurements.

1.5 Analysis of the single–phase IM

The same procedure proposed to analyze the three–phase IM can be applied to study the single–phase IM. Among the various models [39–41] the revolving–field theory is applied [9, 42]. The equivalent circuit is shown in Fig. 1.13 where the forward and backward impedances are given in Fig. 1.14. As above, the normalized parameters of the equivalent circuit are achieved by simulating the no–load and the locked–rotor operations of the motor. From such an equivalent circuit the motor performance is computed [43].

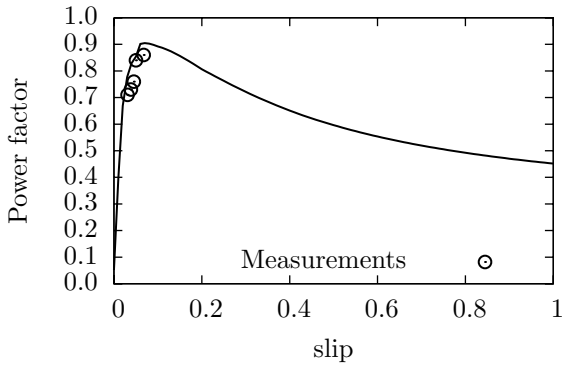

Figure 1.11: Three–kW three–phase IM. Power factor prediction vs measurement.

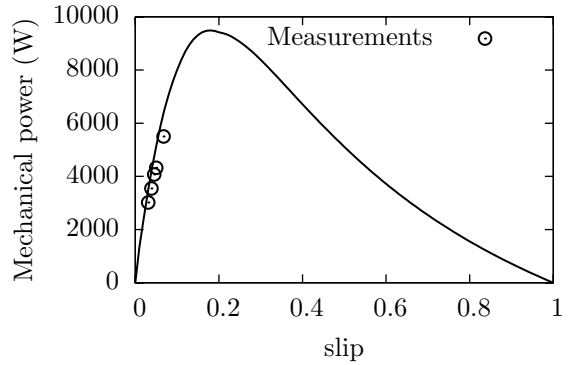

Figure 1.12: Three–kW three–phase IM. Mechanical power prediction vs measurement.

1.5.1 No–load analysis

As before, the simulations of the no–load test of the motor are carried out by feeding the single–phase winding with a given slot current density $\hat{J}_{slot}$ and computing the corresponding flux linkage $\hat{\lambda}_m$ from the field solution.

Fig. 1.15 shows the normalized flux linkage as a function of the slot current density of a single–phase IM. The dashed line refers to the values computed from the FE field solutions. Thus, the curve represents the relationship point by point between the two quantities. Because of the non linearity of the iron B–H curve, the flux linkage is not proportional to the slot current density.

In order to achieve the relationship between the rms values of the two quantities, the following procedure is adopted:

1. From a set of magnetostatic simulations, the $\hat{\lambda}_m - \hat{J}_{slot}$ characteristic is

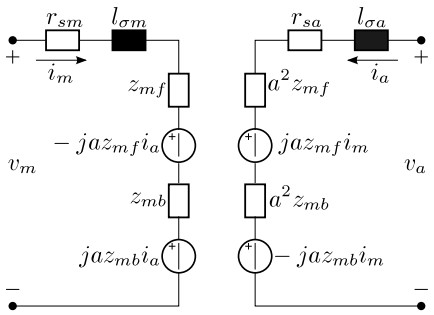

Figure 1.13: Equivalent circuit of the single–phase motor, corresponding to the revolving–field theory.

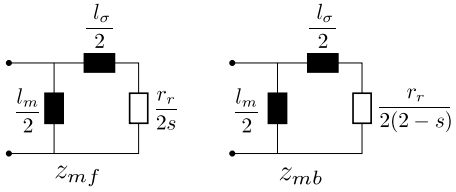

Figure 1.14: Equivalent circuits of the forward and backward impedances.

computed, considering the point by point values (dashed line of Fig. 1.15).

2. Assuming a sinusoidal waveform of the flux linkage, with rms value $\lambda_{rms} = \hat{\lambda}_m/\sqrt{2}$, the corresponding waveform of the slot current density is computed by using the $\hat{\lambda}_m - \hat{J}_{slot}$ characteristic derived in the previous step. An example is reported in Fig. 1.16: the current density waveform is computed from the flux linkage waveform and the correspondence achieved by the $\hat{\lambda}_m - \hat{J}_{slot}$ characteristic of Fig. 1.15 (dashed line).
3. The true rms value $J_{slot,rms}$ is computed from the calculated waveform of the slot current density. It is then associated to the flux linkage λ_{rms}.
4. By repeating the process above for various rms values of the flux linkage, a new characteristic $\lambda_{rms} - J_{slot,rms}$ is reconstructed. This characteristic corresponds to the solid line of Fig. 1.15, where $\hat{\lambda}_m = \sqrt{2}\lambda_{rms}$ and $\sqrt{2}J_{slot,rms}$ are drawn for a better comparison with the previous characteristic. As expected, although $\lambda_{rms} = \hat{\lambda}_m/\sqrt{2}$, it results that $\hat{J}_{slot} \geq \sqrt{2}J_{slot,rms}$ due to the current distortion caused by the saturation.
5. The magnetizing inductance that will be used in the equivalent circuit is computed as

$$l_m = \frac{\lambda_{rms}}{J_{slot,rms} S_{slot}} \tag{1.15}$$

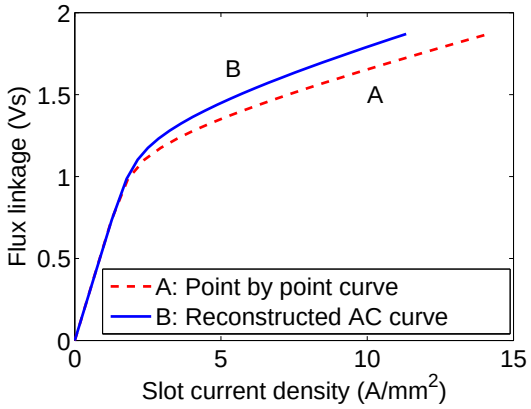

Figure 1.15: Normalized flux–linkage versus current density characteristics: point–by–point curve and reconstructed curve.

1.5.2 Locked rotor analysis

The purpose of this analysis is to determine the rotor parameters to be used in the equivalent circuit. It has been proved that a simulation of a pure single–phase motor gives a rough estimation of these parameters [44]. Thus, a symmetrical two–phase motor is considered for their determination. A second winding is added in quadrature with the first one, as sketched in Fig. 1.17. The two windings are fed by currents of the same magnitude but out of phase by $\pi/2$ electrical radians so as to achieve a rotating field.

From the field solution, the rotor Joule losses P_{jr} and the magnetic energy W_m are computed, the equivalent resistance and inductance are given by:

$$r_{eq} = \frac{P_{jr}}{(\hat{J}_{slot} S_{slot})^2} \tag{1.16}$$

$$l_{eq} = \frac{2W_m}{(\hat{J}_{slot} S_{slot})^2} \tag{1.17}$$

Finally, the normalized rotor resistance $r_{r,bar}(f_r)$ and inductance $l_{\sigma 2D}(f_r)$ are computed as in (1.7).

1.5.3 Three–dimensional computation

As above, the motor parameters computed by means of finite elements are introduced in the equivalent circuit of Fig. 1.13. The latter is completed by introducing the parameters that have not been included in the two–dimensional FE computation. As above, stator resistance, ring resistance, stator end winding and ring leakage inductances are computed. In addition, skewing factor is introduced in the circuit as suggested in literature.

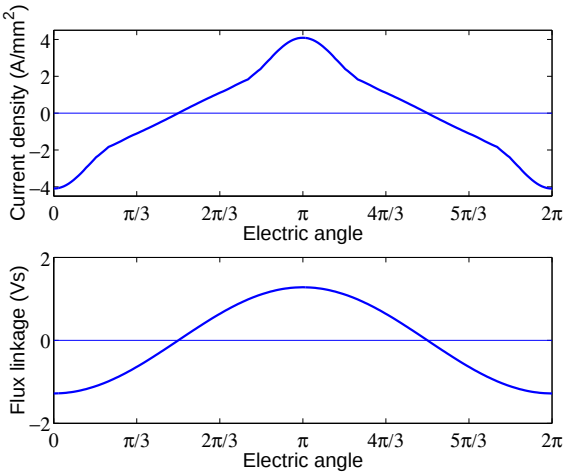

Figure 1.16: Current and flux linkage waveforms. Current waveform is deformed due to the iron saturation.

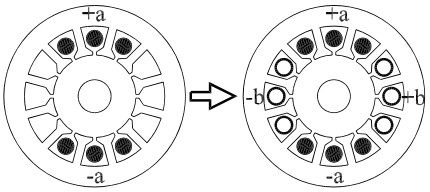

Figure 1.17: Equivalent two–phase motor for the IM parameters determination

The single–phase IM is affected by the space harmonics more than the three–phase IM [45]. As discussed above, the equivalent circuit has to be rearranged introducing the harmonic parameters in series with the fundamental ones [46, 47]. Similarly to the three–phase IM, such harmonic parameters are derived from the fundamental parameters considering the number of harmonics and the corresponding winding factor.

1.5.4 Experiment verification

The proposed procedure is applied to the study of a single–phase capacitor run two–pole 150–W IM. Fig. 1.18 shows a picture of the lamination and Fig. 1.19 shows a picture of the motor with the fan.

The winding of this motor is characterized by a set of possible connections so as to achieve different torque–speed characteristics.

The FE simulations are carried out only one time so as to compute the normalized parameters. For each winding connection, no further FE simulations are

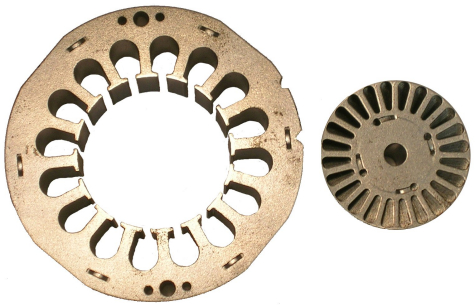

Figure 1.18: Stator and rotor laminations of the single–phase IM. Courtesy of Elektromec

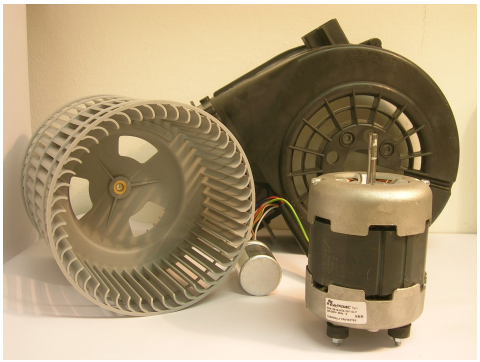

Figure 1.19: The 150–W single–phase IM with the fan. Courtesy of Elektromec

necessary, it is sufficient to update the three–dimensional correction. This makes the analysis fast, saving up much computation time.

Fig. 1.20 shows two flux plots of the magnetostatic and magnetodynamic simulation respectively. Fig. 1.15 shows the corresponding normalized flux–linkage versus current density characteristics. Fig. 1.21 shows the torque vs. speed curves predicted according to the four different connections. The circle–marks curves refer to measurements on the same motor. They confirm the goodness of the proposed analysis procedure.

1.6 Temperature effect on the analysis

The temperature affects the material characteristics and therefore the IM parameters. A precise analysis of the machine requires that we solve together both the electromagnetic and thermal analysis, in order to update the material characteristic of the machine model [4, 5]. This approach will be described in Chapter 3.

As an example, Fig. 1.22 reports the predicted torque characteristic of an IM.

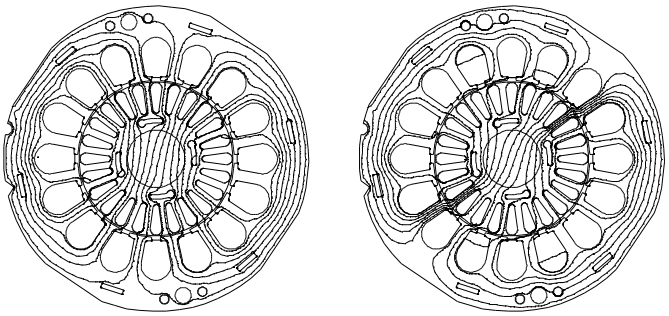

Figure 1.20: Flux plots of two–pole single–phase motor: magnetostatic simulation f_r=0 Hz and magnetodynamic simulation at f_r=25 Hz

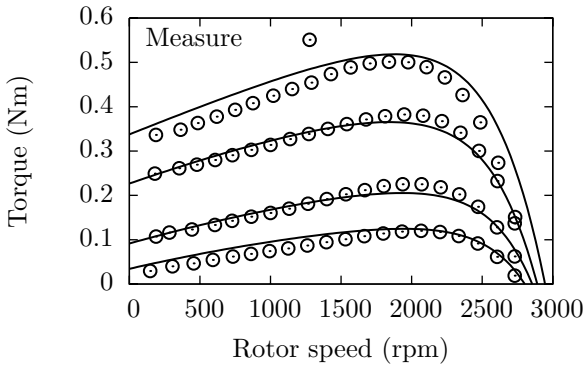

Figure 1.21: Single–phase motor torque versus speed characteristic for various winding connections. Predictions and tests

The simulations have been carried out using a time stepping transient solver. Two temperature values are considered. The motor behaviour is quite different in the two case, this is mainly due to the variations of the resistances.

Therefore, in order to achieve good parameter of the normalized equivalent circuit, it is important to consider proper material characteristics in the FE simulations.

Let us refer to the motor starting. Since the process is swift, the heating effect of the rotor could be considered adiabatic.

In this case, the heat equation for the rotor bars is:

$$P_{jr} = m\ c\ \frac{d\vartheta}{dt} \tag{1.18}$$

where P_{jr} are the Joule losses, m is the mass in kg and c is the specific heat in J/(kg K) of the rotor bars. Using specific quantities and considering the resistivity

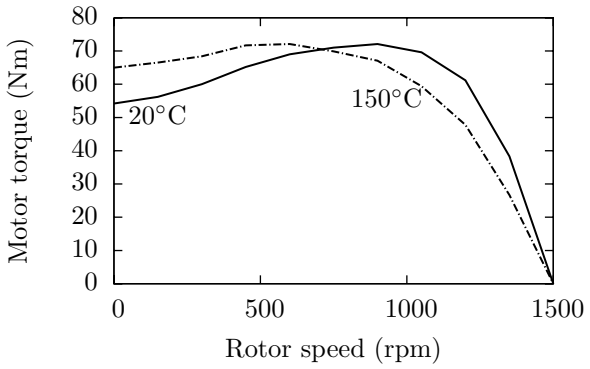

Figure 1.22: Torque versus speed characteristics for different temperature of a three–phase four–pole machine.

of the rotor bars ρ as a function of the temperature, (1.18) become:

$$\rho_0[1 + \alpha(\vartheta - \vartheta_0)]\ J^2 = \gamma\ c\ \frac{d\vartheta}{dt} \tag{1.19}$$

where ρ_0 is the resistivity at the reference temperature ϑ_0, α is the temperature resistance coefficient, J is the current density, and γ is the density in kg/m^3.

The solution of (1.19) is:

$$\vartheta = \vartheta_0 + \frac{e^{t/\tau} - 1}{\alpha} \tag{1.20}$$

with

$$\tau = \frac{\gamma\ c}{\rho_0\ J^2\ \alpha} \tag{1.21}$$

With (1.20) it is possible to estimate the right temperature which has to be used in the FE simulation for achieving the IM parameters. As an example, Fig. 1.23 reports the temperature behaviour of the rotor bars for various value of current density. The considered material for the bars is Aluminum.

Besides the resistivity, the temperature variation affects also the penetration factor of the material. In other words, the frequency behaviour of the motor parameters (like that in Fig. 1.8) depend on the temperature. Therefore, considering different temperatures in the FE simulations may result in different rotor parameters versus frequency curves. This has to be taken into account also when a combined electromagnetic–thermal model is adopted (this case will be considered in Chapter 3).

Let us illustrate this problem referring to a rectangular slot of height h. The penetration factor is defined as [48]:

$$\delta = \sqrt{\frac{\rho}{\pi f \mu}} \tag{1.22}$$

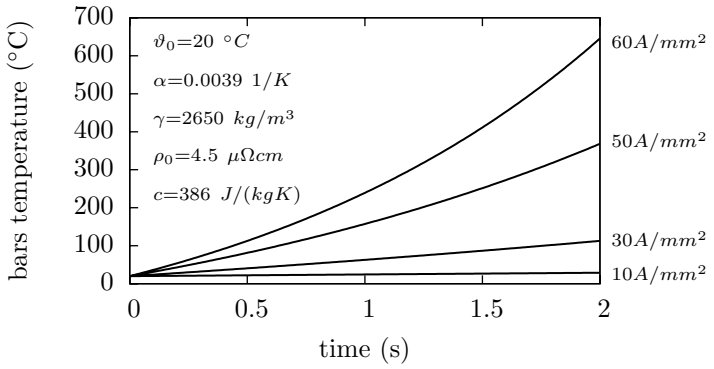

Figure 1.23: Temperature rise of Aluminum rotor bars for different current density in adiabatic conditions

where ρ is the resistivity, f the frequency and μ the permeability. The normalized height is defined as:

$$\xi = \frac{h}{\delta} \tag{1.23}$$

Solving the field equation within the slot, the ratio between the alternating current resistance and direct current resistance is achieved as:

$$\frac{r_{AC}}{r_{DC}} = \xi \, \frac{\sinh\ 2\ \xi + sin\ 2\ \xi}{\cosh\ 2\ \xi - cos\ 2\ \xi} \tag{1.24}$$

The r_{AC}/r_{DC} versus ξ curve is reported in Fig. 1.24. It could be noted that for $\xi \leq 1$ the AC resistance is equal to DC resistance. Then the curve is a straight line. ξ could be understood as the number of δ within the slot height h.

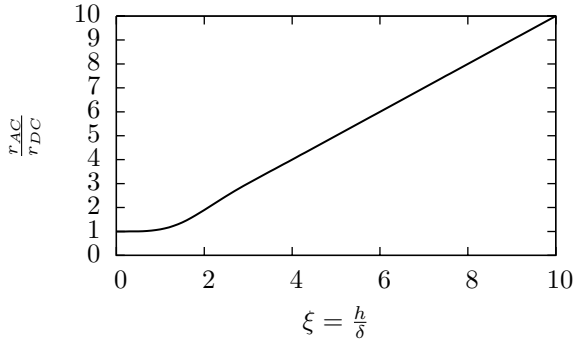

Figure 1.24: Ratio r_{AC}/r_{DC} versus the normalized height ξ.

We now consider a change in the temperature for an Aluminum bar. The

penetration factor at $\vartheta_0 = 20°C$ considering the industrial frequency f=50 Hz is:

$$\delta_0 = 12.5 \text{ mm} \tag{1.25}$$

and the normalized height could be written as:

$$\xi_0 = \frac{h}{\delta_0} = \frac{\sqrt{\pi f \mu}\, h}{\sqrt{\rho_0}} \tag{1.26}$$

A temperature change affects the resistivity and so the normalized height become:

$$\xi = \frac{h}{\delta} = \xi_0 \frac{1}{\sqrt{1 + \alpha(\vartheta - \vartheta_0)}} \tag{1.27}$$

With a typical IM temperature variation of about $200°C$, (1.27) become:

$$\xi = \xi_0 \frac{1}{\sqrt{2}} \tag{1.28}$$

An increment in the temperature implies an increment of the resistivity and a reduction of the normalized height.

From (1.28) we can observe that for $\xi_0 \leq 1$, $\xi \leq \xi_0$ and then $r_{AC} \simeq r_{DC}$ for both ϑ_0 and ϑ. This take place if:

$$h \leq \delta_o = 12.5\text{mm} \tag{1.29}$$

Therefore, if (1.29) is valid the current distribution inside the slot is not affected by the temperature (with the hypothesis above). If (1.29) is not valid, that is if $h > 12.5$ mm, the temperature rise affects the current distribution within the slots. This effect increases as the slot height h increases.

In order to verify this, two motors with different rotor geometries are considered. The slots of the first are 7 mm high while the slots of the second are 20 mm high. For each geometry two temperatures have been considered, $20°C$ and $300°C$. The rotor resistance has been computed for various frequencies on the basis of the rotor losses. The simulation results are shown in Fig. 1.25.

Curves **a** reports the rotor resistances computed from the FE simulations at $20°C$. Curves **b** reports the rotor resistance computed from the FE simulations at $300°C$. Curves **c** reports the rotor resistances at $300°C$ starting from the FE simulation at $20°C$ and computing the resistivity increment with the temperature, that is:

$$r_{r,bar-c} = r_{r,bar-a}\ (1 + \alpha(\vartheta - \vartheta_0)) \tag{1.30}$$

For the slot 7 mm height, curves **b** and **c** are quite close, that is the temperature variation does not affect the distribution of the current density within the slot.

For the slot 20 mm height, curves **b** and **c** are very different. The temperature affects the shape of the rotor parameters curve. In fact, an increment of the temperature is similar to a decrement of the frequency, that is, the skin effect is smaller and the resistance is quite constant with the frequency. This effect is not present at low temperature, and the analytical correction by means of (1.30) does not consider this variation of the skin dept yielding wrong rotor parameters.

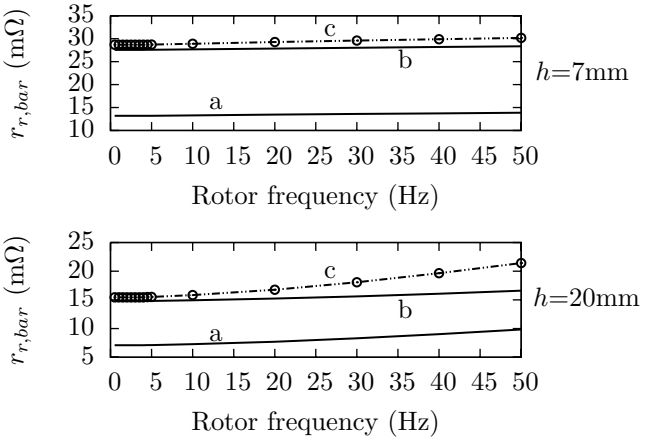

Figure 1.25: Rotor resistance computation at different temperatures. Two slot heights are considered

Therefore, when the parameters of the IM equivalent circuit are achieved by means of FE simulations, it is important to use proper material characteristics, in order to take into account the temperature effects. This is particularly important in machines with slot height greater than the penetration factor (see (1.29)).

1.7 Conclusions

In this Chapter, a procedure that combines FE and analytical computations to predict the IM performance has been described. FE analysis is used to estimate the two–dimensional parameters of the motor, while the three–dimensional ones are computed analytically. Then the IM performance is predicted from the settled equivalent circuit.

The proposed strategy has been adopted for the study of a three–phase as well as a single–phase IM. For both motors, the predictions satisfactorily match the experimental results.

A key issue of the proposed procedure is the choice of normalized parameters that makes the analysis independent of the actual motor length and number of turns per phase. Then, the achieved results are associated only to the given lamination geometry and the winding distribution, so that they can be easily extended to motors of different voltage and power rating.

Chapter 2

Application Examples of the Combined Analytical–FE Analysis

Abstract– In this Chapter, some application examples of the model described in Chapter 1 are presented. At first a series of induction motor for standard applications is considered. The lamination is analyzed, and then the motor performance is achieved for different power ratings.

Next an induction machine for an elevator system is considered. In this type of application, the geometry is not optimized to achieve optimal IM performance for a given power rating, but is designed to achieve "adequate" performance for a complete set of various power ratings.

2.1 Introduction

IN CHAPTER **??**, a combined FE–analytical model for the prediction of IM performance has been presented. Thanks to careful choice of the analysis quantities, the FE simulations results are bound to the lamination geometry and not to a particular power rating. In this way, the obtained results can be adopted for any IM formed by the same lamination geometry and winding distribution. In many real cases, the design of the electrical motor is limited to the selection of commercial laminations. In these cases, the described procedure is well suited since it proves to be rapid and accurate at the same time. An example of this type of application is given in Sec. 2.2

Another application example is considered in Sec. 2.3, where the design of a series of induction machines for an elevator system is considered. In this case, adoption of a single geometry for a series of machines allows the designer to limit the cost of the lamination stamp. Since the particular application of the induction machines in this case, the requirements of the application are first introduced, and then particular care is given to the design constraints. Also in this case, experimental tests on some IM prototypes confirm the accuracy of the predictions.

2.2 Standard lamination performance prediction

In this section the same lamination analyzed in Sec. 1.4.5 is considered. Fig. 1.9 shows the lamination geometry and the flux lines for two different simulations. Fig. 1.6 and Fig. 1.8 show the normalized equivalent circuit parameters computed from the FE simulations.

Three different power ratings are considered. Each motor size is realized by changing the stack length L_{stk} and rearranging the number of conductors n_{cs}. Table 2.1 reports the main data of the motors.

Table 2.1: The characteristics of the three IM considered in this section

Power rating (kW)	L_{stk} (mm)	n_{cs}	Stator resistance (Ω)
2.2	100	46	5.13
3.0	120	38	3.19
3.7	130	33	2.41

The normalized equivalent circuit is particularized for each motor computing the actual three dimensional parameters as described in Sec. 1.4.3. Then it is solved and the performance of each motor is computed. The main performances are reported in Fig. 2.1 where prediction and measurements are compared.

Fig. 2.1(a) shows the predicted torque and current characteristic of the IM of 2.2 kW. Measurements are reported with circle marks. Similarly Fig. 2.1(c) and

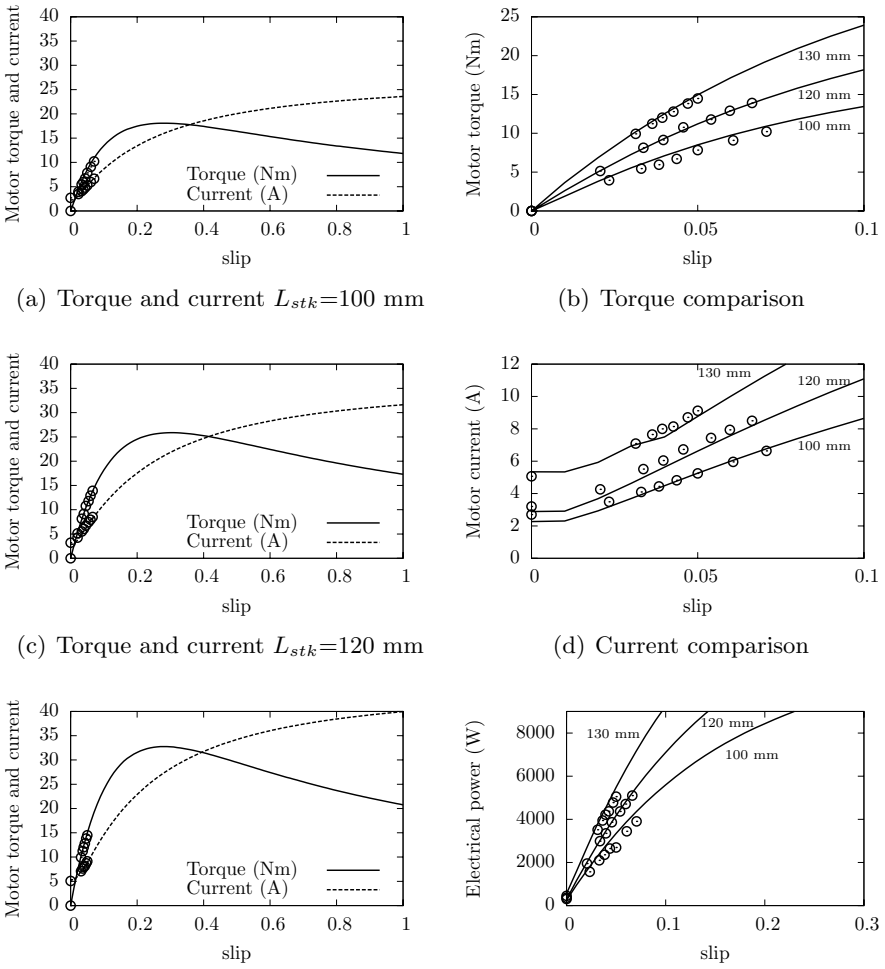

(a) Torque and current L_{stk}=100 mm

(b) Torque comparison

(c) Torque and current L_{stk}=120 mm

(d) Current comparison

(e) Torque and current L_{stk}=130 mm

(f) Electrical power comparison

Figure 2.1: Prediction and measurements comparison for different stack length. Measurements are reported with circles

Fig. 2.1(e) for the other motor sizes. Fig. 2.1(b) shows the comparison of the three motor torque characteristics. The same comparison is reported in Fig. 2.1(d) for the motor current, and in Fig. 2.1(f) for the electrical power. Measurements are reported with circles. Very good agreement can be noted for all the characteristics.

2.3 Design of an IM set for elevator system

In this section the design of a set of IM's for elevator systems is considered. The IM stator contains two three–phase windings of different number of poles: one for low speed (typically 8 or 16 poles) and the other for high speed (2 or 4 poles). This requires a large slot area, which is often higher than the slot area of the common stator laminations. A study is required for each windings.

A 5–kW IM has been properly designed for this application. Fig. 2.2 shows the stator and the rotor of the IM. Fig. 2.3 shows a picture of the stator lamination.

Figure 2.2: Rotor and stator of the realized motor for the elevator system. Courtesy of EME spa.

In addition, as in the most of applications, there are constraints on the external geometry of the machine. This is fixed by the mechanical structure of the application. In an elevator system the operating cycle is intermittent: starting and stopping follow one another continually. As far as the IM design is concerned, the main consequence is that the conductor cross-sectional area and the iron paths are designed forcing high electric and magnetic loadings. This requires an accurate

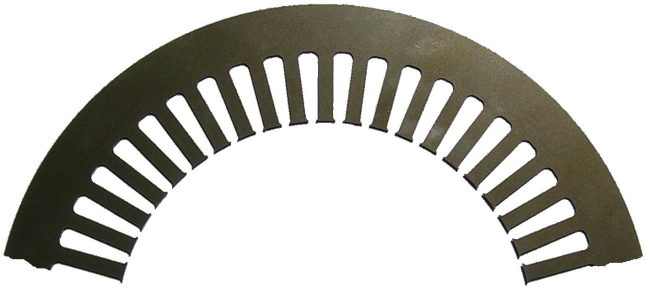

Figure 2.3: The stator lamination of the considered motor series. A large cross sectional of the slots is evident.

magnetic model of the IM to get good predictions of its performance. Therefore, this justifies the choice of an FE analysis that properly considers iron saturation and irregular geometry. However, the time required for the computation (mainly due to the FE simulations) has to be reasonably short.

A further requirement to the elevator system is to be able to set off at full load, that is, with an adequately high starting torque. A direct consequence is that the IM design requires an accurate optimization of the rotor cage geometry. Since the same lamination is used for IM of various power ratings, in order to realize only one lamination stamp, the design has to consider the performance of all motor sizes.

2.3.1 Coupled magnetic–thermal analysis

In an elevator system, the operating cycle is not continuous and the IM has to guarantee a given number of startings and stops per hour. The intermittent operating cycle allows the electric and magnetic loading of the motor to be increased up to the maximum temperature rise of the windings, i.e. the average losses have to be compatible with the cooling system capability. A step by step analysis including the actual dynamics of the IM during each start and stop of the elevator is particularly time consuming. It requires a lot of time, especially if it is linked with an optimization of the motor geometry. A faster analysis can be carried out based on the following considerations, obtaining a good approximation of the average losses.

At first, let us remember that the thermal time constant is significantly higher than the electrical one. Therefore the average losses of the motor can be considered instead of the instantaneous ones to estimate the temperature rise. In addition, in order to avoid abrupt departure of the elevator system, a large inertia is present at the mechanical shaft, as depicted in Fig. 2.4.

Hence, the electric dynamics is neglected, and only the mechanical dynamics is considered. Thus, the IM is assumed to work in successive steady state operating points.

For a given load (i.e. fixing a torque T_{load} constant with the speed) and

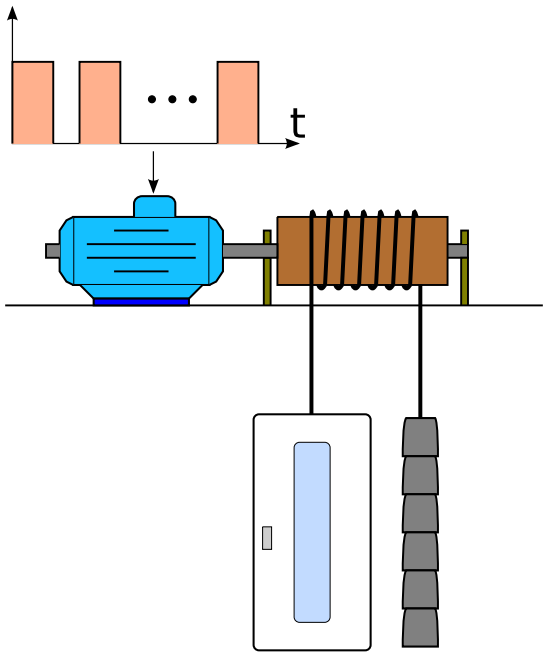

Figure 2.4: Typical installation of elevator system. A large inertia is present at the mechanical shaft.

knowing the IM torque to speed characteristic, obtained from the electromagnetic analysis, the speed ω_m is given by

$$\omega_m(t+dt) = \omega_m(t) + \frac{T_m - T_{load}}{J'_m} dt \tag{2.1}$$

where $T_m = T_m(\omega_m)$ is the IM torque at such a speed ω_m and J'_m is the total inertia, reported at the motor shaft.

The motor is assumed to remain at the speed $\frac{1}{2}[\omega_m(t+dt) + \omega_m(t)]$ for the time dt. At such a speed the losses are $P_{Joule}(\omega_m)$ and $P_{iron}(\omega_m)$. Finally, the total power loss during the motor start are computed as

$$P_{L,start} = \frac{\sum (P_{Joule} + P_{iron}) dt}{\sum dt} \tag{2.2}$$

where $\sum dt$ means the total starting time t_{start}.

2.3.2 Torque and current characteristics

Some experimental tests are carried out in order to verify the results achieved by the proposed analysis. Some comparisons are presented in this section. It is worth noticing that, once the FE analysis is completed, all elaborations and optimizations require a few seconds to be achieved.

Fig. 2.5 shows the flux plots with both winding connections. The IM symmetry allows the study of half a machine only to be carried out, reducing the FE computation time [17].

Fig. 2.6(a) shows the torque and the current versus slip curves, considering the four–pole winding connection. Fig. 2.6(b) shows the same characteristic for the 16–pole winding connection.

Solid lines refer to the results of the equivalent circuit obtained from the proposed analysis that combines FE and analytical computations (see Fig. 1.3) while circles are measured values. The test at unity slip has been carried out at lower voltage and then current and torque are reported at nominal voltage. A reasonable agreement can be noticed, in spite of the high magnetic and electric loadings. A high dependence on the rotor cage temperature has been observed. The slight discrepancy between simulations and tests is because the simulations are carried out at given temperature while the latter might be changed during the test.

As a further comparison, the squares in Fig. 2.6(a) and 2.6(b) are the FE checks where stator current and rotor frequency are computed by means of equivalent circuit and imposed as sources in FE analysis.

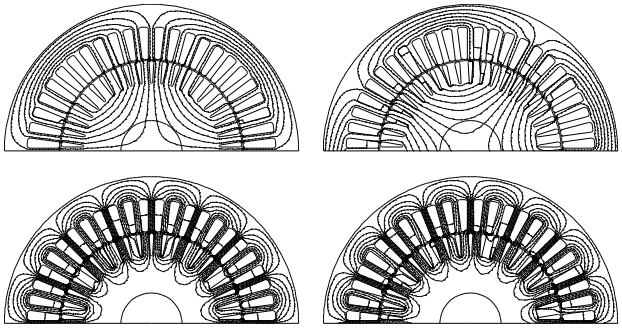

Figure 2.5: Flux plots of the motor with 4–pole and 16–pole winding connections. On the left hand side, simulations at f_r=0 Hz. On the right hand side, simulations at f_r=5 Hz.

2.3.3 Motor with different length and number of conductors

Using the normalized equivalent circuit, a rapid prediction of the performance of several motors manufactured with the same lamination geometry and the same winding distribution can be achieved. This is the basis for the optimization of a complete set of IMs of different power ratings.

As an example, Fig. 2.7 shows the torque characteristic of three motors with different stack lengths (solid line): L_{stk} equal to 40, 80, and 160 mm respectively. The number of turns is chosen to be inversely proportional to the stack length.

The analysis can be rapidly carried out changing the number of turns of the winding, or the motor performance can be predicted at different voltage. Fig. 2.7

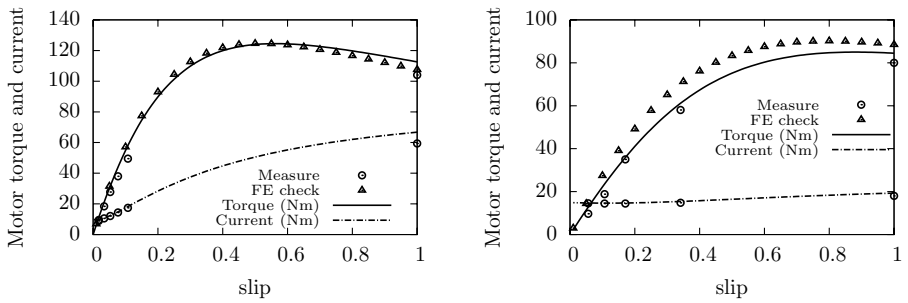

(a) 4–pole connection (b) 16–pole connection

Figure 2.6: Torque and current versus slip curves of the 5–kW IM

shows by dotted lines the torque versus slip behavior according to a decrease of the supply voltage of 10%.

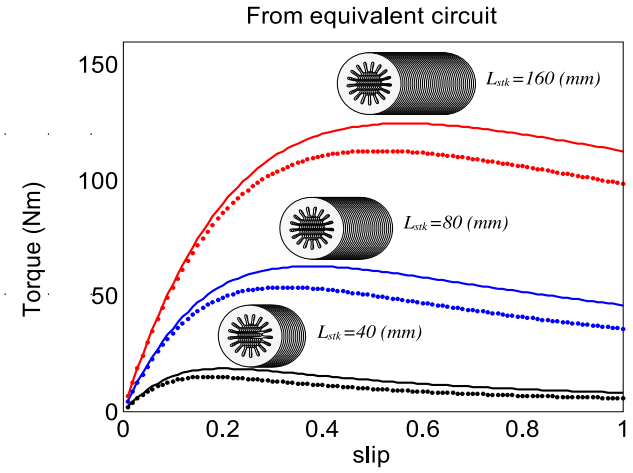

Figure 2.7: Simulation of three motor with the same lamination geometry, changed stack length and rearranged number of turns.

Similarly, the IM model is used to predict the performance of the elevator system assuming different load conditions. As above, these analysis are very rapid since they are based on analytical computation without any additional FE simulations.

Fig. 2.8 shows the rotor speed rise during motor starting computed by (2.1). Two different loads are considered in order to highlight their impact on start up. For each load three different inertias are considered: J'_m equal to 1.5, 2.5, and 3.5

kgm^2. From Fig. 2.8, it could be noted the different running speeds related to the different load torques and the different starting times for each inertia.

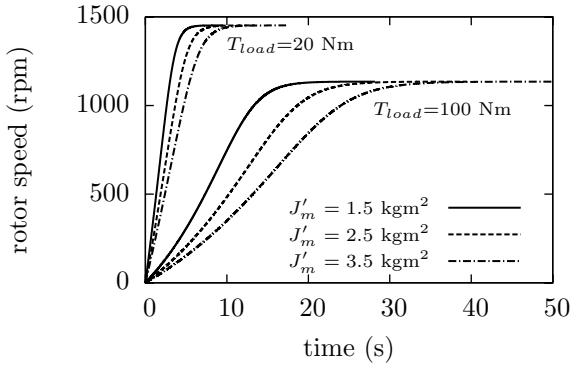

Figure 2.8: Simulation of different start transients of the motor.

2.3.4 Evaluation of the impact of change of length and number of conductors on the motor efficiency.

The adopted analysis procedure allows a rapid study of the impact of the changes of both the IM stack length and the number of the conductors. As an example, Fig. 2.9 shows the IM efficiency, as a function of the stack length and the number of conductors per slot. Each operating point refers to motor operation at the same load torque.

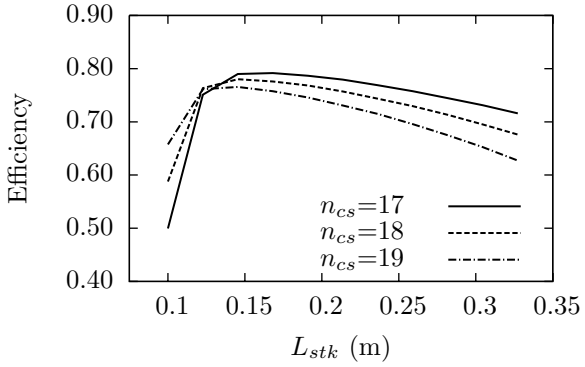

Figure 2.9: Efficiency for various stack length and conductor number for given output power.

2.3.5 External heat flow verification.

When the operating cycle is fixed, it is also possible to verify that the average losses during the starting and operating time are carried out by the cooling system. It should be verified that

$$\frac{P_{L,start}t_{start} + P_{L,on}t_{on}}{t_{start} + t_{on} + t_{off}} \leq P_{therm} \tag{2.3}$$

2.3.6 Turn off time estimation for intermittent operations.

For a fixed mechanical load, the starting time and the total losses during starting can be computed as described in Section 2.3.1. With given external heat flow P_{therm}, the operating cycle can be estimated imposing the time in which the motor is switched off, as

$$t_{off} = \frac{P_{L,start}t_{start} + P_{L,on}t_{on} - P_{therm}(t_{start} + t_{on})}{P_{therm}} \tag{2.4}$$

where $P_{L,start}$ is computed by (2.2), with $t_{start} = \sum dt$, and $P_{L,on}$ are the total losses at the operating point, and t_{on} is the motor operation time. Table 2.2 reports an example of various t_{off} times computed from (2.4), as a function of different t_{on}.

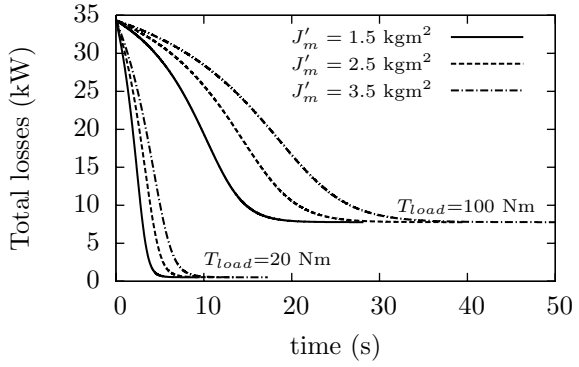

Figure 2.10: Total motor losses during starting.

Fig. 2.10 shows the total motor losses during starting. Also in this case, the prediction of the IM performance are based on the equivalent circuit that has been derived previously. Therefore, since they require only an analytical computation, they are achieved in a few seconds. As in Fig. 2.8, it could be noted the impact of the inertia on the starting time and the impact of the load torque on the total losses.

Table 2.2: Turn off time estimation for a given mechanical load. Various operation times t_{on} are considered.

$P_{on} = 530$ W $P_{therm} = 400$ W						
$T_{load} = 20$ Nm $J'_m = 2.5$ kgm^2						
$n = 1451$ rpm $P_{L,start} = 8031$ W $t_{start} = 9.54$ s						
t_{on} (s)	10	20	30	40	50	60
t_{off} (s)	185	188	192	195	198	201

2.4 Conclusions

In this Chapter, two real application examples of the model described in Chapter 1 have been presented. At first a series of induction motors for standard applications is considered. Three power rating have been analyzed: 2.2, 3.0 and 3.7 kW. For each motor size, experimental test data has been presented in order to confirm the accuracy of the proposed model.

Then a series of induction machines for elevator system have been considered. For this application the mechanical start transient and thermal verification have been presented. These two aspects are important for a good design in this application, and the adopted model allow one to consider them in a rapid and accurate way. The predictions achieved with the proposed strategy match satisfactorily the experimental results.

Chapter 3

A Coupled Thermal–Electromagnetic Analysis for a Rapid and Accurate Prediction of IM Performance

Abstract– The design of electrical machines for extreme operating conditions must include a thermal analysis coupled with the magnetic analysis. However, the traditional coupling of the thermal and the magnetic models can result in an unacceptable increase in computation time, especially if finite elements are used for the machine analysis.

This Chapter describes a coupled thermal–magnetic analysis of an induction machine with the primary goal of achieving a rapid and accurate prediction of its performance. For the electromagnetic analysis, the normalized equivalent circuit of Chapter 1 is adopted. Its parameters are non linear and are adjusted on the basis of the operating point. Then, this equivalent circuit is coupled with a lumped parameter thermal network to predict the temperature in each part of the IM.

Since both the equivalent circuit and thermal network solutions are analytic, the analysis converges very rapidly. At the same time, the finite element analysis yields a precise estimation of the IM parameters used in the equivalent circuit.

3.1 Introduction

THE modern challenge of an electrical engineer is to design electric devices that are suitable for operation in demanding applications. There are some reasons to explain this trend. Primarily, there is an economic interest in increasing the power density of the machine: this means reducing the machine dimensions for a given power, and for increasing the performance of a machine of a given size. Secondly, there is the need to employ the machine in severe external conditions, such as high temperature, pressure, and so on.

However, such a choice of operating the design to the maximum limits yields a corresponding increase in the operating temperature of the machine. As a consequence, it is necessary: (i) to adopt insulating materials that are well suited for high operating temperatures, and (ii) to improve or to redesign the cooling system of the machine.

During the design stage, the thermal analysis assumes a key role in maximizing the power density of the electric motor. A correct prediction of the temperature rise in each part of the machine leads to the maximum exploitation of the materials and, consequently, the highest performance of the machine.

In addition, the thermal analysis has to be not only accurate but also rapid in order to be included in a process of parametric analysis and optimization of the machine. To this end, an analytical approach based upon a lumped parameter network is preferred to the finite element thermal analysis.

In addition to the standard performance concerns mentioned above, thermal analysis is also important for machine control aspects. For instance, in field orientation techniques for induction motors, the control methods depend upon the motor parameters, particularly on the rotor resistance and magnetizing inductance. Errors in the estimation of these parameters translate directly to errors in field orientation [49]. The magnetizing inductance can be considered constant if the flux level is kept constant and it can be easily mapped to the flux level by a saturation function if flux is variable. The rotor resistance varies as a function of skin effect and rotor temperature, however the later is unmeasurable in practical conditions. Since the machine parameters change continuously as a function of temperature, it is important to know the exact parameter values at the actual operating point [50].

In this Chapter attention is given to the characterization of an induction motor, designed to operate in severe conditions. A coupled thermal–magnetic analysis for rapid and accurate prediction of IM performance is proposed. The strategy is to combine the normalized equivalent circuit of Chapter 1 with an analytical thermal analysis of the motor.

The finite element analysis calculates the iron saturation at various magnetizing currents and the current density distributions within the rotor slots at different rotor frequencies [14]. A few FE simulations are carried out to get the more significant motor parameters. Then the IM performance is computed by solving the lumped–parameter electric and thermal models. Since the electric and thermal models are coupled, the electric parameters are iteratively updated on the basis of the temperature computed by means of the thermal model, the latter receiving

the motor losses as heat sources from the electric model.

Therefore a rapid and accurate prediction of the performance is achieved at the same time. The IM model that results is accurate enough to allow good prediction of the motor parameters, with a minimum of computation time. As one would expect the most computationally intensive portion of the analysis is the finite element simulations.

3.2 Examples of applications

There are many applications requiring high power density IMs. Among them, traction and propulsion motors are those in which the reduction of volume and size are imperative. Fig. 3.1(a) shows a sketch of an IM for ship propulsion. The external frame of this IM is water–cooled. Since the stator lamination is in constant contact with this cold fluid, the iron losses, in the inner part of the stator are allowed to increase to the temperature limit. In addition, an inner rotor fan is mounted on the shaft so as to force air within ducts to cool the rotor parts and then to transfer the heat to the external water by means of a heat exchange system. As a result of these two cooling systems working in parallel, the power density of the IM is very high.

It is worth noting that the design of such an IM requires the thermal and electromagnetic analysis to be carried out at the same time. A representative thermal network of such a machine is sketched in Fig. 3.1(b). The heat is transferred to the cooling water, flowing around the stator, directly through the stator contact with the frame and through the air circulation within the motor. A similar cooling system is used in large machines designed for traction, wind power generator and/or elevator systems, often forced oil is used as the external cooling fluid.

Another family of machines with a non conventional cooling system is represented by IMs for submerged pumps. Both motor and pump are designed with a small diameter and large length, so as to limit the well diameter. Fig. 3.2 shows a sketch of this type of machine. Since the motor operates completely submerged within the fluid (typically water), it is automatically cooled by the fluid that is evacuated by the connected pump.

When the well is very deep, the pressure of the external fluid could deform the motor frame. To avoid deformation the IM is filled with a mixture of water and antifreeze and thus, can theoretically work at any depth. However, the presence of the fluid within the stator influences the choice of the insulating materials, the internal heat exchange, and consequently the machine operation. For instance varnish cannot be used to insulate the winding conductors, and a waterproof insulator such as PVC has to be used [51]. Such a material exhibits inferior thermal properties to varnish and as such has a large impact in the IM design process.

Once again, an accurate thermal analysis of the machine is a key necessity to predicting and maximizing the machine performance. The representative thermal network of such a machine is sketched in Fig. 3.2. The heat is transferred to the external water by way of flowing through the stator and the internal fluid.

In light of these considerations we strongly conclude the necessity of combining the thermal and electromagnetic analysis of the machine. The model begins with

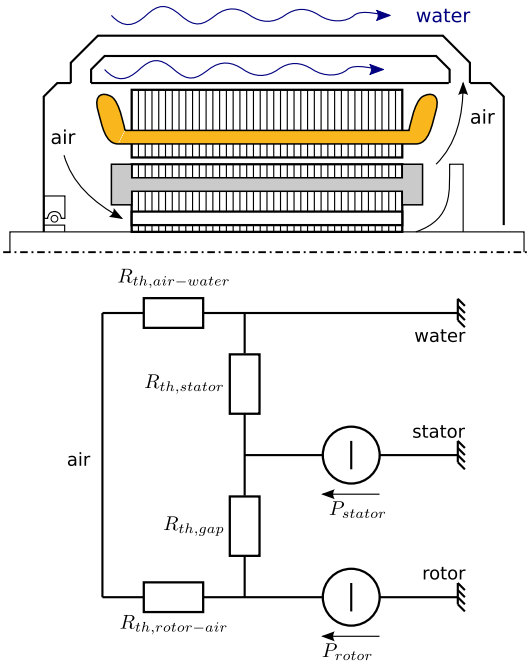

Figure 3.1: Example of a ship propulsion induction motor

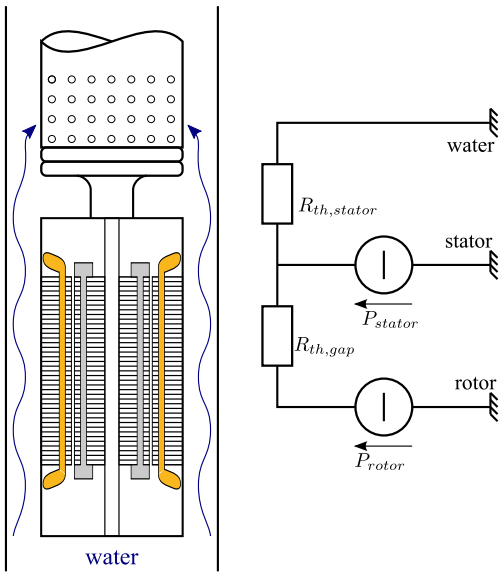

Figure 3.2: A sketch of the structure of a submerged pump

the thermal indications found in specialized literature and depending upon the IM application the thermal network is suitably modified. In some instances FE simulations are used to calculate thermal parameters that are then introduced in the analytical lumped–parameter network. An example of which is given in Section 3.5.

In Fig. 3.3(a) a picture of a commercial submerged pump is shown [52]. Fig. 3.3(b) shows the IM of the pump and Fig. 3.4 shows the endwinding of the motor.

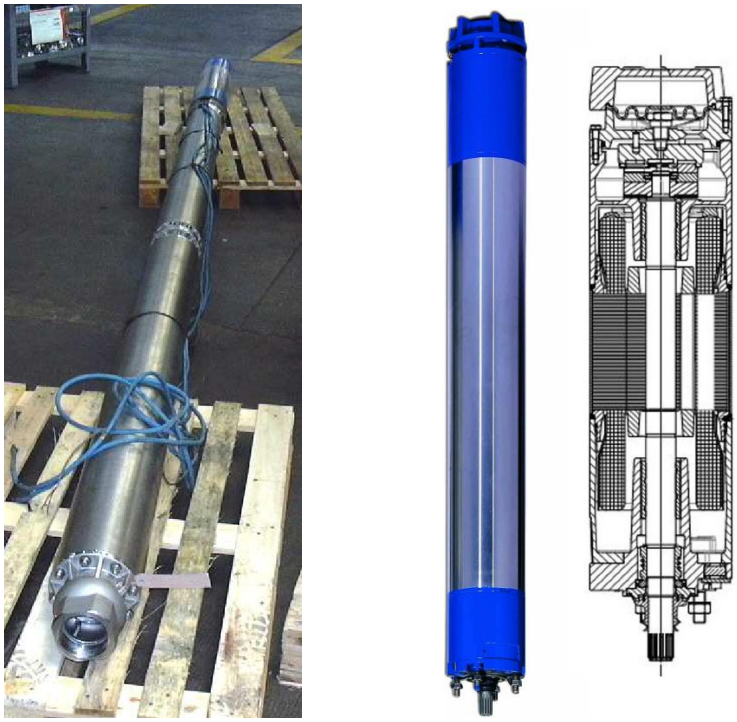

(a) Complete pump (b) Electric motor

Figure 3.3: Picture of a submerged pump. Courtesy of Lowara.

3.3 Analysis procedure

The flow–chart of the entire analytical model is sketched in Fig. 3.5. Starting from the IM data and the operating conditions, the normalized equivalent circuit is achieved as described in Chapter 1. In Fig. 3.5 the same block of Fig. 1.2 are present.

Then, a lumped parameter thermal model of the motor is built. The thermal computation is tightly bound to the electromagnetic analysis. A detailed descrip-

Figure 3.4: The end winding of the submerged pump IM. Courtesy of Lowara.

tion of the thermal model and the link between it and the electromagnetic model will be given in the next Section.

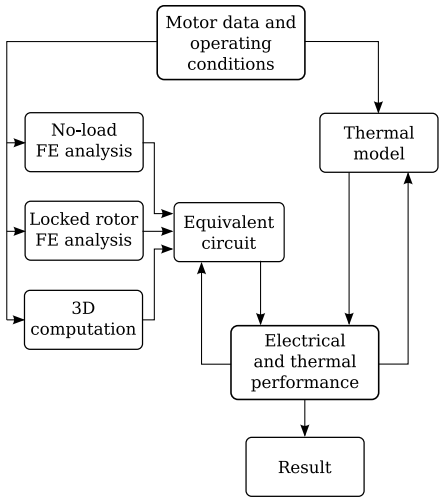

Figure 3.5: Flow chart of the IM thermal–magnetic analysis

3.4 Coupled thermal network

For the study of the thermal behaviour of an industrial IM, several lumped parameters thermal networks have been proposed. For example, in [53] a detailed thermal network is introduced which describes the temperature in any machine part, both axial and radially.

Fig. 3.1 and Fig. 3.2 show a very simple thermal network, in actuality anal-

ysis networks with more than twenty nodes are used. Using matrix notation the solution is achieved solving the system:

$$[G_{th}][\theta] = [P_{loss}] \tag{3.1}$$

where $[G_{th}]$ is the matrix of the thermal conductances, $[\theta]$ is the column vector of the temperature rise and $[P_{loss}]$ is the column vector of the losses.

Using the proposed thermal network, thermal dynamic analysis can also be performed [53, 54]. In this case thermal capacitors are added to the network. A generic $i-$th thermal node is represented as shown in Fig. 3.6. For each node it is possible to write the following relation:

$$\theta_{i(k+1)} = \theta_{i(k)} + \frac{\Delta t}{C_i}\left[P_i - \sum_j G_{ij}(\theta_i - \theta_j)\right] \tag{3.2}$$

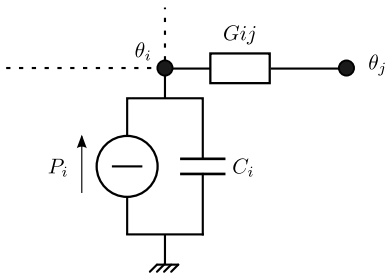

Figure 3.6: Scheme of a generic thermal network node in the dynamic case

Once the thermal network is assembled, it is possible to compute the temperature behaviour of the motor. Moreover, the electromagnetic and thermal analysis are strictly correlated. Starting from the initial value, the motor performance is computed at a given operating point. From the equivalent circuit, the motor losses are computed and used as heat sources in the thermal model. Solving the thermal network, the temperature rise is computed in the various machine parts and the electrical parameters of the equivalent circuit are updated. Repeating this process until convergence, the operating conditions of the motor are achieved. This process is sketched in Fig. 3.7.

Discontinuous operating cycles of the motor can be also taken into account. The thermal and electromagnetic models are solved jointly adjusting power losses and temperatures. An example will be given in Section 3.6.

It is worth noticing that each computation is carried out using the analytical models of the machine. Therefore, each computation requires a few seconds of both the continuous and discontinuous operating cycles.

In addition, an advantage of using a normalized model of the IM is that any variation of stack length and number of winding turns can be immediately ad-

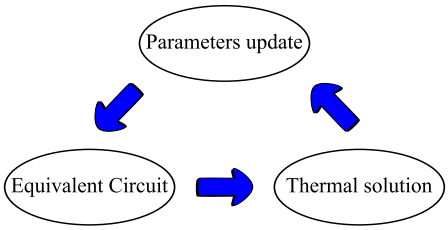

Figure 3.7: Flow chart of the combined electromagnetic–thermal IM analysis

dressed. This is very useful in any optimization process, especially from an industrial point of view.

3.5 Computation of the thermal network parameters

In order to obtain an accurate thermal prediction, a good estimation of the thermal parameters is necessary. Many past works give careful guidelines [21, 53, 55]. For example for the computation of the convective exchanges, empirical relations based on adimensional parameters are used. They are based on experience and experimental test, and there is a wide variety of relationships which depend both upon the considered phenomenon (natural convection, forced convection, etc.) and on the system geometry.

In any event, when information is missing for a particular application, the finite element analysis can fill the gap. Therefore suitable FE thermal analyses are carried out for predicting the necessary thermal parameters. Even in this case, a FE thermal analysis of the whole machine is avoided, so as to reduce the computation time. The strategy is to use the FE analysis to determine the parameters of the thermal network as precisely as possible, and then use this network for the computation of IM temperatures under each operating condition.

In the following, this approach is used for the computation of the thermal parameters of a submerged pump as sketched in Fig.3.2. As the machine for this application is non standard (see Section 3.2), the thermal networks presented in literature have to be modified. The computation of the particular parameters and the modifications of the thermal network are now illustrated.

Let us consider the slot winding thermal resistance. In order to consider the wire insulation in the slot thermal resistance, in [21] a corrective factor $F = \lambda/\lambda_{ins}$ is defined, where λ is the equivalent thermal conductivity and λ_{ins} is the insulating thermal conductivity. In [21] the value of the factor F is reported considering conductors with varnish insulation.

When, as is the case in our example, the slot is filled by cooling water and PVC insulation is used, the factor proposed in the literature is not suitable. Using FE simulation, the estimation of the corrective factor F is updated, for the

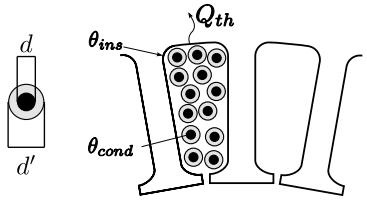

Figure 3.8: A sketch of the stator slot considered in the FE simulation

actual conditions. Fig. 3.8 shows the stator slot cross section considered in the FE simulation together with a sketch of a single conductor and its PVC insulation. A fixed heat source (due to the Joule losses) is imposed in each conductor of the slot. Then the heat flow Q_{th} through the slot insulation is computed and the thermal resistance related to the winding in the slot can be computed as:

$$R_{th} = \frac{\theta_{cond} - \theta_{ins}}{Q_{th}} \tag{3.3}$$

where θ_{cond} is the average temperature of the conductors in the slot and θ_{ins} is the imposed temperature in the slot insulating sheet.

The factor F is estimated as:

$$F = \frac{1}{2\pi\lambda L_{stk} R_{th}} \tag{3.4}$$

In this way the correction factor F can be computed also for the thermal network of a non conventional machine.

In Fig. 3.9 the correcting factor F is reported for a traditional slot with varnish and for a slot filled with water. As expected, a higher value of equivalent conductivity is found in the second case.

Various values of the wire diameter ratio d/d' have been considered, where d is the wire diameter and d' is the insulated wire diameter. The computed values of F by means of FE simulations for the traditional machine agree with those reported in [21].

The presence of water inside the motor also influences other thermal parameters.

Since the motor is mounted in an upright position, a convection resistance in the stator slots has to be added to account for the natural convection among the stator slots and the endcap water. This resistance directly connects the stator slot winding with the endcap water and is computed using the classical–empirical natural convection relationship.

Also in the endcap the presence of water improves the thermal exchange and this has to be considered in the thermal network. The convective coefficient inside the endcap is computed again using empirical relationships for convection, with

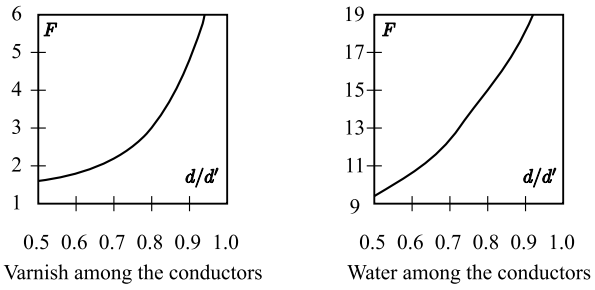

Figure 3.9: F corrective factor as a function of diameter ratio. Left: traditional slot with air among the conductors [21]; right: slot filled by water, PVC insulated wires.

consideration given to the actual water speed. The latter is computed by starting with the rotor speed and applying correction coefficients.

Due to the friction among the water and the rotor, mechanical losses arise in the endcaps. Therefore, in order to take this into account a loss generator has to be added. This loss can be estimated from the no load test of the motor by separating the iron losses of the machine.

Finally a thermal capacitor has to be added to represent the thermal capacity of the endcap water.

Once the endcap model has been developed, it can be used for any motor that exhibits this same endcap. This is common in industrial applications where one lamination geometry is often used for a series of IMs with varying stack lengths.

3.6 Experimental validation

In order to illustrate the proposed procedure, a 22 kW submerged pump is described. A sketch of the pump is reported in Fig. 3.2. The motor is filled with a mixture of water and antifreeze, thus an accurate thermal analysis of the machine is necessary to predict the machine performance.

In particular, starting from the models proposed in the literature, a specific thermal network has been developed taking care to update the parameters (see Section 3.5) in order to take into account the peculiar thermal exchanges in the machine.

Some thermal conductances are added in order to represent additional thermal flows due to the presence of the water.

Moreover, the friction due to the rotating water gives rise to additional losses, which have to be added into the thermal network. A crucial parameter for the thermal model is the slot thermal resistance. In order to obtain a precise estimation, FE simulations are used. The curve reported in Fig. 3.9 is used.

The entire model for the coupled thermal–electromagnetic analysis has been implemented in C++.

To assist in the goal of validating the model, the motor has been equipped with some thermocouples. The temperature has been measured in the middle of the external frame, in the middle (and at middle radius) of the stator back iron, in the middle (between conductors) of the slot windings, and in the water of one endcap.

As far as the experimental validation is concerned, first the data for continuous operation is introduced, and then the intermittent operating data is considered.

3.6.1 Continuous running

The pump operates at nominal power, i.e. 22 kW. For a given rotor slip, the performance of the motor is computed. The electrical circuit and the thermal network are iteratively solved until convergence is achieved. In this way both the electrical and thermal behaviour of the machine is considered.

The results of the simulations are compared with the measurements of the motor. Table 3.1 reports the measured and predicted temperature rises for various machine parts. Good agreement between the data can be noted.

Table 3.1: Comparison between measured and predicted temperatures in various machine parts. Continuous running operation.

Motor part	Measurements (°C)	Prediction (°C)
Frame	41.1	41.4
Stator Back Iron	44.3	48.3
Slot Winding	58.5	61.6
Endwinding	50.5	53.7
Endcap Water	55.5	52.7
Winding Average	62.2	62.2

Fig. 3.10 shows the comparison between predicted (solid line) and measured (circles) temperatures of the external frame and endcaps. Good prediction of the frame temperature is achieved while for the endcap temperatures a 4–K discrepancy is noted. Let us observe that the actual temperature of the two caps is different, this is due to the vertical position of the pump. The thermal model predicts the average temperature while the measurements refer to the hottest cap.

Fig. 3.11 reports the predicted and measured temperature for the slot winding and the back iron. The simulated slot winding temperature differs slightly with respect to the measurement. Since the thermocouple gives local information, a better estimation of the average winding temperature is achieved by means of a winding resistance measurement system. Considering the variation of the resistance with the temperature, yields a very good result as reported also in Table 3.1.

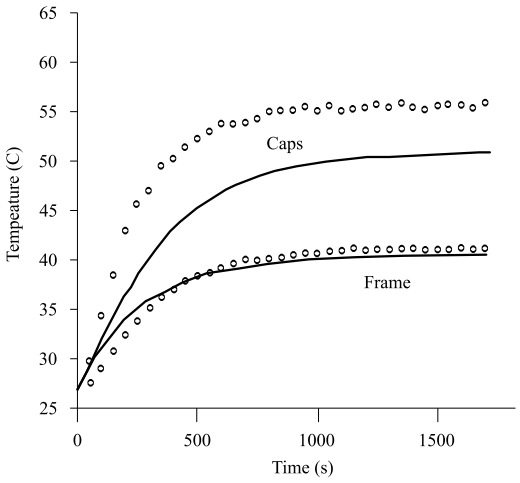

Figure 3.10: Comparison between prediction (solid line) and measurements (circles) for the frame and caps temperature

Furthermore in Table 3.2 the predicted and measured mechanical performance of the motor has been reported for various supply conditions. For all these results the same normalized equivalent circuit has been used, i.e. the FE simulations are carried out only one time which yields a considerable time saving.

After assembling the analytical magnetic and thermal models, many computations can be carried out rapidly.

3.6.2 Intermittent operating cycle

The proposed model also allows the estimation of the motor performance during intermittent operating cycles. The motor is supposed to run in subsequent steady state operation. Then the electrical and thermal models are used to calculate all motor performance.

In Fig. 3.12 the motor operates under nominal load for 5 minutes and under half load for the next 5 minutes, the cycle then repeats. Using the coupled magnetic–thermal model all of the IM performance data can be calculated. In Fig. 3.12 the motor speed and torque are reported and in Fig. 3.13 the losses in the various machine parts are shown. Finally, Fig. 3.14 reports the temperature in the four main parts of the machine.

3.6.3 Whole motor thermal transient

In order to illustrate the proposed strategy for a different motor a four pole servo–ventilated motor is considered in this subsection. For this case, the whole thermal transient of the machine is simulated and measured. First the motor is loaded

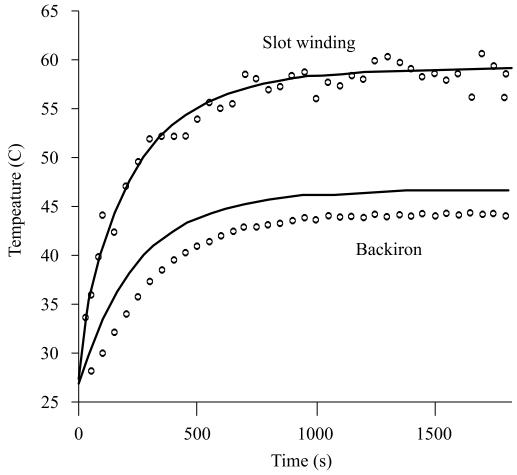

Figure 3.11: Comparison between prediction (solid line) and measurements (circle) for the back iron and slot winding temperature

with nominal power equal to 5.5 kW for one hour and then the motor is stopped. The motor fan is running the entire time. The thermal model parameters vary according to the particular operation of the motor. In particular, when the motor is stopped the convection coefficient for the airgap and the air in the caps are recomputed.

Fig. 3.15 shows the comparison among the predicted and measured temperature in the slot winding and in the end winding of the motor. Predictions are reported with solid lines, while measurements are reported with squares and circles (respectively for the stator slot and the endwinding).

Also in this case the combined strategy (magnetic & thermal) yields good prediction of the entire thermal transient of the motor.

3.7 Conclusions

In this Chapter, a coupled thermal–electromagnetic analysis of the three–phase induction motor has been presented. This analysis is based on the normalized equivalent circuit introduced in Chapter 1 and a lumped–parameter thermal network. The model can be extended to any motor adopting the same lamination and winding distribution including those with different supply conditions. Since the equivalent circuit and thermal network work in conjunction to predict the temperature rise and the IM parameters, the proposed strategy proves to be rapid and accurate at the same time. Taking into account the temperature rise in the various machine parts, allows the machine performance to be computed more accurately, even during severe operating conditions. Experimental tests confirm the accuracy of the model predicted results.

Table 3.2: Comparison of measurements and simulation of motor performance for various supply conditions.

Test type	Torque (Nm)		
	Measured	Simulated	error %
22.0 kW 360 V - 50Hz	74.0	74.7	0.97
22.0 kW 400 V - 50Hz	72.9	73.3	0.52
22.8 kW 440 V - 50Hz	75.3	75.7	0.54
Test type	Current (A)		
	Measured	Simulated	error %
22.0 kW 360 V - 50Hz	49.7	48.3	2.8
22.0 kW 400 V - 50Hz	46.6	45.9	1.5
22.8 kW 440 V - 50Hz	49.7	47.8	3.9
Test type	Electrical power (kW)		
	Measured	Simulated	error %
22.0 kW 360 V - 50Hz	27.6	27.2	1.4
22.0 kW 400 V - 50Hz	26.7	26.5	0.75
22.8 kW 440 V - 50Hz	28.1	28.0	0.36

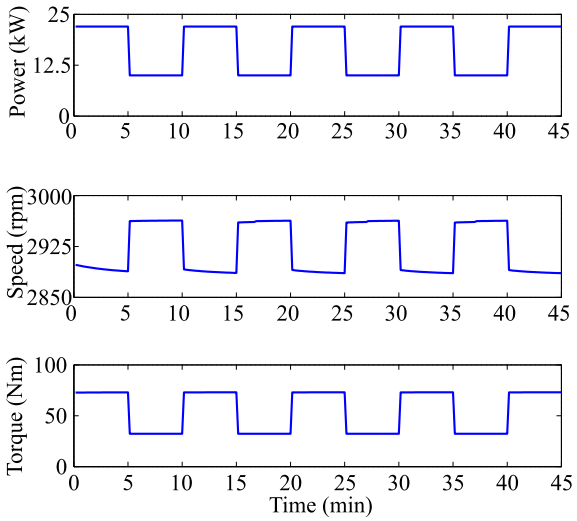

Figure 3.12: Work cycle of the motor in intermittent operating cycle. Mechanical characteristics.

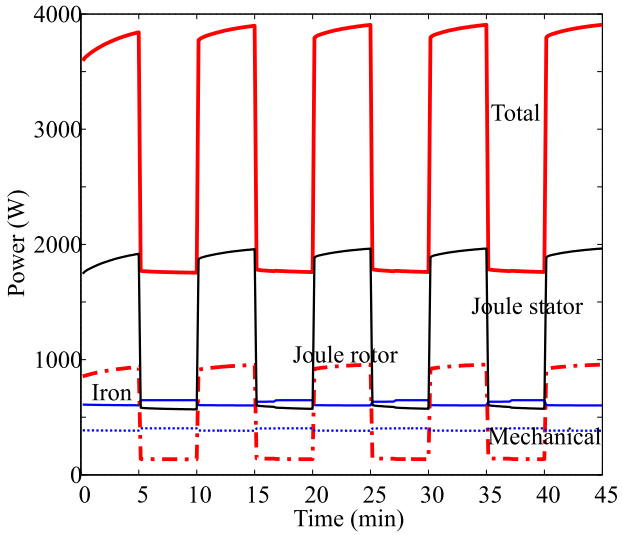

Figure 3.13: Losses in the various machine parts during intermittent operating cycle (simulation results).

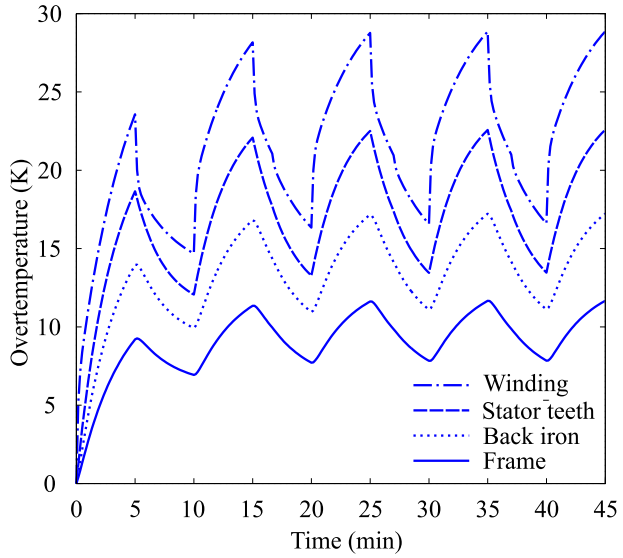

Figure 3.14: Temperature behaviour during intermittent operating cycle (simulation results).

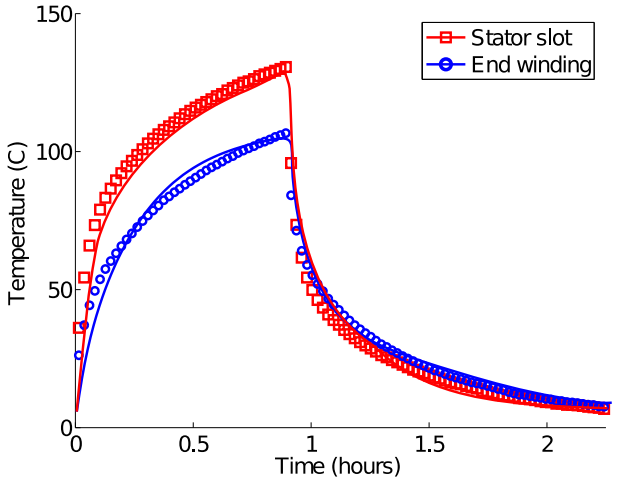

Figure 3.15: Whole thermal transient of the 4–pole motor. Comparison between measurements (circles) and simulations (solid line).

Chapter 4

Finite Element Modeling of Induction Motor for Variable Speed Drives

Abstract– This Chapter deals with a strategy for the IM analysis adopting the rotor flux reference frame. A novelty of the proposed procedure is that only magneto–static field solutions are used for both no–load and load analysis. Both the stator and rotor currents are imposed as field sources. In this way, the IM simulation is similar to that of a synchronous machine, and the computation time is very low.

The proposed strategy is adopted to compute the IM performance, the maximum torque per Ampere trajectory and the torque versus speed characteristic of the drive.

4.1 Introduction

THIS Chapter presents a strategy for the analysis of IM in the rotor flux reference frame. The currents in the simulation are adjusted so as to orient the rotor flux along the d–axis. Only magnetostatic field solutions are used for both no–load and under load analysis. In this way, the IM simulation is similar to that of a synchronous machine and the computation time results reduced taking into account saturation in any operating point of the machine.

The proposed strategy, is appropriate for the prediction of steady state performance of any IM. In particular, it is suitable for variable speed applications, when the field oriented control technique (denoted with the acronym *FOC*) is adopted. In the following, for the proposed strategy the acronym *FOC* is used, although its application is not strictly related to a field oriented controlled machine.

As before a coupled FE–analytical approach is adopted. In particular squirrel cage IMs are considered here while wound rotor IMs are considered in Chapter 6. The main hypothesis of the strategy is to assume a sinewave distribution of the rotor currents. This allows us to impose the rotor currents as field sources according to the *FOC* condition. In this way, the IM simulation is similar to that of a synchronous machine, and the computation time is very low.

The reference frame of the analysis is fixed to the rotor flux, allowing magneto static FE simulations. This kind of simulation has the advantage of a shorter computational time (with respect to magneto–dynamic simulations), as well as better consideration of the iron saturation phenomenon [1, 15, 16]. Moreover the complete torque vs. speed characteristic of the motor is achieved in both constant torque and constant power regions.

At first, the *FOC* equations of the motor are introduced and then the implementation of the model in the FE simulations is described.

4.2 Mathematical model of the IM drive

At first, let us recall the electromagnetic model of the IM. The stator and rotor flux linkages are given by

$$\begin{aligned} \lambda_{sd} &= L_s i_{sd} + L_m i_{rd} \\ \lambda_{sq} &= L_s i_{sq} + L_m i_{rq} \end{aligned} \tag{4.1}$$

and

$$\begin{aligned} \lambda_{rd} &= L_r i_{rd} + L_m i_{sd} \\ \lambda_{rq} &= L_r i_{rq} + L_m i_{sq} \end{aligned} \tag{4.2}$$

where L_s and L_r are the stator and rotor inductances and L_m is the mutual inductance between stator and rotor.

The corresponding voltages are

$$\begin{aligned} v_{sd} &= R_s i_{sd} + \frac{d\lambda_{sd}}{dt} - \omega \lambda_{sq} \\ v_{sq} &= R_s i_{sq} + \frac{d\lambda_{sq}}{dt} + \omega \lambda_{sd} \end{aligned} \tag{4.3}$$

and

$$\begin{aligned} 0 &= R_r i_{rd} + \frac{d\lambda_{rd}}{dt} - (\omega - \omega_{me})\lambda_{rq} \\ 0 &= R_r i_{rq} + \frac{d\lambda_{rq}}{dt} + (\omega - \omega_{me})\lambda_{rd} \end{aligned} \tag{4.4}$$

where R_s and R_r are the stator and rotor resistance, ω is the electrical angular frequency and ω_{me} is the electrical rotor speed. At steady–state, the time derivatives in (4.3) and (4.4) are zero.

4.2.1 Equations of the *FOC* controlled IM

When the *FOC* technique is adopted, the reference frame is chosen so that the d–axis is parallel to the rotor flux λ_r. In other words, only the d–axis component of the rotor flux exists, and the q–axis component is zero i.e. $\lambda_r = \lambda_{rd}$ and $\lambda_{rq} = 0$.

At steady–state the derivatives of the flux linkages are equal to zero. From first equation of (4.4), it results:

$$i_{rd} = 0 \tag{4.5}$$

From the second equation of (4.4), the slip speed can be achieved as

$$\omega_{sl} = (\omega - \omega_{me}) = -\frac{R_r i_{rq}}{\lambda_{rd}} \tag{4.6}$$

From (4.1), adopting (4.5) and (4.9), the stator flux linkages are

$$\begin{aligned} \lambda_{sd} &= L_s i_{sd} \\ \lambda_{sq} &= \left(L_s - \frac{L_m^2}{L_r}\right) i_{sq} \end{aligned} \tag{4.7}$$

where the inductance within the parenthesis is the stator dynamic inductance, often labeled as L_t.

From (4.2), adopting (4.5), the rotor flux linkages are

$$\begin{aligned} \lambda_r &= L_m i_{sd} \\ 0 &= L_r i_{rq} + L_m i_{sq} \end{aligned} \tag{4.8}$$

The first equation highlights that the rotor flux linkage is only due to the d–axis stator current. Then the second equation of (4.8) links the q–axis stator and rotor currents:

$$i_{rq} = -\frac{L_m}{L_r} i_{sq} \tag{4.9}$$

4.3 Analysis procedure

The procedure is described referring to a 2–pole 300–W squirrel cage IM. A sketch of the motor geometry is shown in Fig. 4.2(a) where the flux lines at no load are reported. The same motor is considered in Chapter 5 where the analysis procedure is validated by means of experimental test. The main motor data are reported in Table 5.1.

4.3.1 Winding

The three–phase winding of the IM is considered using the classical d–q transformation. Therefore, the transformation $dq \longrightarrow abc$ is used to compute the actual value of the stator currents.

As far as the rotor winding is concerned, it is rearranged using the d–q transformation with a sinewave conductor distribution. In this way, the rotor current is supposed to be sinusoidally distributed along the airgap.

The winding matrix of the actual motor winding is described in Table 4.1. The numbers in the table express the slot fill of each phase (a, b and c).

Table 4.1: Winding distribution of the actual motor winding

	slot number											
	1	2	3	4	5	6	7	8	9	10	11	12
a	-1	-0.5	-0.43	0	0	0	0	0	0	0.43	0.5	1
b	0	0	0	0	0	0.43	0.5	1	1	0.5	0.43	0
c	0	0.43	0.5	1	1	0.5	0.43	0	0	0	0	0
	slot number											
	13	14	15	16	17	18	19	20	21	22	23	24
a	1	0.5	0.43	0	0	0	0	0	0	-0.43	-0.5	-1
b	0	0	0	0	0	-0.43	-0.5	-1	-1	-0.5	-0.43	0
c	0	-0.43	-0.5	-1	-1	-0.5	-0.43	0	0	0	0	0

The winding factor for the three phase stator winding is $k_{w,s} = 0.9299$. During each simulation, the stator currents are imposed so as to obtain the prefixed d or q–axis flux.

As far as the rotor is concerned, the number of rotor turns N_r is rearranged in order to make it equivalent to the stator winding, that is, the following relationship is used:

$$k_{w,r} \cdot N_r = \frac{3}{2} \cdot k_{w,s} \cdot N_s \tag{4.10}$$

The winding matrix for the transformed rotor winding is reported in Table 4.2.

4.3.2 Stator currents at no–load

At no–load, only the d–axis stator current is imposed in the stator, i.e. $i_{sd} \neq 0$, $i_{sq} = 0$, $i_{rd} = 0$ and $i_{rq} = 0$. Fig. 4.1(a) shows the current reference. The current i_{sd} produces the flux along the d–axis. It is linked by the stator winding yielding λ_{sd}, and by the rotor winding yielding λ_{rd}. Such a flux is the main flux of the machine in the most of operating conditions.

Table 4.2: Winding distribution of the rotor $d-q$ winding

	slot number						
	1	2	3	4	5	6	7
d	0.111	0.330	0.532	0.707	0.846	0.943	0.993
q	-0.993	-0.943	-0.846	-0.707	-0.532	-0.330	-0.111
	slot number						
	8	9	10	11	12	13	14
d	0.993	0.943	0.846	0.707	0.532	0.330	0.111
q	0.111	0.330	0.532	0.707	0.846	0.943	0.993
	slot number						
	15	16	17	18	19	20	21
d	-0.111	-0.330	-0.532	-0.707	-0.846	-0.943	-0.993
q	0.993	0.943	0.846	0.707	0.532	0.330	0.111
	slot number						
	22	23	24	25	26	27	28
d	-0.993	-0.943	-0.846	-0.707	-0.532	-0.330	-0.111
q	-0.111	-0.330	-0.532	-0.707	-0.846	-0.943	-0.993

Once computed the flux linkages λ_s and λ_r can be used to compute the inductance L_s from (4.7) and L_m from (4.8)

Fig. 4.2(a) reports the flux lines in the no load analysis. As expected, the flux lines do not cross the d–axis, i.e. flux lines are only along the d–axis.

The no load simulation has been carried out for various i_{sd}. The 3D effects are considered adding the 3D parameters, and the phase–to–phase voltage versus current characteristic is computed and compared with measurements. In Fig. 4.2(b), predictions are reported with solid lines and measurements with circles.

4.3.3 Stator and rotor currents under load

In the operating condition under load, both the d–axis current i_{sd} and q–axis current i_{sq} are forced in the stator winding. Then, a corresponding rotor current i_{rq} has to be assigned in the rotor in such a way that the relationship $\lambda_{rq} = 0$ is satisfied, as in (4.8), that is, the FOCcondition is valid.

In Fig. 4.1(b) the current references are shown and the FOCcondition $\lambda_{rq} = 0$ is also reported.

A preliminary estimation of the rotor current i_{rq} is achieved by means of (4.9)

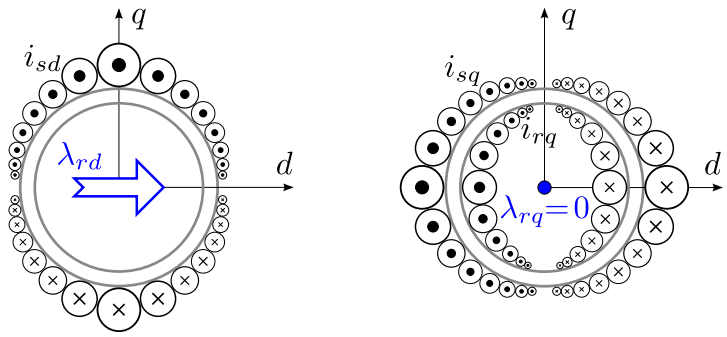

(a) no–load simulation (b) under load simulation

Figure 4.1: Convention for positive current assumed in the simulations. Sinusoidal distributed rotor winding is considered.

assuming $L_r \simeq L_m^2/L_s$, that is, a perfect coupling between stator and rotor. [1]

Since both stator and rotor currents are imposed as the field source, only magnetostatic FE analysis is necessary. The actual field solution is achieved iteratively. At each step the rotor flux linkage is computed from the field solution and, if the q–axis component is different from zero, the q–axis rotor current i_{rq} has to be modified so as to reduce λ_{rq} to zero. Since the variations are carried out along the q–axis, orthogonal to the main flux direction, the flux linkage variation is proportional to the current variation. Therefore, only a few steps, generally three, are sufficient to determine the proper rotor currents.

The convergence process is sketched in Fig. 4.3, where the linearity of the iron in the q–axis direction is shown.

The motor torque can be computed from the Maxwell's stress tensor from the field solution. Alternatively, the torque can be computed as [56]:

$$\tau_m = \frac{3}{2} p \lambda_{rd} i_{rq} \tag{4.11}$$

The slip speed, in electrical radians per second, is achieved from (4.6). Multiplying both numerator and denominator by $\frac{3}{2} i_{rq}$, such a speed becomes

$$\omega_{sl} = \frac{P_{Jr}}{\frac{3}{2}\lambda_{rd} i_{rq}} = p \, \frac{P_{Jr}}{\tau_m} \tag{4.12}$$

where P_{Jr} is the Joule loss in the rotor cage that is easily computed from the field solution.

[1] For two magnetic circuits the coupling factor is defined as $k = \dfrac{L_m}{\sqrt{L_s \, L_r}}$. When they are perfectly coupled it is $k = 1$.

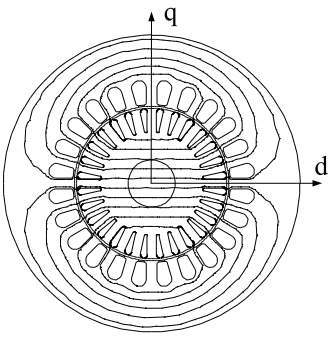

(a) Flux lines $i_{sd} = 1.5\ A$

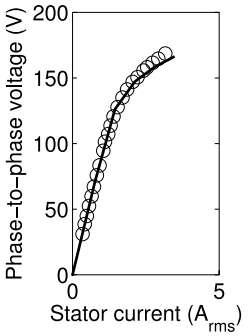

(b) Phase to phase voltage. Predictions and tests comparison.

Figure 4.2: No load simulations, only d–axis current.

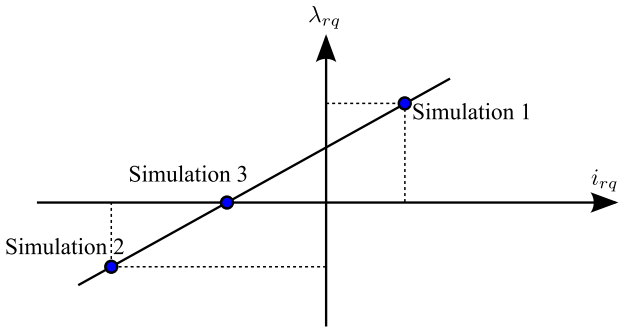

Figure 4.3: The convergence process during the load simulations.

Fig. 4.4(a) shows the flux lines under load operating condition with $i_{sd} = 1.5$ A, $i_{sq} = 1.5$ A and $\lambda_{rq} \neq 0$. In this case, the FOCcondition is not satisfied and this is evident since the flux lines are also in the q–axis direction.

On the contrary, Fig. 4.4(b) shows the flux lines under load operating condition with $i_{sd} = 1.5$ A and $\lambda_{rq} = 0$. Now the FOCcondition is satisfied and in the rotor the flux line are only in the d–axis direction.

In Fig. 4.5 the stator and rotor flux linkages versus q–axis stator current curves for $i_{sd} = 1.5$ A are shown. It could be observed that the FOCcondition $\lambda_{rq} = 0$ is kept for each q–axis stator current. The d–axis flux linkages satisfy the relationship:[2]

$$\frac{\lambda_{rd}}{\lambda_{sd}} = \frac{L_m}{L_s} \tag{4.13}$$

[2]This result making the ratio between the first equations of 4.8 and 4.7.

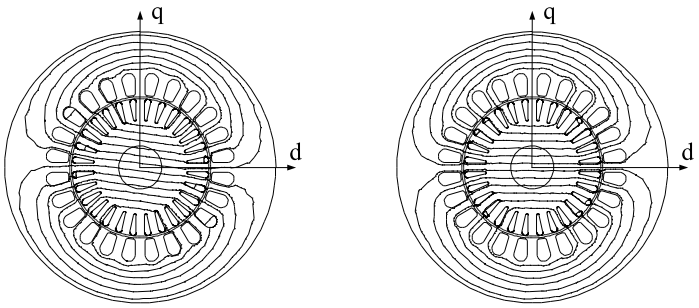

(a) $\lambda_{rq} \neq 0$ (b) $\lambda_{rq} = 0$

Figure 4.4: Under load simulations $i_{sd} = 1.5$ A.

Since the motor is not saturated, they remain almost constant increasing the q–axis current. From (4.7) the q–axis stator flux linkage λ_{sq} is related to the q–axis stator current by the stator dynamic inductance L_t. Since L_t is quite constant, λ_{sq} increases linearly with i_{sq}. Let us note that λ_{rd} results higher than λ_{sd} since the rotor winding is characterized by a higher number of turns. It can be reported to the stator using the turns ratio which, from (4.10), equals 3/2.

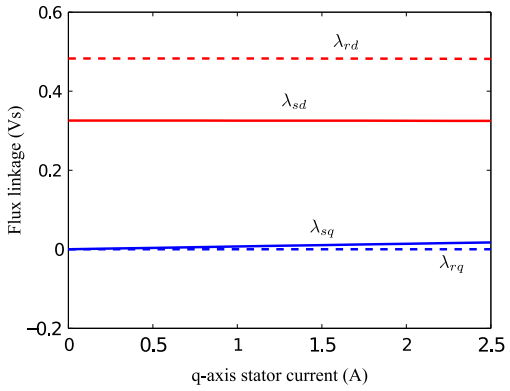

Figure 4.5: Stator and rotor flux linkages versus q–axis current for $i_{sd} = 1.5$ A

In Fig. 4.6 the torque versus q–axis stator current is shown for $i_{sd} = 1.5$ A. Two computations are compared: the torque computed by Maxwell's stress tensor (solid line) and the torque computed by (4.11). Very good agreement can be observed.

Then, a rotation of the stator current spatial vector is simulated. The stator current amplitude is fixed at $i_s = 3$ A and its angle ϑ_i has been varied from 0 to 90 electrical degrees.

Fig. 4.7 shows the stator and rotor flux linkages versus stator current angle.

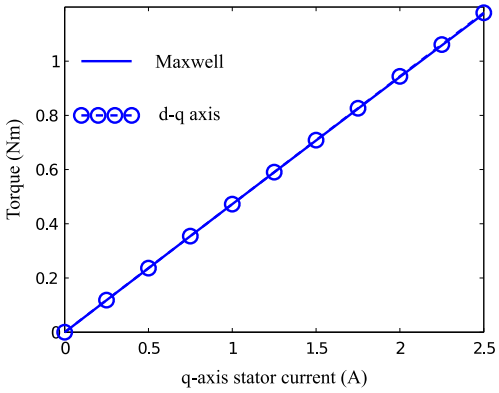

Figure 4.6: Torque versus q–axis stator current for $i_{sd} = 1.5$ A

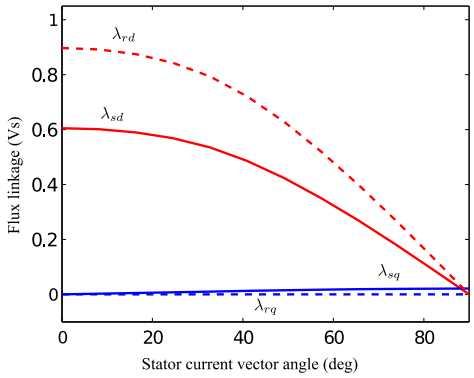

Figure 4.7: Stator and rotor flux linkages versus stator current angle for $i_s = 3$ A

The no load condition corresponds to $\alpha_{is} = 0$. The d–axis flux linkages λ_{sd} and λ_{rd} decrease as the current vector angle increases. With linear iron these curves are cosine, a similar behaviour is visible in Fig. 4.7. In this case, the q–axis stator flux linkage λ_{sq} increases as a sine, since the q–axis stator current i_{sq} increases sinusoidally and L_t is quite constant. Anyway the q–axis flux linkages are always smaller than the d–axis flux linkages.

4.4 The torque versus speed characteristic

The simulations described in the above section allow for a rapid and precise computation of the IM performance at various operating points.

For example it is possible to predict the whole torque versus speed charac-

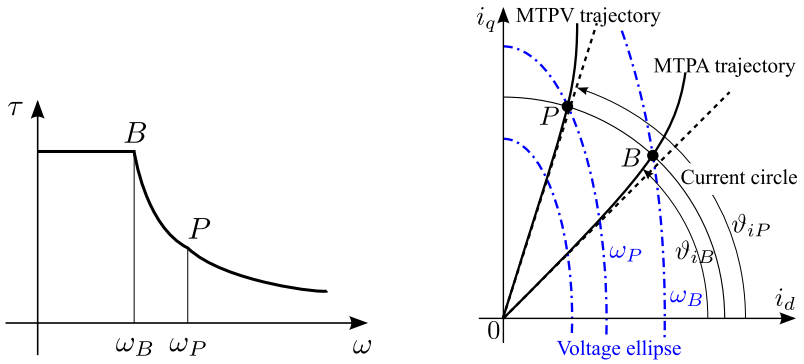

Figure 4.8: Various IM operating point: (a) torque versus speed characteristic; (b) polar diagram. Dashed line refers to the trajectories in linear conditions; with solid lines the saturation effect is shown.

teristic of the motor. A qualitative behaviour of such characteristics is shown in Fig. 4.8(a). In Fig. 4.8(b) the polar diagram of the IM is reported [57].

There are three main operating regions for the drive which are described in the following subsections.

4.4.1 MTPA

The base point B is a point on the maximum torque per Ampere (MTPA) trajectory. Up to this point the motor torque is constant. In linear conditions, the current angle for the MTPA trajectory is $\vartheta_{iB} = \pi/4$. Due to the effects of iron saturation the current angle for MTPA increases.

The MTPA trajectory deviation due to the saturation effect is shown in Fig. 4.8(b) using a solid line.

Fig. 4.9 reports the torque versus stator current angle for various stator currents. From Fig. 4.9, the saturation effects on the MTPA is visible. At low current, for example with $i_s = 1$ A, the machine is unsaturated and the MTPA angle is equal to $\pi/4$. In this case the curve in Fig. 4.9 is a sine curve and it is symmetric respect to the angle $\pi/4$.

As the current increases, the iron saturates and so the MTPA angle increases. This is the case for the curve $i_s = 6$ A in Fig. 4.9. Due to the saturation, the curve is deformed and the MTPA angle increases.

Let us remark that the proposed strategy allows one to consider carefully the saturation effects at any operating point.

As above, the torque computed by Maxwell's stress tensor (solid line) is compared with the torque compute by (4.11) (circles). Very good agreement can be observed also in this case.

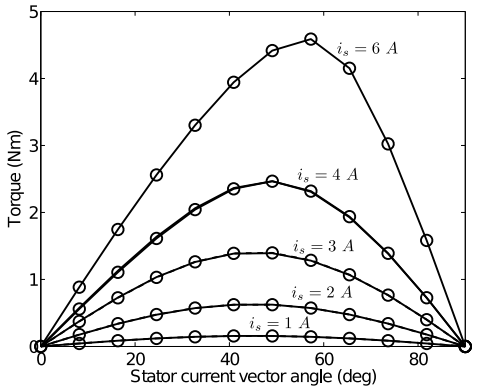

Figure 4.9: Torque versus stator current angle for various i_s

4.4.2 CPSR

Above the base point B, the current amplitude is maintained constant while the current vector angle ϑ_i is increased. The motor torque and flux become smaller which allows the motor to run at a higher speed. The operating region between points B and P is often denominated as the constant power speed range (CPSR).

4.4.3 MTPV

The point P is located at the intersection among the current circle and the maximum torque per voltage (MTPV) trajectory. The point P is identified by this condition:

$$\tan \vartheta_{iP} = \frac{\lambda_{sd}\ i_{sq}}{\lambda_{sq}\ i_{sd}} \tag{4.14}$$

Above the point P, the motor is driven on the MTPV trajectory up to the maximum speed. In this region the motor power decreases.

For each motor simulation, the condition (4.14) is checked in order to recognize when the point P is reached in the path $B \rightarrow P$ (see Fig. 4.8). Along the path $P \rightarrow O$ the condition (4.14) is used for checking that the motor operating point remains along the MTPV trajectory.

Also in this case, thanks to the particular analysis strategy, the saturation effect on machine performance is carefully taken into account for any motor operating point.

In Fig. 4.10 the simulated torque versus speed characteristic of the motor is reported. The point B and P are highlighted on the torque characteristic. Let us remark that the whole characteristic has been simulated only with magnetostatic simulations.

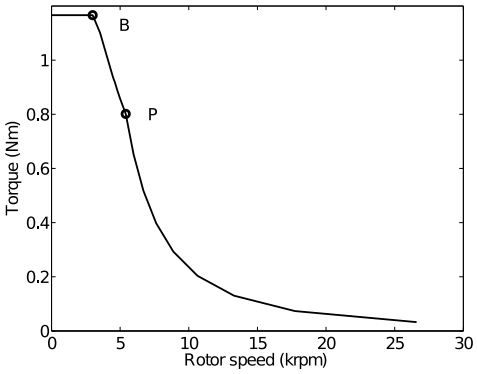

Figure 4.10: Simulated mechanical characteristic of the motor. The point B and P computed during the simulations are highlighted.

4.5 The equivalent circuit of an IM operating in *FOC* condition

In the previous Sections, the proposed strategy is used to compute the IM performance. It can be used also to compute the equivalent circuit of an IM operating in *FOC* conditions. In [58] different topologies of IM equivalent circuits have been described with their peculiarities. In particular, when *FOC* technique is adopted, the "inverse Γ" model is particularly useful. In fact in this case the torque current component and the flux current component are in quadrature.

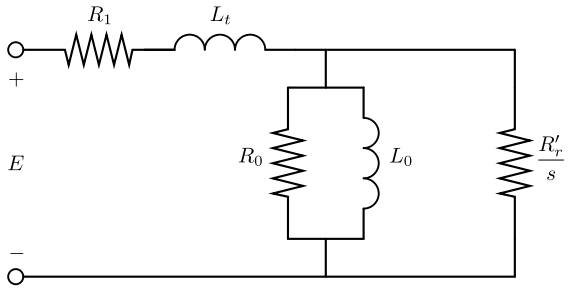

Figure 4.11: The "inverse Γ" equivalent circuit of the IM

Fig. 4.11 shows the "inverse Γ" equivalent circuit of the IM. Its parameters are computed from the FE simulations as:

$$\begin{aligned} L_t &= L_s - \frac{L_m^2}{L_r} \\ Ł_0 &= \frac{L_m^2}{L_r} \end{aligned} \tag{4.15}$$

The rotor resistance R_r is computed from the rotor Joule losses; the iron loss resistance R_0 and the others 3D parameters are computed as described in Sec. 1.4.3.

A comparison of IM performance computed by the "inverse Γ" equivalent circuit and the circuit described in Chapter 1 will be presented in Chapter 5.

4.6 Conclusions

In this Chapter a new procedure for achieving the steady state performance of IMs has been presented. The strategy is particularly suitable for variable speed IMs, but it can be use also for other applications. Both the stator and rotor currents are imposed as field source and are adjusted so as to obtain a rotor flux along the d–axis. In this way, the IM simulation is similar to that of a synchronous machine, the computation time is reduced and the saturation effects are carefully taken into account for each machine operating point.

Adopting this analysis strategy, it is possible to achieve a rapid and precise prediction of the whole torque versus speed curve of the induction motor.

Chapter 5

Application examples of the *FOC* analysis

Abstract– In this Chapter, the analysis procedure presented in Chapter 4 is adopted for the computation of an IM for washing machine applications. Various operating conditions, at low and high frequency, are considered. The computation is compared with results obtained from the analysis described in Chapter 1 and from measurements.

5.1 Application description

THE motor considered in this Chapter is designed for a washing machine. In this application, two main operating points are required:

- *washing*
  low speed and high torque for moving the water inside the basket.
  The motor is supplied at 30 V, 8.33 Hz (synchronous speed 500 rpm)
- *spin dryer*
  high speed and low torque for drying the linen.
  The motor is supplied at 195 V, 300 Hz (synchronous speed 18000 rpm)

The motor considered here is the same as Chapter 4. A sketch of the motor geometry is shown in Fig. 4.2(a) The main data of the motor are reported in Table 5.1.

Table 5.1: Main geometrical data of the motor

Poles	$2p$	2
Stator slots	Q_s	24
Rotor slots	Q_r	32
Stack length	L_{stk}	55 mm
Stator inner diameter	D	55 mm
Airgap	g	0.33 mm

In the next Sections, the motor performance in the two operating conditions are computed with the "inverse Γ" equivalent circuit computed with the strategy described in Chapter 4 (this model is labeled *FOC* in the following table). For the sake of comparison, the IM is computed along with the equivalent circuit described in Chapter 1 (label *RA* in the table) and the results are validated with experimental test.

5.2 No load computation

In this section the no load performance of the IM is considered. The frequency is fixed at 50 Hz and various voltages are considered. Table 5.2 reports the comparison between the two equivalent circuits. Experimental tests are also reported. Good agreement can be noted between prediction and measurement. This is expected because the two equivalent circuits at no–load are very similar.

5.3 Washing computation

In this section the performance of the IM during washing is considered. Various frequencies about 50 Hz are considered. The voltage is varied in order to keep constant the ratio V/f. Table 5.3 reports the comparison between the two equivalent circuit computations. Experimental tests are also reported.

Table 5.2: No–load computation comparison

		Test	*RA*	*FOC*	Test	*RA*	*FOC*
V	(V)	75.8	75.8	75.8	107	107	107
Io	(A)	0.84	0.82	0.9	1.23	1.18	1.3
Po	(W)	9.1	9.6	8	15.3	14.7	16
V	(V)	120	120	120	135	135	135
Io	(A)	1.4	1.34	1.5	1.7	1.6	1.77
Po	(W)	19.4	20	20	26.4	25	25

Good agreement among the values reported in the table can be noted. This is particularly true for the mechanical computation T and P_m. For the electrical quantities the discrepancy is greater, with an average discrepancy about 10%

This is explainable considering the simplified model adopted for the losses of the IM. In order to increase the accuracy of the prediction, the model can be improved as suggested in, [19, 20, 59–62]. Moreover the thermal behaviour of the machine has not been considered in the predictions meaning the machine parameters have not been affected by temperature.

5.4 Spin computation

In this section, the performance of the IM during spin operation is computed. Various frequencies slightly lower than 300 Hz are considered. The voltage is adapted so as to keep quite constant the ratio V/f. Table 5.4 reports the comparison between the two equivalent circuits computation. Experimental tests are also reported.

Also in this case, good agreement among the values reported in the table can be noted. As above, the agreement is greater for the mechanical computation T and P_m. The same statement regarding the improvement of the model can also be made in this case.

5.5 Comparison between the two models

In this section a comparison between the models presented in Chapter 1 (model *RA*) and Chapter 4 (model *FOC*) is presented.

The first consideration is regarding the type of FE simulation that is required. For the computation of the *RA* model a series of magnetostatic simulations for the "no–load" analysis are required. Then a series of magnetodynamic simulations are carried out in order to compute the IM parameter variation with the frequency. For the computation of the *FOC* model only magnetostatic simulations are required. This allows a reduction in the computation time.

Table 5.3: Washing computation comparison

		Test	*RA*	*FOC*	Test	*RA*	*FOC*
V	(V)	42	42	42	48	48	48
f	(Hz)	9	9	9	12	12	12
s	(%)	46	46	46	30	30	30
I	(A)	3.8	3.7	3.4	3.5	3.3	3.1
P_e	(W)	270	250	230	276	240	220
P_0	(W)	7.6	7.2	7.8	7.4	8.6	9
T	(Nm)	2.2	2.2	2.2	2	1.8	1.8
P_m	(W)	67	66	67	105	95	95
V	(V)	51	51	51	52	52	52
f	(Hz)	12.3	12.3	12.3	11.5	11.5	11.5
s	(%)	33.2	33.2	33.2	30.3	30.3	30.3
I	(A)	3.8	3.6	3.3	3.8	3.9	3.4
P_e	(W)	319	280	260	311	301	261
P_0	(W)	10.2	9.6	10	10.5	10.3	11
T	(Nm)	2.2	2.1	2.1	2.2	2.1	2.2
P_m	(W)	113	107	107	111	106	110
V	(V)	54.6	54.6	54.6	60	60	60
f	(HZ)	12.6	12.6	12.6	13.1	13.1	13.1
s	(%)	40	40	40	30	30	30
I	(A)	4.3	4.1	3.8	4.2	4.3	3.7
P_e	(W)	390	360	336	400	390	348
P_0	(W)	13	11	12	15	13	14
T	(Nm)	2.55	2.54	2.6	2.6	2.5	2.6
P_m	(W)	122	120	123	151	142	148

Moreover, with closed rotor slots particular attention has to be payed to the magnetodynamic simulation in order to avoid wrong results. In fact a closed slot in a linear FE simulation is similar to a magnetic short circuit for the flux line (for example for the lines produced by the rotor currents). This makes no sense physically, because thanks to the saturation of the iron bridge the behaviour is very different [24, 25, 63, 64]. This yields a wrong estimation of the equivalent circuit parameters. In order to avoid this, the saturation of the iron bridge has to be carefully taken into account introducing an equivalent air bridge above each rotor bar [26]. On the other hand, the *FOC* model allows the actual geometry to be considered in the FE simulation. Thanks to the use of magnetostatic simulations the saturation is carefully taken into account also in the iron bridge of the rotor slots.

Table 5.4: Spin computation comparison

		Test	*RA*	*FOC*	Test	*RA*	*FOC*
V	(V)	198	198	198	213	213	213
f	(Hz)	288.7	288.7	288.7	288	288	288
s	(%)	6.32	6.32	6.32	6	6	6
I	(A)	3.2	2.7	2.5	3.1	2.8	2.6
P_e	(W)	941	830	814	1030	930	902
P_0	(W)	97	80	84	120	90	95
T	(Nm)	0.4	0.4	0.4	0.45	0.42	0.45
P_m	(W)	685	624	690	760	710	765
V	(V)	218	218	218	219	219	219
f	(Hz)	275	275	275	286	286	286
s	(%)	1.7	1.7	1.7	1	1	1
I	(A)	1.3	1.2	1.1	0.8	0.74	0.7
P_e	(W)	430	407	360	244	224	195
P_0	(W)	62	50	56	57	46	44
T	(Nm)	0.2	0.19	0.18	0.1	0.1	0.1
P_m	(W)	340	320	320	179	167	161
V	(V)	220	220	220	226	226	226
f	(Hz)	272	272	272	272	272	272
s	(%)	1	1	1	0.86	0.86	0.86
I	(A)	0.78	0.75	0.73	0.85	0.77	0.8
P_e	(W)	220	215	200	252	240	210
P_0	(W)	40	46	44	43	49	46
T	(Nm)	0.12	0.11	0.1	0.11	0.1	0.1
P_m	(W)	157	167	160	168	176	170

It is also interesting to consider the current distribution within the rotor slots in the two models. The *FOC* model is based on the hypothesis that the rotor currents are sinusoidally distributed along the rotor periphery. In the *RA* model the rotor current distribution is computed from the field solution, that is in the magnetodynamic simulation. In this case each rotor slot current is assumed sinusoidally in time, but the distribution along the rotor periphery in the various slots are computed by the field solution. These assumptions are verified by comparing the rotor current distribution achieved with *RA* and *FOC* strategies, as shown in Fig. 5.1. Fig. 5.2, also shows the harmonic content of the rotor current distributions in Fig. 5.1. A higher discrepancy between the rotor current harmonic content occurs when the assumption of a sine–wave rotor current distribution is not verified. This is the case with an IM with a low number of slot per pole and per

phase. In this case the prediction of the IM performance with the two procedures yields different results.

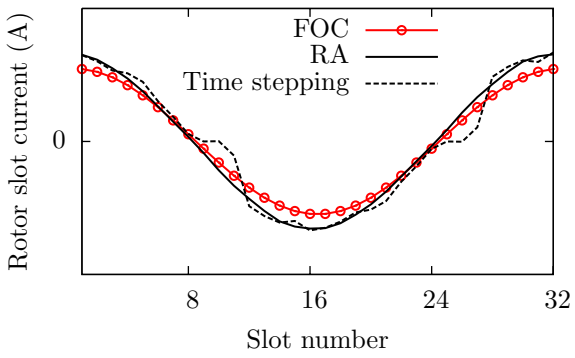

Figure 5.1: Comparison of the current distributions with three analysis strategies;
FOC: strategy described in Chapter 4;
RA: strategy described in Chapter 1
Time stepping: time transient solution.

For the sake of comparison, the rotor current distribution is computed with a time transient solver [65]. The rotor speed is fixed at 0 rpm. In this way the rotor is stationary like in the other simulations, that is the influence of the movement does not affect the simulation. In the stator windings the same current and frequency of the magnetodynamic simulation are imposed. The reported results refer to the steady state operation after the starting transient. Each rotor bar current is considered at the same time instant and the current distribution along the rotor periphery is reported in Fig. 5.1. The harmonic contents is reported in Fig. 5.2.

As can be noted, the harmonic contents of the time stepping simulation is richer than the others. In this case the rotor currents are not sinusoidal in time, and the harmonic content of the rotor current distribution along the rotor periphery depends on the time instant considered.

To illustrate this, Fig. 5.3 shows a rotor bar current versus time computed from the time transient solution. Fig. 5.4 shows the time harmonic content of the curve in Fig. 5.3

5.6 Conclusions

In this Chapter, the analysis procedure presented in Chapter4 has been adopted to compute an IM for washing machines. Various operating conditions, at low and high frequency, have been considered. The experimental tests reported, confirms that the model is able to predict the machine performance with a good accuracy. The obtained results have been compared with predictions achieved with

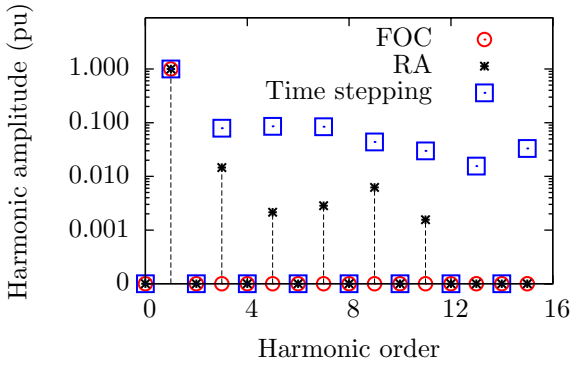

Figure 5.2: Harmonic components of the rotor currents in the two models.

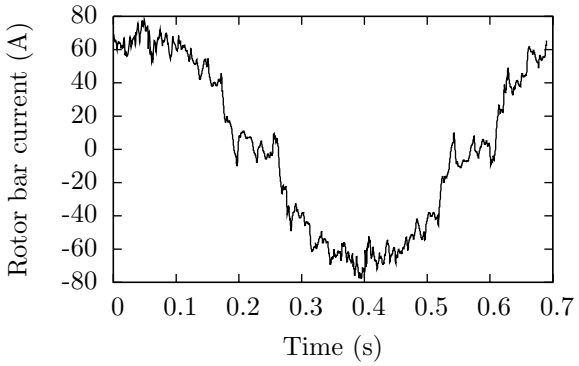

Figure 5.3: Rotor bar current in an electrical period.

the model of Chapter 1, and the assumptions of the two models have been commented pointing out the different current distributions within the rotor slots in the two case. Finally, for the sake of comparison, a time transient simulation has been carried out and the rotor currents distribution has been compared with that of the proposed strategies.

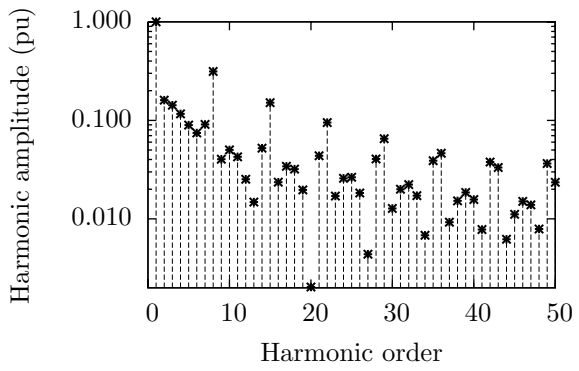

Figure 5.4: Time harmonic contents of the rotor bar current.

Chapter 6

Design Feasibility of a Fractional–Slot Doubly Fed Induction Machine for Direct Drive Applications

Abstract– In this Chapter the possibility to design a fractional–slot doubly fed IM for a direct–drive application is investigated. This Chapter shows that in a doubly fed induction machine, a proper choice of the number of stator and rotor slots minimizes the interaction between stator and rotor MMF harmonics, limiting losses and torque ripple. The design strategy of the doubly fed induction machine is explained and the results are commented, highlighting advantages and drawbacks of the proposed solutions.

6.1 Introduction

THE aim of this Chapter is to investigate the feasibility of designing a doubly fed induction machine for direct–drive applications, requiring high power at low speed. In addition, this Chapter considers a fractional–slot solution that is never used for IM, showing that it is feasible when the IM is doubly fed. There are many applications in which such a solution could be applied, for instance; mills, presses, lift systems, propulsion systems and, for generation in wind power systems. The considerations reported in this Chapter are general and can be referred to any direct–drive application.

The advantages and the drawbacks of the solution analyzed hereafter can be applied to a wide variety of similar applications. For instance let us focus on a wind power generator, there are two main solutions:

- The use of a permanent magnet (PM) machine, typically with surface mounted PMs, directly coupled with the turbine (see Fig. 6.1(a)). The machine has to exhibit a high torque, thus it is characterized by big dimensions [66, 67].
- The use of a induction machine coupled to the turbine by means of a gearbox (see Fig. 6.1(b)). The IM speed is higher than the turbine speed, so that, for a given power, the IM has to exhibit a moderate torque. Therefore, its size is reduced [68–73].

In recent years direct–coupled PM machines have been increasing in popularity. The main advantage of this solution is the absence of a gearbox, with a consequent increase in efficiency and reliability of the whole system. The machine rotates at the same speed as the turbine, that is, at low speed. It is characterized by a high number of poles that are achieved by arranging properly the PMs along the surface of the rotor. The design of the machine is not difficult, and different numbers of poles can be easily accommodated. The adoption of PMs has the further advantage that there is no magnetizing current, with a consequent increase of the machine efficiency.

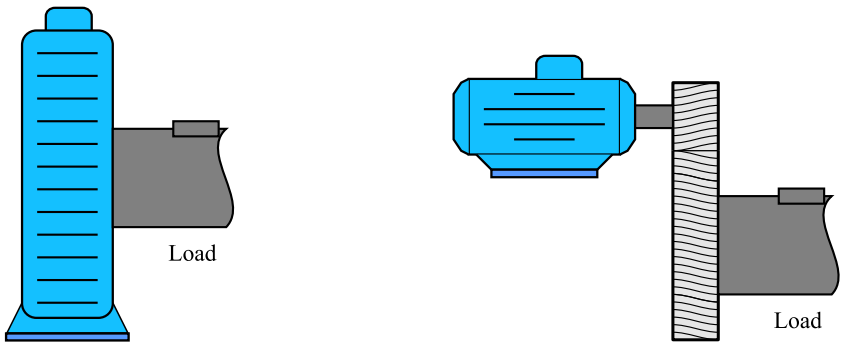

(a) Direct coupled machine

(b) Machine coupled to the load with a gearbox

Figure 6.1: Different types of machine coupling

As far as the stator, the recent general tendency is to adopt fractional–slot winding stators, that is, stators with a non–integral number of slots Q per phase m and per poles $2p$. Such solutions allow one to reduce the periodicity between slots and poles, thereby minimizing the torque ripple of the machine. In addition, the solutions with concentrated coils, i.e. wound around a single tooth, facilitate the winding manufacture and minimize the end windings, that is, the Joule losses in the end connections.

On the other hand, the PM becomes a key component of the machine. They have to be protected against corrosion, the operating temperature has to be monitored and the demagnetizing current has to be adequately limited. Special designs can be adopted in order to avoid the irreversible demagnetization of the PM material, even in the event of a short–circuit condition. Finally, in the building of large machines special care is required when mounting the PM rotor inside the stator.

The IM is normally combined with a gearbox, in order to increase the speed and to reduce the number of poles. The stator winding can be connected directly to the grid. For the regulation of the power flow, a wound rotor is adopted and the rotor currents are controlled by means of a bidirectional power converter. The IM can be operated as a generator at both sub– and super–synchronous speed. The speed range depends on the converter ratings: limiting the slip e.g. to 10%, the Volt-Amps rating of the power converter reduces to 10% of the IM nominal power, with an evident cost saving. A direct–drive IM is never adopted. It appears to be disadvantageous in comparison with the PM machine, mainly due to the required high number of poles. Contrary to the PM machine, the IM requires a magnetizing current and, furthermore, this current increases with the number of poles. In addition, since in low speed applications the ratio between the slots and the poles reduces, the adoption of a fractional–slot winding becomes inevitable. However, the adoption of an IM with fractional–slot winding yields high harmonic contents of MMF space–harmonics in the air–gap. The interaction between the stator and rotor MMF harmonics cause parasitic losses, a decrease of average torque and torque ripple.

The aim of this Chapter is to demonstrate that some solutions exist, that can overcome the drawbacks described above. This Chapter will investigate the possibility of designing a doubly fed IM, characterized by fractional–slot windings, suitable for operating in direct drive applications. Although the expected performance of such a machine is lower than the PM machine performance, the presented study paves the way for future analysis and development.

6.2 Choice of the stator and rotor windings

The direct–drive doubly fed IM is characterized by two three–phase windings. In this section, the criteria to design a suitable fractional–slot winding are given.

Let us assume that the speed of the IM is fixed by the application as in a wind–power generator, the angular speed is fixed by mechanical considerations of the maximum speed of the blade tips. Additionally, if the stator winding is directly

connected to the grid, the operating frequency is also fixed. As a result, the number of poles is computed according to the rated speed and operating frequency.

At this point, the two fractional–slot windings have to be chosen so as to exhibit the minimum interaction among their space–harmonics. This means that the order of the MMF harmonics of the stator windings have to be as different as possible from the order of the MMF harmonics of the rotor winding.

6.2.1 Computation of the MMF space–harmonics

The computation of the order of the MMF space–harmonics of a given three–phase winding is carried out on the basis of the theory of the star of slot [8,37,74]. Some details are given hereafter.

Let us refer to a three–phase machine with a fixed number of slots Q and number of poles $2p$. The star of slots is formed by Q phasors that are numbered according to the number of the corresponding slot. The machine periodicity is given by the greatest common divisor ($G.C.D.$) between Q and p, that is, $t = G.C.D.\{Q,p\}$ [74]. Then, the star of slots is characterized by

- Q/t spokes,
- each spoke containing t phasors.

When Q/t is even, there are no harmonics of even order in the winding distribution and therefore in the MMF distribution. They are all harmonics of odd order, multiplied by machine periodicity t, not multiples of three. On the contrary, when Q/t is odd, there are harmonics of both even and odd order, always multiplied by machine periodicity t, not multiples of three.

The winding factor is achieved as the product between the distribution factor and the pitch factor, i.e. $k_w = k_d k_p$. The distribution factor k_d is the ratio between the geometrical and the arithmetic sum of the phasors of the same phase. The computation can be repeated for each harmonic order ν. The pitch factor k_p is independent of the star of slots and is computed according to the coil throw y_q. This is approximated by $y_q \approx Q/(2p)$ and it is considered here to be unity, assuming fractional–slot windings with non–overlapped coils.

6.2.2 Interaction between the MMF space–harmonics of the two windings

Both the stator and rotor windings can be conveniently described by the distribution of its conductor density along the air–gap adopting the Fourier series expansion. Then, when a winding carries a current, a linear current density is defined, which is the resultant for all the phases. At steady state, it results in

$$K(\theta) = \sum_{\nu} \hat{K}_\nu \sin(\nu p \vartheta - \omega t) \tag{6.1}$$

and it is commonly called electrical loading [75]. Such an electrical loading is characterized by various harmonics, that depend on the space distribution of the coil sides within the slots. The amplitude of each harmonic is defined as

$$\hat{K}_\nu = \frac{3 k_{w\nu} N \hat{I}}{\pi D} \tag{6.2}$$

where $k_{w\nu}$ is the winding factor, N is the number of conductors per phase, D is the bore diameter, and $\hat{I}$ the amplitude of the current. These electrical loading harmonics cause MMF space–harmonics along the airgap, described as

$$U_s(\vartheta) = \int K(\vartheta)\frac{D}{2}d\vartheta \tag{6.3}$$

$$= \sum_{\nu} -\frac{\hat{K}_\nu}{\nu}\frac{D}{2p}\cos(\nu p\vartheta - \omega t) \tag{6.4}$$

To the sinusoidal distribution of each MMF harmonic corresponds a sinusoidal flux density distribution:

$$B_g(\vartheta) = \sum_{\nu} B_{g\nu}(\vartheta) \tag{6.5}$$

$$= \frac{\mu_0}{g}\sum_{\nu} U_{s\nu}(\vartheta) \tag{6.6}$$

where g is the magnetic air gap thickness including the Carter factor and the saturation factor. In IM, the air gap is constant and therefore the flux density distribution corresponds to the MMF distribution.

The torque is obtained by integrating the Lorentz's force density $B_g(\vartheta)K(\vartheta)$ along the air–gap surface, and multiplying the result by the radius $D/2$, i.e.,

$$\tau = -\frac{D}{2}\int_0^{2\pi} B_g(\vartheta)K(\vartheta)\frac{DL_{stk}}{2}d\vartheta \tag{6.7}$$

$$= -\frac{D^2 L_{stk}}{4}\sum_{\nu}\sum_{\xi}\int_0^{2\pi} B_{g\nu}(\vartheta)K_\xi(\vartheta)d\vartheta \tag{6.8}$$

Remembering that the Fourier series expansion is a series of orthogonal functions, the integral (6.7) is different from zero only if

- the harmonic distributions $B_{g\nu}(\vartheta)$ and $K_\xi(\vartheta)$ have the same order, i.e., when $\nu = \xi$;
- the distributions of the same order are not out of phase of 90 degrees.

From the second item, there is no torque contribution due to the current density distribution of the stator and flux density distribution produced by the stator itself. The same for the current and the flux density distributions produced by the rotor.

In conclusion, the torque is generated by the interaction of current density harmonics of the rotor and flux density harmonics of the same order due to the stator currents.

Let us also notice that only the main harmonics (i.e. of order $\nu = p$) have a synchronous speed, so that their contribution to the torque is constant. The amplitude of the interaction between the MMF harmonics of a given order of the winding can be quantified by the product of the winding factor of such order. The other harmonics have asynchronous speeds, hence, they cause an oscillating torque.

6.2.3 An index of harmonic interaction

As a consequence of the discussion above, it is convenient to have high amplitudes of the harmonics of order $\nu = p$. Conversely, it is imperative that the harmonics of different order exhibit a limited product of winding factor.

Therefore, on the basis of (6.8), it is possible to define a space–harmonic interaction index that has to be minimized as:

$$I_{shi} = \frac{\sum_{\nu=1,\ \nu\neq p}^{\infty} \frac{k_{ws\nu}\ k_{wr\nu}}{\nu}}{\frac{k_{wsp}\ k_{wrp}}{p}} \tag{6.9}$$

where $k_{ws\nu}$, $k_{wr\nu}$ are the stator and rotor winding factors for the generic harmonics of order ν and k_{wsp}, k_{wrp} are the stator and rotor winding factor for the main harmonics of order p.

For a given number of poles, it is possible to select the stator and rotor slot combination which minimizes this index, that is, with the lowest interaction between MMF harmonics.

6.2.4 Example: a 10–pole IM

As an example a 10 pole IM is considered having

- a stator with Q_s=12 slots, and
- a rotor with Q_r=15 slots.

The combination of slots and poles have been chosen so as to reduce the interaction between the harmonics of the two windings as described above.

The stator is characterized by a periodicity equal to t=1 (this is computed as the greater common divisor between the slots and the pole pairs, i.e. $t = G.C.D.\{Q_s, p\}$, [74]). The phasor representation of the EMF of the coil sides within the slots, also called star of slots [37], is formed by Q_s/t=12 spokes. Then, it is demonstrated in [8] that there are all MMF space harmonics of odd order, except those multiples of three.

Fig. 6.2(a) shows the stator of the doubly fed IM together with the coils of the phase a of the stator. The axis of the phase a is also highlighted. Fig. 6.2(b) shows the corresponding star of slots of the stator, according to the main harmonic, i.e. of order ν=p=5.

The rotor is characterized by a periodicity equal to $t = G.C.D.\{Q_r, p\}$=5. The star of slots is formed by Q_r/t=3 spokes. Then, there are all MMF harmonics of odd and even order multiple of $t = 5$, except those multiples of three.

Fig. 6.3(a) shows the rotor of the doubly fed IM together with the coils of the phase a of the rotor. The axis of the phase a has been chosen so as to be aligned to the axis of the phase a of the stator. Fig. 6.3(b) shows the corresponding star of slots, according to the main harmonic of order ν=p=5.

Fig. 6.4 shows the comparison between the winding factors of the stator and the rotor winding. Although there are many MMF space harmonics in the airgap, only a few numbers interact. In particular:

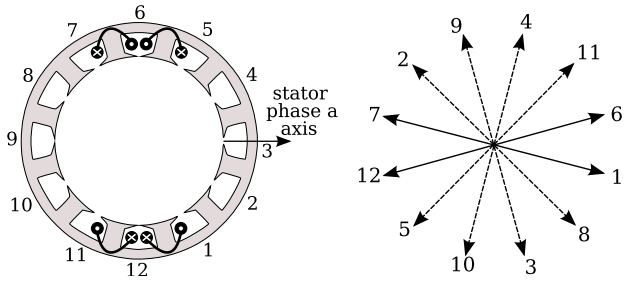

(a) Geometry (b) Star of slots

Figure 6.2: The 10–pole 12–slot stator and the stator of slots

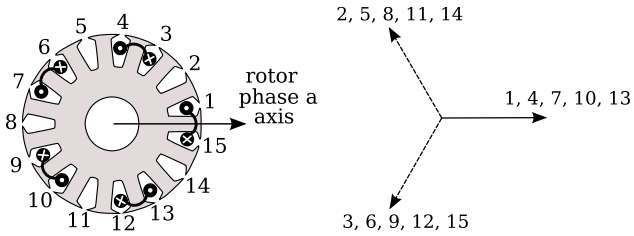

(a) Geometry (b) Star of slots

Figure 6.3: The 10–pole 15–slot rotor and the star of slots

- the main harmonic (ν=5): both winding exhibit a high winding factor;
- there are no interactions between harmonics of order lower than ν=5, that is, subharmonics;
- among the harmonics of higher order, the first harmonics that interact are the harmonics of order ν=25 and ν=35. Anyway, stator winding factor of these harmonics is low.

The order of the MMF space harmonics of the stator are found as $\nu = -(6k_1 + 1)$, where $k_1 = 0, \pm1, \pm2, ...$ [37]. The order of the MMF space harmonics of the rotor are found as $\nu = 5(3k_2 + 1)$, where $k_2 = 0, \pm1, \pm2, ...$ Thus the order of the harmonics that interact is found by the relationship $k_2 = -\frac{2}{5}(1 + k_1)$.

6.3 Analysis of the IM performance

The analysis of the IM is carried out at steady–state by means of the finite element method, adopting the field–oriented analysis strategy described in Chapter 4. This is briefly summarized hereafter.

At first both the stator and rotor winding are placed with the phase a axis along the x axis. When rotor field oriented control (FOC) is adopted, only d–axis flux linkage is present in the rotor. The flux linkage along the q–axis λ_{rq} is equal

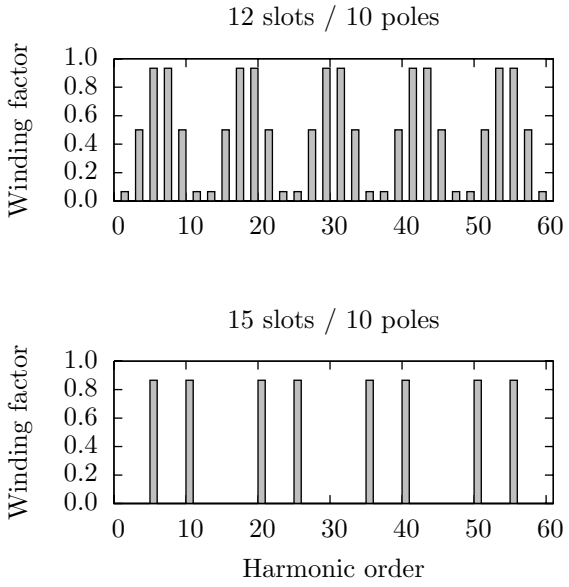

Figure 6.4: Comparison of winding factors of the two windings

to zero. For each stator current, it is possible to find the proper rotor current i_{rq} which realize the FOCcondition, that is $\lambda_{rq} = 0$ (see Chapter 4).

It is also possible to simulate the rotor movement. In this case the stator is fed at the frequency f. The mechanical angular speed of the magnetic field results in $\omega/p = 2\pi f/p$. The rotor rotates at the mechanical angular speed $\omega_m = (1-s)\omega/p$, and it is fed at the frequency $f_r = s\omega/(2\pi)$. Then, the reference frame, whose d–axis is along the rotor flux, rotates at the synchronous speed ω/p, as sketched in Fig. 6.5.

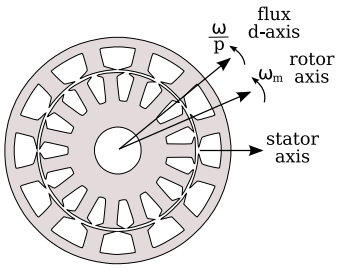

Figure 6.5: Reference axis and speeds during the simulations

6.4 Torque computation examples

Some finite element simulations are carried out adopting the IM presented in Sec. 6.2.4. A sketch of the lamination geometry is shown in Fig. 6.5; the external diameter is D_e=300 mm and the stack length is L_{stk}=100 mm. Fig. 6.6 shows the stator flux linkage versus the stator current and the rotor current. Each stator coil has 30 turns, while each rotor coil has 24 turns.

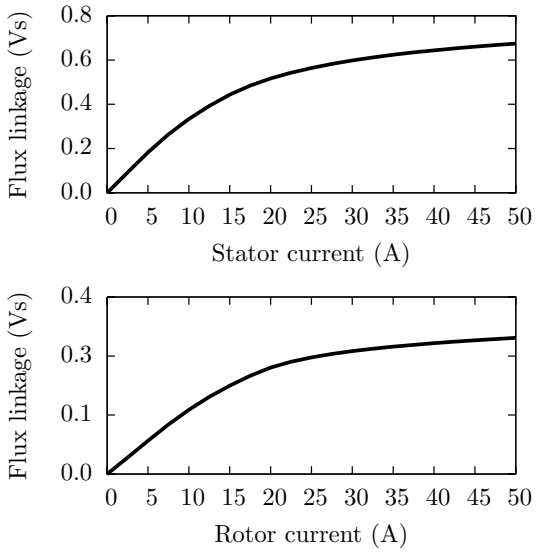

Figure 6.6: Stator flux linkage versus stator current (a) and rotor current (b)

Then the IM is fed with both stator and rotor currents, according to the technique presented above. Fig. 6.7 shows the torque computed for various rotor

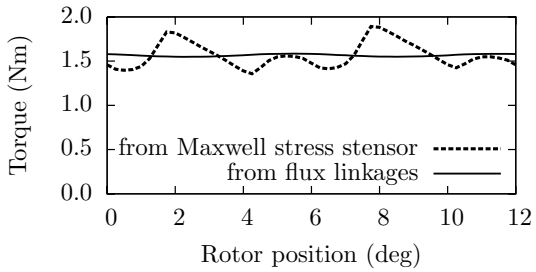

Figure 6.7: Torque versus rotor position at low current

positions. Low currents have been fixed so as to avoid iron saturation. The torque has been computed in two different ways:

1. computing Maxwell's stress tensor from the field solution,
2. computing as

$$\tau = \frac{3}{2} p(\lambda_{rq} i_{rd} - \lambda_{rd} i_{rq}) \tag{6.10}$$

Although both computations present the same average value, the first method considers the complete torque developed by the IM, while the second method inherently does not consider all torque oscillations [76].

Therefore, for an accurate analysis of the IM, the computation by means of Maxwell's stress tensor has to be carried out. For a rapid estimation of the average value of the torque, a single simulation can be carried out computing the torque by means of the d– and q–axis flux linkages [56].

Fig. 6.8 shows the torque computed for various rotor positions, for different current amplitudes. The stator and rotor currents are chosen with an angle displacement of 45 degree. In addition, the rotor current has been chosen with an amplitude equal to $1/\sqrt{2}$ of the stator current.

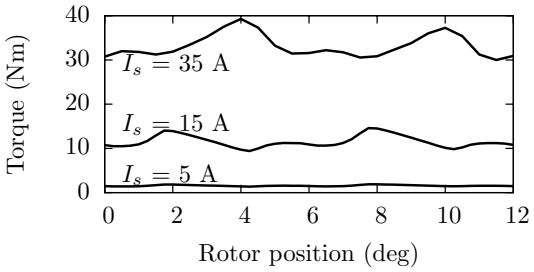

Figure 6.8: Torque versus rotor position for various stator currents

6.5 Example of a direct–drive doubly fed IM

In this section two doubly fed IMs for direct–drive applications are considered. They are designed according to the procedure described above.

The external diameter and the stack length are the same for both machines; they are D_e=3 m and L_{stk}=1 m respectively.

6.5.1 Low speed high torque application

The first example is an IM designed for a low speed application equal to 18 rpm. For a stator frequency f=50 Hz, the number of poles pair is p=167. The best solution for the minimization of the space–harmonics interaction index is Q_s=462 and Q_r=444. Using (6.9) it results in I_{shi}=0.35.

Such a number of poles is very high, and so the magnetizing current of the IM is comparable to the nominal current.

Fig. 6.9 shows a FE simulation of the machine with the flux lines. The stator slots are high and narrow causing a considerable leakage flux. This is also recognizable in Fig. 6.9 where only a few lines cross the airgap. This tooth geometry involves also mechanical design aspects of the lamination. The slot leakage flux also produces a saturation of the stator teeth. This is visible in Fig. 6.9 where the flux density map is reported using gray scale (the maximum flux density in the stator teeth is 2 T).

All these aspects limit the flux per pole of the IM so that its performance is very poor.

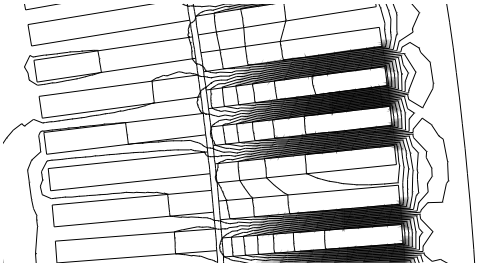

Figure 6.9: FE simulation of low speed direct–drive IM. Q_s=462, Q_r=444, p=167, I_{shi}=0.35

6.5.2 Medium torque medium speed application

In this subsection an IM designed for a speed in the range 70–80 rpm is considered. At first the best combination of poles and numbers of slots is identified so as to have the best index I_{shi}. The various combinations considered are reported in Table 6.1. The slot numbers used to identify the best combinations are chosen in the range from 30 to 120.

Table 6.1: Computation of the interaction index I_{shi} for various combinations of poles and slots number

2p	Q_s	Q_r	index
74	78	72	1.79
76	60	54	10.1
80	114	102	5.36
82	114	84	1.23
86	102	84	1.63

The selected solution is that with $2p$=82, Q_s=114 and Q_r=84. The IM is simulated with the strategy described in Sec. 6.3 so that the IM is simulated in FOCcondition. Fig. 6.10 shows the IM torque for various d–axis current (the total

slot current value is reported in the figures). For each d–axis current various q–axis current has been considered. Controlling the q–axis current allows one to adjust the torque of the machine.

In Fig. 6.11 the q–axis rotor current for each point of Fig. 6.10 is reported. With a positive q–axis stator current, the q–axis rotor current is negative as in (4.9). From Fig. 6.11 it can be noted that the four characteristics of q–axis rotor currents versus q–axis stator currents are very close. In other words, the rotor current variation is mainly related to the q–axis stator current variation, which is the torque component of the current. For different values of d–axis stator current, the rotor current is almost constant.

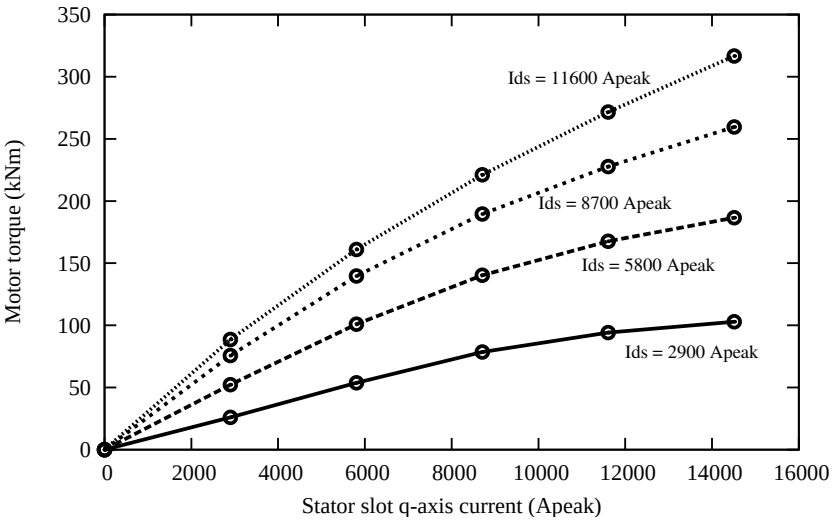

Figure 6.10: Torque of the IM for various d and q–axis stator currents. The current values refer to the total slot current.

Fig. 6.12 shows a rotation of the stator current vector. Various stator current densities have been considered. From these simulations it is possible to identify the maximum torque per Ampere (MTPA) trajectory. For a given stator current amplitude, the stator current angle is identified so as to achieve the maximum torque of the machine. In Fig. 6.12 the effect of the saturation on the MTPA trajectory is visible. At low current the MTPA trajectory is at 45 degree. As the current increases, the saturation rise in the machine and so the MTPA trajectory deviates towards higher angle.

Next the IM is simulated in steady state operation as described in Sec. 6.3. A working point of the IM is selected and it is kept while the stator and rotor fields rotate. In particular the total stator slot currents are I_{sd}=I_{sq}=11600 Apeak. The resulting rotor current is I_{rq}=-6821 Apeak. Fig. 6.13 shows the torque computed by means of the Maxwell stress tensor for various rotor positions. It is worth noticing that the torque ripple is very low, equal to 2.5%.

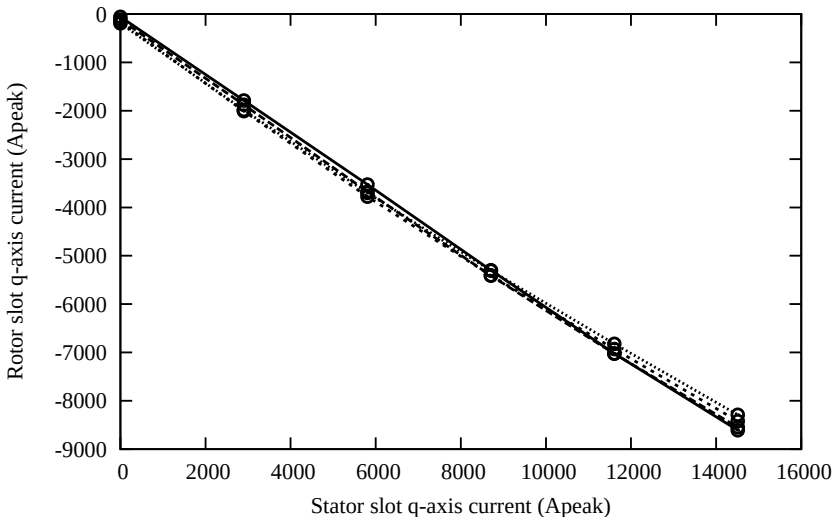

Figure 6.11: Rotor slot q–axis current versus q–axis stator current for the simulations of Fig. 6.10.

6.6 Conclusions

The possibility to adopt a fractional–slot doubly fed IM in a direct–drive application has been investigated in this Chapter. Various sizes of IMs have been considered and both advantages and drawbacks of the various solutions have been pointed out.

It has been shown that solutions with a high number of poles for high torque and low speed applications are not feasible. In fact this machines are characterized by a high magnetizing current. Moreover, the machine performance is limited also by the high leakage flux and by the teeth saturation. As the number of poles decreases, the effects of these drawbacks decreases too, and so the solution with a direct–drive fractional–slot winding become attractive.

With regards to the MMF harmonics the index I_{shi} has been introduced which quantify the interaction of the MMF harmonics with respect to the main harmonic of order p. It has been demonstrated that it is possible to find a slot–pole combination that minimizes the interaction among the MMF harmonics, reducing the torque ripple of the machine.

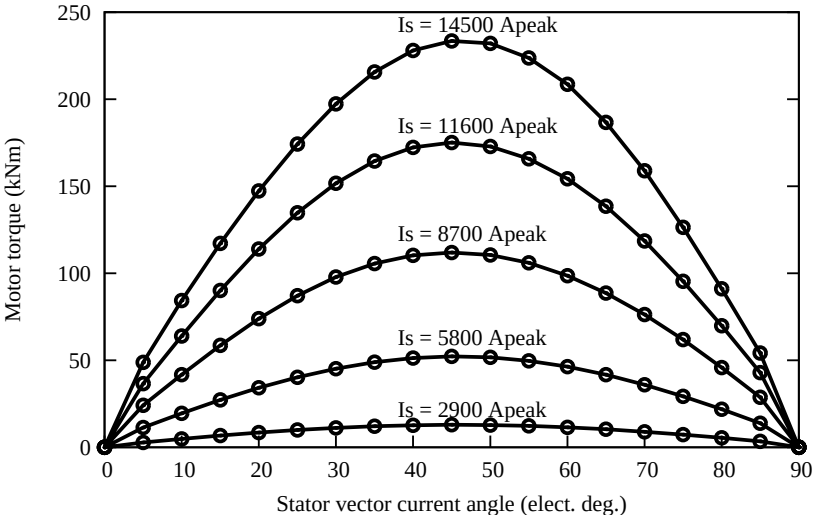

Figure 6.12: Rotation of the stator current vector for various stator current density

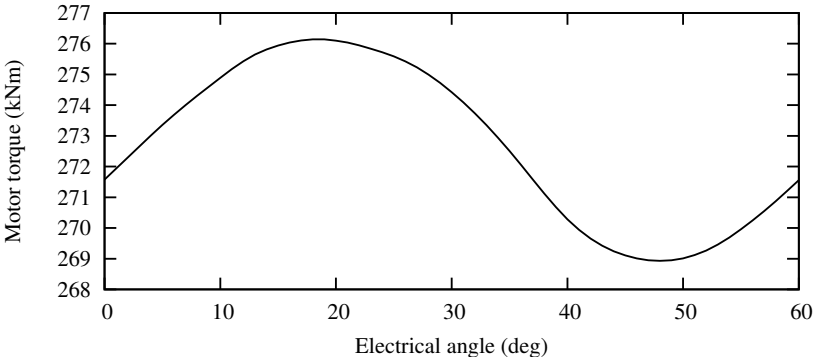

Figure 6.13: IM torque computed by means of Maxwell stress tensor for various rotor position

General Conclusions

This Thesis represents a contribution to the analysis of the induction machine (IM). Hereafter the main conclusions of the work are reported.

Rapid computation of IM performance

The normalized equivalent circuit presented in Chapter 1 allows a rapid and accurate prediction of the IM performance. FE analysis is used to estimate the two–dimensional parameters of the motor, while the three–dimensional effects are computed analytically. The results of each are then used to build an IM equivalent circuit from which the IM performance is predicted. It is shown that this procedure can be applied to the study of both three–phase and single–phase IMs.

A key issue of the proposed procedure is the choice of normalized parameters that makes the analysis independent of the actual motor length and number of turns per phase. The results are applicable to any motor employing the given lamination geometry and winding distribution. In this way the computed results can be easily extended to motors of different voltages and power ratings. The performance computed with the model proposed in Chapter 1 matches very good with the experimental tests carried out on several prototypes. Moreover, in Chapter 2 the potentiality of the model is exploited for the analysis of two series of IMs: the FE simulations are carried out only once for each lamination. Then, the performance computation of any IM depends only upon analytical calculations and as a result is very fast.

In Chapter 3, the normalized equivalent circuit is coupled with a lumped parameter thermal network. The thermally significant coefficients are computed using thermal FE simulations. In this way, the machine performance is computed more accurately, and is even suitable for use in analyzing motors for severe operating conditions. As an application of this combined model, a submerged pump is considered and presented. Measurements on a prototype shown that there is good agreement between the predicted values and measurements, also for the thermally dynamic cases.

IM simulation with field oriented technique

An alternative analysis approach is presented in Chapter 4. This strategy is suitable for the computation of steady state performance of IMs, particularly for variable speed ones. The IM simulation is similar to that of a synchronous machine so that the strategy is proper to achieve a rapid and precise prediction of the whole torque versus speed curve of the IM. Moreover, the MTPA trajectory of the IM drive is computed.

In Chapter 5 the above strategy is applied to compute the performance of an IM for a washing machine application. Various operating conditions, at low and high frequency, are presented. The reported experimental tests confirm the accuracy of the model. The discrepancy between tests and computations is small when the rotor currents can be assumed sinusoidally distributed along the rotor periphery. In other cases, the deviation between predictions and measurements increases, as pointed out in Chapter 5.

Doubly fed induction machines

The possibility of adopting a fractional–slot doubly fed IM in a direct–drive application is investigated in Chapter 6. Since the stator and rotor windings are given, and the currents are the source of the field, the real current distribution in the slots is actually determined. However a sinusoidal current distribution assumption does not exist as in the case of the squirrel cage IM.

It is shown that solutions with a high number of poles for high torque and low speed applications are not feasible due to the high magnetizing current, the high leakage flux and the teeth saturation. As the number of poles decreases, these drawbacks decrease, and the solution with a direct–drive fractional–slot winding becomes attractive.

With regards to the MMF harmonics, the index I_{shi} is introduced which quantifies the interaction of the MMF harmonics with respect to the main harmonic of order p. It is demonstrated that there exists a slot/pole combination that minimizes the interaction among the MMF harmonics thereby reducing the torque ripple of the machine.

Future prospects

Hereafter there are some suggestions for future research:

1. Improving the equivalent circuit model of the strategy proposed in Chapter 1. For example the iron loss model can be refined to consider better various loss contribution;

2. Implementation of the analysis described in Chapter 4 in a circuit solver for the IM drive simulation. In this way a precise simulation of the entire drive (machine and control) can be achieved;

3. In Chapter 6 the analysis strategy proposed in Chapter 4 has been extended for considering the rotor movement. This can be inspected in more detail while considering the effects of different simulations.

Appendix A

Practical Implementation

Abstract– In this Chapter the software developed during my PhD is briefly introduced. All the software is available at the download section of the website: http://edlab.die.unipd.it

A.1 Introduction

VARIOUS codes have been developed, which implement the methods described in this work. In the next sections, the codes are briefly introduced. The codes are freely available for further tests and collaborations over the Internet at the address http://edlab.die.unipd.it. They are distributed "as it is" under the terms of the GPL license:

```
/*************************************************************
* Copyright (C) 2009 by luigi alberti                        *
* luigi.alberti@unipd.it                                     *
*                                                            *
* This program is free software; you can redistribute it     *
* and/or modify it under the terms of the GNU General        *
* Public License as published by the Free Software           *
* Foundation; either version 2 of the License, or (at        *
* your option) any later version.                            *
*                                                            *
* This program is distributed in the hope that it will       *
* be useful, but WITHOUT ANY WARRANTY; without even the      *
* implied warranty of MERCHANTABILITY or FITNESS FOR A       *
* PARTICULAR PURPOSE.  See the GNU General Public            *
* License for more details.                                  *
*                                                            *
* You should have received a copy of the GNU General         *
* Public License along with this program; if not, write      *
* to the Free Software Foundation, Inc., 59 Temple Place     *
* - Suite 330, Boston, MA  02111-1307, USA.                  *
*************************************************************/
```

We believe that sharing the developed software tools with the rest of the "Electrical Machine Community" is also an original aspect of this work. For the FE simulations, the adopted software is *FEMM*, which is a powerful and free finite element simulator. It allow scripts functionality via a `LUA` console; the provided `LUA` script are briefly described in the next sections.

Other software has been developed in *C++*. In this case the library Qt4^{TM}has been used in order to make the software platform independent.

A.2 Rapid Analysis

In this section the software for the three-phase IM analysis presented in Chapter 1 is described. The same procedures have been used also in Chapter 2 and Chapter 3

A.2.1 FE analysis

The file used for the FE analysis are the following:

- `Example_0.fem`
  the femm file for the no–load simulations. The iron is non linear
- `Example_CC.fem`
  the femm file for the locked rotor simulations. The iron is linear
- `IM3_motordata.lua`
  a `lua` file with all the motor data and simulations parameters. It is invoked from the other `lua` script.
- `IM3_no_load.lua`
  the script that executes the no–load simulations of the IM. It has to be launched from `Example_0.fem`. The results are saved in the file `ris0.ris`.
- `IM3_lock_rotor.lua`
  the script that executes the locked rotor simulations of the IM. It has to be launched from `Example_CC.fem`. The results are saved in the file `risCC.ris`.
- `IM3_Post.lua`
  the script that executes the post computation on the field solution. It is invoked from other scripts.

A.2.2 IM performance prediction

Once the FE simulation is carried out with the code described above, the files `ris0.ris` and `risCC.ris` can be used to predict the performance of any IM formed by the lamination geometry described in `Example_CC.fem` and by the winding distribution described in `IM3_motordata.lua`.

For the computation of a particular IM performance, a file `motor.dat` with the actual motor data has to be edited. Then, the three files `motor.dat`, `ris0.ris` and `risCC.ris` are used by the *C++* code for the estimation of the IM performance. The results are written on the file `Performance.ris`. Two versions of the *C++* code are available: the first one is for console use and the second one uses a GUI. Both of them allow to customize the name of the file.

A.3 ϑ–less

In Chapter 3, a lumped parameters thermal network coupled to the IM equivalent circuit has been described. The thermal network parameters are computed on the basis of geometrical data and materials property. For the computation of the thermal exchange coefficients there are two main approaches. The first is to carry out a fluid–dynamic FE simulation. This typically involves a three dimensional solution and a considerable computational time. The second approach is to use semi empirical relation based on dimensionless relations. A comprehensive set of useful relations to compute the thermal parameters for the thermal network is given in [55]. Other useful reference are [54, 77–79]

ϑ–less is a small program written in *C++* to aid the designer during the thermal network parameters computation. It computes the dimensionless parameters. In Fig. A.1 a screenshot of the program is reported.

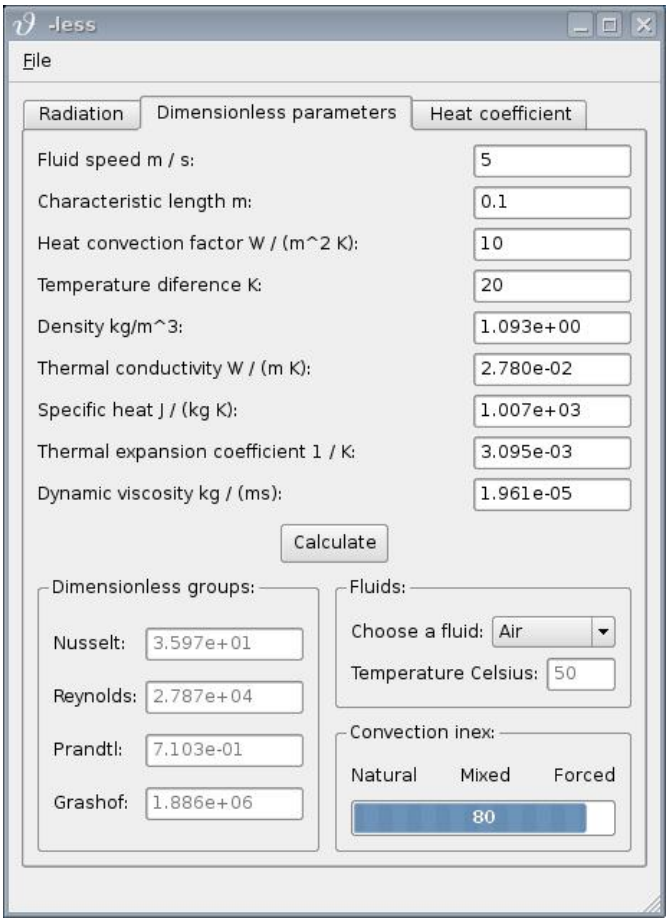

Figure A.1: A screenshot of ϑ–less.

A.4 Inkscape extension for star of slots

The star of slots has been introduced many times ago. Firstly, it was presented to the aim of designing large synchronous generators with a high number of poles. The star of slots is useful to determine the correct coils connection to maximize the main (synchronous) harmonic of the EMF induced in the windings.

Since the star of slots contains information of the winding distribution, it can be adopted not only for the analysis of the main harmonic of EMF, but also for the analysis of the harmonic contents of the EMF waveform, and of the airgap MMF distribution harmonic contents. An exhaustive and complete treatment is given in [8].

From a graphical point of view, the star of slots is a set of spokes which compose a star. The draw of the star of slots is done via an algorithmic way, and draw it by hand may become tedious.

In order to draw in an automatic way the star of slots starting from the winding data (number of slots, number of poles pair) I write this extension for Inkscape. Inkscape is a powerful, free, vector oriented drawing tool. The extension allow to draw the star of slot of any three–phase winding and for various harmonics order. The produced image can be saved in many graphical formats.

A.5 Koil

This program allows the design of a three–phase winding on the basis of the star of slots theory. The input data are the number of slots and the number of pole pairs. The user can then select a desired coil throw.

A draw of one phase winding is sketched, and a complete list of all coils of each phase is generated in a list–item view. Additionally, the winding factor of the harmonics up to order 100 is computed and reported in a table view.

A report with all the winding can be saved as file. Finally the slot matrices of the three phases can be exported in a file ready for use in *FEMM* `LUA` scripting.

As an example, Fig. A.2 shows a screenshot of the program. The winding 12–slot 10–pole (adopted in the example presented in Section 6.4) is considered. On the top left part there are the winding data. Below there is a list with all the coils of each phase. On the right there is a sketch of the winding (only one phase is reported).

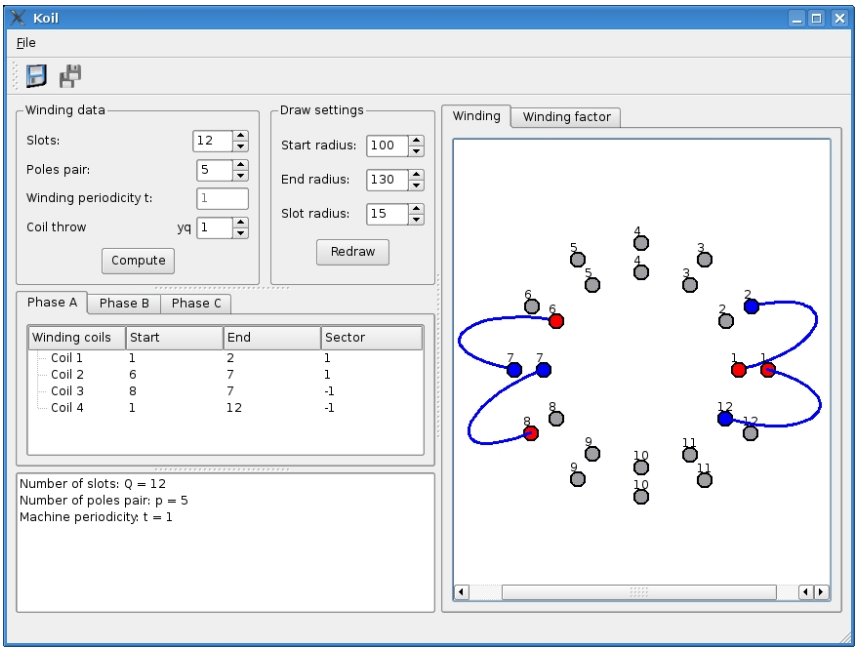

Figure A.2: A screenshot of Koil. A 12–slot 10–pole winding example is shown.

Bibliography

[1] L. Alberti, N. Bianchi, and S. Bolognani, "A rapid prediction of IM performance using a combined analytical and finite element analysis," in *IEEE International Electric Machines & Drives Conference. (IEMDC '07)*, vol. 1, Antalya, Turkey, May 3–5 2007, pp. 334–340.

[2] ——, "Lamination Design of a Set of Induction Motors for Elevator Systems," in *IEEE International Electric Machines & Drives Conference. (IEMDC '07)*, vol. 1, Antalya, Turkey, May 3–5 2007, pp. 514–518.

[3] ——, "A Very Rapid Prediction of IM Performance Combining Analytical and Finite-element Analysis," *IEEE Transactions on Industry Applications*, vol. 44, no. 5, pp. 1505–1512, Sep./Oct. 2008.

[4] L. Alberti and N. Bianchi, "A Coupled Thermal-Electromagnetic Analysis for a Rapid and Accurate Prediction of IM Performance," *IEEE Transactions on Industrial Electronics*, vol. 55, no. 10, pp. 3575–3582, Oct. 2008.

[5] L. Alberti, N. Bianchi, P. Baldassari, and R. Wang, "Thermal Assisted Finite Element Analysis of Electrical Machines," in *International Conference on Electrical Machines (ICEM)*, Vilamoura, Portugal, Sep. 6–9 2008, pp. 1–4 CD–ROM.

[6] L. Alberti, N. Bianchi, and S. Bolognani, "Field Oriented Control of Induction Motor: a Direct Analysis Using Finite Element," in *34th IEEE IES Annual Meeting (IECON)*, Orlando, FL, USA, Nov. 10–13 2008, pp. 1–4 CD–ROM.

[7] ——, "Finite Element Modeling of Induction Motor for Variable Speed Drives," in *International Conference on Electrical Machines (ICEM)*, Vilamoura, Portugal, Sep. 6–9 2008, pp. 1–6 CD–ROM.

[8] N. Bianchi, M. Dai Pré, L. Alberti, and E. Fornasiero, *Theory and Design of Fractional-Slot PM Machines*, Sponsored by the IEEE-IAS Electrical Machines Commitee, Ed. Padova: CLEUP (ISBN 978-88-6129-122-5), 2007.

[9] C. Veinott, *Theory and Design of Small Induction Motors.* New York: McGraw–Hill Book Company, 1959.

[10] P. Alger, *Induction machines, their behavior and uses*, second edition ed. New York, London, Paris: Gordon and Breach Science Publishers, 1970.

[11] M. Liwschitz-Garik and C. C. Whipple, *Electric Machinery, vol.II, A–C Machines*. New York: D. Van Nostrand Company Inc., 1960.

[12] S. Williamson and J. Ralph, "Finite–element analysis of an induction motor fed from a constant–voltage source," *IEE Proc., Pt. B*, vol. 130, no. 1, pp. 18–24, Jan. 1983.

[13] S. Williamson, A. Smith, M. Begg, and J. Smith, "General techniques for the analysis of induction machines using finite elements," in *Proc. of International Conference on Evolution and Modern Aspect of Induction Motors*, Turin, Italy, July 8–11 1986, pp. 389–395.

[14] A. Arkkio, "Analysis of induction motors based on the numerical solution of the magnetic field and circuit equations," Ph.D. Thesis, Helsinki University of Technology, Helsinki, Finland, Laboratory of Electromechanics, 1987, acta Polytechnica Scandinava, Electr. Eng. Series No.59.

[15] N. Bianchi, S. Bolognani, and G. Comelato, "Finite element analysis of three-phase induction motors: Comparison of two different approaches," *IEEE Transactions on Energy Conversion*, vol. 14, no. 4, pp. 1523–1528, Dec 1999.

[16] S. Williamson and A. Smith, "Field analysis for rotating induction machines and its relationship to the equivalent circuit," *IEE Proc., Pt. B, Elect. Power Applications*, vol. 127, no. 2, pp. 83–90, March 1980.

[17] N. Bianchi, *Electrical Machine Analysis using Finite Elements*, ser. Power Electronics and Applications Series, CRC, Ed. Boca Raton, FL, USA: CRC Press, Taylor & Francis Group, 2005.

[18] S. Williamson and M. J. Robinson, "Calculation of cage induction motor equivalent circuit parameters using finite elements," in *Electric Power Applications, IEE Proceedings B [see also IEE Proceedings-Electric Power Applications]*, vol. 138, Sep. 1991, pp. 264–276.

[19] D. M. Ionel, M. Popescu, S. J. Dellinger, T. J. E. Miller, R. J. Heideman, and M. I. McGilp, "On the variation with flux and frequency of the core loss coefficients in electrical machines," *IEEE Transactions on Industry Applications*, vol. 42, no. 3, pp. 658–667, May/Jun. 2006.

[20] M. A. Mueller, S. Williamson, T. J. Flack, K. Atallah, B. Baholo, D. Howe, and P. H. Mellor, "Calculation of iron losses from time–stepped finite–element models of cage induction machines," in *Electrical Machines and Drives, 1995. Seventh International Conference on (Conf. Publ. No. 412)*, Sep. 11–13, 1995.

[21] W. Schuisky, *Berechnung Elektrischer Maschinen*. Springer Verlag, Wien, 1967.

[22] G. Müller, K. Vogt, and B. Ponick, *Berechnung elektrischer Maschinen*, 6th ed. Weinheim: Willey–Vch, 2008.

[23] S. Swann and J. Salmon, "Effective resistance and reactance of a solid cylindrical conductor embedded in a semi–closed slot," *IEE Proceedings*, vol. 109, no. c, pp. 1–33, 1962.

[24] T. Birch and O. Butler, "Permeance of closed–slot bridges and its effect on induction motor current computation," *IEE Proceedings*, vol. 118, no. 1, pp. 169–172, Jan. 1971.

[25] S. Williamson and M. Begg, "Calculation of the bar resistance and leakage reactance of cage rotors with closed slots," *IEE Proc., Pt. B, Elect. Power Applications*, vol. 132, no. 3, pp. 125–132, May 1985.

[26] B. Heller and V. Hamata, *Harmonic field effects in induction machines.* Amsterdam ; Elsevier Scientific Pub. Co., 1977.

[27] C. Steinmetz, "The alternating current induction motor," *Transaction AIEE*, vol. 14, pp. 185–217, 1897.

[28] G. Kron, *Equivalent circuits of electric machinery*, first edition ed. New York: John Wiley, 1951.

[29] I. Boldea and S. A. Nasar, *The Induction Machine Handbook*, ser. Power Electronics and Applications Series. Boca Raton, FL, USA: CRC Press, Taylor & Francis Group, 2001.

[30] G. R. Slemon and A. Straughen, *Electric Machines.* Addison–Wesley Pub. Co., New York, 1980.

[31] S. Tandom, E. Richter, and M.V.K.Chari, "Finite elements and electrical machine design," *IEEE Transactions on Magnetics*, vol. 16, pp. 1020–1022, 1980.

[32] R. Richter, *Lehrbuch der Wicklungen Elektrischer Machinen*, W. Bucherei, Ed. Karlsruhe: G. Braun, 1952.

[33] M. V. K. Chari and P. P. Silvester, *Finite Elements in Electrical and Magnetic Field Problems*, ser. Numerical Methods in Engineering, Wiley, Ed. New York: John Wiley & Sons, 1980.

[34] P. Trickey, "Induction motor resistance ring width," *Trans. AIEE*, vol. 55, pp. 144–150, 1936.

[35] M. V. K. Chari, D. Sharma, and H. Kudlacik, "No load magnetic field analysis in the end region of a turbine generator by the method of finite elements," in *Proc. of IEEE Power Engineering Society winter meeting*, New York, Jan. 1976.

[36] S. Williamson and M. C. Begg, "Calculation of the resistance of induction motor end rings," *Electric Power Applications, IEE Proceedings B*, vol. 133, pp. 54–60, Mar. 1986.

[37] M. Liwschitz-Garik and C. C. Whipple, *Alternating–Current Machines.* Van Nostrand Company, 1961, iD: Macchine elettriche; ID: Corrente alternata.

[38] R. Richter, "Die induktionmaschinen," in *Elektrische Maschinen.* Verlag Birkhäuser, 1954, vol. 4.

[39] A. Puchstein and T. Lloyd, "The cross-field theory of the capacitor motor," *Trans. AIEE*, vol. 60, pp. 58–63, February 1941.

[40] F. Suhr, "Symmetrical components as applied to the single–phase induction motor," *Trans. AIEE*, vol. 64, pp. 651–655, Sept. 1945.

[41] P. Trickey, "Capacitor motor performance calculations by the cross–field theory," *Trans. AIEE*, vol. 76, pp. 1547–1553, February 1957.

[42] W. Morrill, "The revolving–field theory of the capacitor motor," *Trans AIEE*, vol. -, pp. 614–632, April 1929.

[43] I. Boldea, T. Dumitrescu, and S. A. Nasar, "Unified analysis of 1-phase AC motors having capacitors in auxiliary windings," *IEEE Transaction on Energy Conversion*, vol. 14, no. 3, pp. 577–582, Sep. 1999.

[44] C. Rasmussen and T. Miller, "Revolving–field polygon technique for performance prediction of single–phase induction motors," *IEEE Transactions on Industry Applications*, vol. 39, no. 5, pp. 1300–1306, Sept.–Oct. 2003.

[45] H. Fudeh and C. Ong, "Modeling and analysis of induction machines containing space harmonics," *AIEE Trans. on Power Apparatus System*, vol. 102, pp. 2608–2628, August 1983.

[46] L. Buchanan, "An equivalent circuit for a single–phase motor having space harmonics in its magnetic field," *AIEE Trans. on Power Apparatus System*, vol. 84, pp. 999–1007, November 1965.

[47] J. Davis and D. Novotny, "Equivalent circuits for single–phase squirrel–cage induction machines with both odd and even order mmf harmonics," *AIEE Trans. on Power Apparatus System*, vol. 88, pp. 1080–1086, July 1969.

[48] P. Lorrain, D. Corson, and F. Lorrain, *Electromagnetic fields and waves.* New York: W. H. Freeman and co., 1988.

[49] M. J. Duran, J. L. Duran, F. Perez, and J. Fernandez, "Induction-motor sensorless vector control with online parameter estimation and overcurrent protection," *IEEE Transactions on Industrial Electronics*, vol. 53, no. 1, pp. 154–161, Dec. 2005.

[50] A. B. Proca and A. Keyhani, "Sliding-mode Flux Observer With Online Rotor Parameter Estimation for Induction Motors," *IEEE Transactions on Industrial Electronics*, vol. 54, no. 2, pp. 716–723, Apr. 2007.

[51] C. G. Stone, A. E. Boulter, I. Culbert, and H. Dhirani, *Electrical insulation for rotating machines*, ser. IEEE press series on power engineering. John Wiley & sons, 2004.

[52] F. Reffo, "Lumped Parameter Thermal Model for Electrical Machines. Application to Submerged Motors," Master's thesis, University of Padova, 2007.

[53] P. H. Mellor, D. Roberts, and D. R. Turner, "Lumped parameter thermal model for electrical machines of TEFC design," in *Electric Power Applications, IEE Proceedings B [see also IEE Proceedings-Electric Power Applications]*, vol. 138, Sep. 1991, pp. 205–218.

[54] D. Staton, A. Boglietti, and A. Cavagnino, "Solving the More Difficult Aspects of Electric Motor Thermal Analysis in Small and Medium Size Industrial Induction Motors," *IEEE Transactions on Energy Conversion*, vol. 20, no. 3, pp. 620–628, Sep. 2005.

[55] D. A. Staton and A. Cavagnino, "Convection Heat Transfer and Flow Calculations Suitable for Electric Machines Thermal Models," *IEEE Transactions on Industrial Electronics*, vol. 55, no. 10, pp. 3509–3516, Oct. 2008.

[56] N. Bianchi, L. Alberti, M. Popescu, and T. J. E. Miller, "MMF Harmonics Effect on the Embedded FE-analytical Computation of PM Motors," in *42nd IEEE IAS Annual Meeting*, New Orleans, LA, USA, Sep. 23–27 2007, pp. 1544–1551.

[57] N. Bianchi and S. Bolognani, "Design procedure of a vector controlled induction motor for flux-weakening operations," in *Industry Applications Conference, 1997. Thirty-Second IAS Annual Meeting, IAS '97., Conference Record of the 1997 IEEE*, vol. 1, New Orleans, LA, Oct. 5–9, 1997, pp. 104–111.

[58] G. R. Slemon, "Modelling of induction machines for electric drives," *IEEE Transactions on Industry Applications*, vol. 25, no. 6, pp. 1126–1131, Nov./Dec. 1989.

[59] S. Williamson and M. S. Boger, "Impact of inter-bar currents on the performance of the brushless doubly-fed motor," in *Industry Applications Conference, 1997. Thirty-Second IAS Annual Meeting, IAS '97., Conference Record of the 1997 IEEE*, vol. 1, New Orleans, LA, Oct. 1997, pp. 188–195.

[60] C. I. McClay and S. Williamson, "Influence of rotor skew on cage motor losses," in *Electric Power Applications, IEE Proceedings-*, vol. 145, Sep. 1998, pp. 414–422.

[61] ——, "The variation of cage motor losses with skew," in *Industry Applications Conference, 1998. Thirty-Third IAS Annual Meeting. The 1998 IEEE*, vol. 1, St. Louis, MO, Oct. 1998, pp. 79–86.

[62] D. M. Ionel, M. Popescu, M. I. McGilp, T. J. E. Miller, S. J. Dellinger, and R. J. Heideman, "Computation of Core Losses in Electrical Machines Using Improved Models for Laminated Steel," *IEEE Transactions on Industry Applications*, vol. 43, no. 6, pp. 1554–1564, Nov./Dec. 2007.

[63] S. Williamson and C. I. McClay, "Optimization of the geometry of closed rotor slots for cage induction motors," *IEEE Transactions on Industry Applications*, vol. 32, no. 3, pp. 560–568, May/Jun. 1996.

[64] S. Williamson and Y. N. Feng, "Slot-harmonic Fields in Closed-slot Machines," in *Electric Machines & Drives Conference, 2007. IEMDC '07. IEEE International*, vol. 1, Antalya, Turkey, May 2007, pp. 482–488.

[65] *http://www.magneforcess.com*.

[66] H. Polinder, D. Bang, R. P. J. O. M. van Rooij, A. S. McDonald, and M. A. Mueller, "10 MW Wind Turbine Direct-drive Generator Design with Pitch or Active Speed Stall Control," in *Electric Machines & Drives Conference, 2007. IEMDC '07. IEEE International*, vol. 2, Antalya, May 3–5, 2007, pp. 1390–1395.

[67] A. Binder and T. Schneider, "Permanent magnet synchronous generators for regenerative energy conversion - a survey," in *Power Electronics and Applications, 2005 European Conference on*, Sep. 11–14, 2005.

[68] R. Pea, R. Cerdenas, J. Proboste, G. Asher, and J. Clare, "Sensorless Control of Doubly-fed Induction Generators Using a Rotor-current-based MRAS Observer," *IEEE Transactions on Industrial Electronics*, vol. 55, no. 1, pp. 330–339, Jan. 2008.

[69] R. Pena, J. C. Clare, and G. M. Asher, "Doubly fed induction generator using back-to-back PWM converters and its application to variable-speed wind-energy generation," in *Electric Power Applications, IEE Proceedings* -, vol. 143, May 1996, pp. 231–241.

[70] ——, "A doubly fed induction generator using back-to-back PWM converters supplying an isolated load from a variable speed wind turbine," in *Electric Power Applications, IEE Proceedings* -, vol. 143, Sep. 1996, pp. 380–387.

[71] R. Pena, R. Cardenas, J. Proboste, J. Clare, and G. Asher, "Wind-Diesel Generation Using Doubly Fed Induction Machines," *IEEE Transaction on Energy Conversion*, vol. 23, no. 1, pp. 202–214, Mar. 2008.

[72] F. Bonnet, P. E. Vidal, and M. Pietrzak-David, "Dual Direct Torque Control of Doubly Fed Induction Machine," *IEEE Transactions on Industrial Electronics*, vol. 54, no. 5, pp. 2482–2490, Oct. 2007.

[73] G. Iwanski and W. Koczara, "Sensorless Direct Voltage Control of the Stand-alone Slip-ring Induction Generator," *IEEE Transactions on Industrial Electronics*, vol. 54, no. 2, pp. 1237–1239, Apr. 2007.

[74] N. Bianchi and M. Dai Pré, "Use of the star of slots in designing fractional-slot single-layer synchronous motors," in *Electric Power Applications, IEE Proceedings* -, vol. 153, May 1, 2006, pp. 459–466.

[75] E. Levi, *Polyphase motors: a direct approach to their design*, Wiley & Sons, Ed. New York, N.Y., 1984.

[76] D. White and H. Woodson, *Electromechanical Energy Conversion.* John Wiley & Sons, 1959.

[77] A. Boglietti, A. Cavagnino, and D. Staton, "Determination of Critical Parameters in Electrical Machine Thermal Models," *IEEE Transactions on Industry Applications*, vol. 44, no. 4, pp. 1150–1159, Jul./Aug. 2008.

[78] A. Boglietti and A. Cavagnino, "Analysis of the Endwinding Cooling Effects in TEFC Induction Motors," *IEEE Transactions on Industry Applications*, vol. 43, no. 5, pp. 1214–1222, Sep./Oct. 2007.

[79] A. Boglietti, A. Cavagnino, M. Parvis, and A. Vallan, "Evaluation of radiation thermal resistances in industrial motors," *IEEE Transactions on Industry Applications*, vol. 42, no. 3, pp. 688–693, May/Jun. 2006.

The paper published during my PhD period

(1) L. Alberti, "Formulazione debole di problemi di elettromagnetismo. applicazione mediante il codice agli elementi finiti GetDP," Master's thesis, University of Padova, 2005, Supervisor: prof. Nicola Bianchi.

(2) L. Alberti, N. Bianchi, and S. Bolognani, "Lamination Design of a Set of Induction Motors for Elevator Systems," in *IEEE International Electric Machines & Drives Conference. (IEMDC '07)*, vol. 1, Antalya, Turkey, May 3–5 2007, pp. 514–518.

(3) ——, "A rapid prediction of IM performance using a combined analytical and finite element analysis," in *IEEE International Electric Machines & Drives Conference. (IEMDC '07)*, vol. 1, Antalya, Turkey, May 3–5 2007, pp. 334–340.

(4) N. Bianchi, L. Alberti, M. Popescu, and T. J. E. Miller, "MMF Harmonics Effect on the Embedded FE-analytical Computation of PM Motors," in *42nd IEEE IAS Annual Meeting*, New Orleans, LA, USA, Sep. 23–27 2007, pp. 1544–1551.

(5) T. S. Kwon, S. K. Sul, L. Alberti, and N. Bianchi, "Design and Control of an Axial Flux Machine for a Wide Flux-weakening Operation Region," in *42nd IEEE IAS Annual Meeting*, New Orleans, LA, USA, Sep. 23–27 2007, pp. 2175–2182.

(6) N. Bianchi, M. Dai Pré, L. Alberti, and E. Fornasiero, *Theory and Design of Fractional-Slot PM Machines*, Sponsored by the IEEE-IAS Electrical Machines Commitee, Ed. Padova: CLEUP (ISBN 978-88-6129-122-5), 2007.

(7) L. Alberti, N. Bianchi, and S. Bolognani, "Efficiency Reduction due to the Rotor Losses in Fractional–Slot PM Machines," in *EVER Conference*, Monaco, Montecarlo, Mar. 27–30 2008, pp. 1–6 CD–ROM.

(8) A. Faggion, L. Sgarbossa, L. Alberti, M. Barcaro, M. Dai Pre, and S. Bolognani, "Effective control of an Integrated Starter-alternator with an IPM synchronous machine," in *39nd IEEE PES Annual Meeting (PESC)*, Rhodes, Greece, Jun. 15–19 2008, pp. 3924–3929.

(9) L. Alberti, "Energy supplying of high altitude isolated users," in *43rd International Uniersities Power Engineering Conference (UPEC)*, Padova, Italy, Sep. 1–4 2008, pp. 1–5 CD–ROM.

(10) L. Alberti, N. Bianchi, P. Baldassari, and R. Wang, "Thermal Assisted Finite Element Analysis of Electrical Machines," in *International Conference on Electrical Machines (ICEM)*, Vilamoura, Portugal, Sep. 6–9 2008, pp. 1–4 CD–ROM.

(11) L. Alberti, N. Bianchi, and S. Bolognani, "Finite Element Modeling of Induction Motor for Variable Speed Drives," in *International Conference on Electrical Machines (ICEM)*, Vilamoura, Portugal, Sep. 6–9 2008, pp. 1–6 CD–ROM.

(12) M. Barcaro, L. Alberti, A. Faggion, L. Sgarbossa, M. Dai Pré, and N. Bianchi, "Experimental Tests on a 12–slot 8–ploe Integrated Starter–Alternator," in *International Conference on Electrical Machines (ICEM)*, Vilamoura, Portugal, Sep. 6–9 2008, pp. 1–6 CD–ROM.

(13) L. Alberti, N. Bianchi, and S. Bolognani, "A Very Rapid Prediction of IM Performance Combining Analytical and Finite-element Analysis," *IEEE Transactions on Industry Applications*, vol. 44, no. 5, pp. 1505–1512, Sep./Oct. 2008.

(14) L. Alberti and N. Bianchi, "A Coupled Thermal-Electromagnetic Analysis for a Rapid and Accurate Prediction of IM Performance," *IEEE Transactions on Industrial Electronics*, vol. 55, no. 10, pp. 3575–3582, Oct. 2008.

(15) ——, "Electric drive for an in–wheel fractional–slot axial flux machine," *Power Electronics ISSN 1000-100X*, vol. 42, no. 10, pp. 7–10, Oct. 2008.

(16) L. Alberti, E. Fornasiero, N. Bianchi, and S. Bolognani, "Impact of Rotor Losses in a 12–slot 10–pole Axial Flux PM Machine," in *43nd IEEE IAS Annual Meeting*, Edmont, Canada, Oct. 5–9 2008, pp. 1–8 CD–ROM.

(17) M. Barcaro, L. Alberti, M. Dai Pré, A. Faggion, L. Sgarbossa, N. Bianchi, and S. Bolognani, "IPM Machine Drive Design and Test for an Integrated Starter Alternator Application," in *43nd IEEE IAS Annual Meeting*, Edmont, Canada, Oct. 5–9 2008, pp. 1–8 CD–ROM.

(18) L. Alberti, N. Bianchi, and S. Bolognani, "Field Oriented Control of Induction Motor: a Direct Analysis Using Finite Element," in *34th IEEE IES Annual Meeting (IECON)*, Orlando, FL, USA, Nov. 10–13 2008, pp. 1–4 CD–ROM.

(19) L. Alberti, M. Barcaro, N. Bianchi, S. Bolognani, D. Bon, M. Castiello, A. Faggion, E. Fornasiero, and L. Sgarbossa, "Interior Permanent Magnet Integrated Starter–Alternator," in *EVER Conference*, Monaco, Montecarlo, Mar. 26–29 2009, pp. 1–8 CD–ROM.